UNIVERSITY OF CALIFORNIA SAN DIEGO

Numerical simulations of vortex breakdown in swirling jets and diffusion flames

A dissertation submitted in partial satisfaction of the
requirements for the degree Doctor of Philosophy

in

Engineering Sciences (Mechanical Engineering)

by

Benjamin W. Keeton

Committee in charge:

Professor Keiko K. Nomura, Chair
Professor Antonio L. Sánchez
Professor Oliver T. Schmidt
Professor Forman A. Williams
Professor William R. Young

2023

The Dissertation of Benjamin W. Keeton is approved, and it is acceptable in quality and form for publication on microfilm and electronically.

University of California San Diego

2023

TABLE OF CONTENTS

LIST OF FIGURES

LIST OF TABLES

ACKNOWLEDGEMENTS

I would like to thank Professor Keiko K. Nomura for serving as my advisor for the last four years, and chairing my doctoral committee. Our discussions always led to valuable insight that was instrumental to the success of the work presented in this dissertation. Furthermore, I would like to acknowledge the support of Professor Antonio L. Sánchez and Professor Forman A. Williams. Meetings with all three faculty members were enjoyable and inspired me to conduct this research. I would also like to thank Oliver T. Schmidt and William R. Young for agreeing to serve on my committee, and providing excellent instruction on fundamental fluid dynamics and mathematics coursework.

In chapter 3, the axisymmetric results are published in the Journal of Fluid Mechanics 2022. Keeton, Benjamin W.; Carpio, Jaime; Nomura, Keiko K.; Sánchez, Antonio L.; Williams, Forman A. The author of this dissertation contributed the unsteady numerical simulations and is indebted to his co-authors for the first-authorship.

The work discussed in chapter 4 is published in the Proceedings of the Combustion Institute 2022. Keeton, Benjamin W.; Nomura, Keiko K.; Sánchez, Antonio L.; Williams, Forman A. The dissertation author was the primary investigator in this project.

The axisymmetric results of chapter 5 have been submitted to Combustion & Flame 2023. Keeton, Benjamin W.; Nomura, Keiko K.; Sánchez, Antonio L.; Williams, Forman A. The dissertation author was the primary investigator in this project.

The majority of the numerical simulations in this work used Bridges-2 at Pittsburgh Supercomputer Center and Stampede2 at Texas Advanced Computing Center through allocations PHY210060 and MCH220017 from the Advanced Cyberinfrastructure Coordination Ecosystem: Services & Support (ACCESS) program, which is supported by National Science Foundation grants #2138259, #2138286, #2138307, #2137603, and #2138296.

VITA

2015	Bachelor of Science, University of Rochester
2021	Master of Science, University of California San Diego
2023	Doctor of Philosophy, University of California San Diego

PUBLICATIONS

Keeton, B.W., Carpio, J., Nomura, K.K., Sánchez, A.L., & Williams, F.A. (2022). Vortex breakdown in variable-density gaseous swirling jets. *J. Fluid Mech.*, 936, A1.

Keeton, B.W., Nomura, K.K., Sánchez, A.L., & Williams, F.A. (2022). Vortex breakdown in swirling Burke-Schumann flames. *Proc. Combust. Inst.*.

Keeton, B.W., Nomura, K.K., Sánchez, A.L., & Williams, F.A. (2023). A computational investigation of swirl-number and Damköhler-number effects on vortex breakdown in non-premixed laminar swirling jet flames. *Combust. Flame*. Submitted.

FIELDS OF STUDY

Major Field: Mechanical & Aerospace Engineering

Studies in Fluid Dynamics
Studies in Combustion

ABSTRACT OF THE DISSERTATION

Numerical simulations of vortex breakdown in swirling jets and diffusion flames

by

Benjamin W. Keeton

Doctor of Philosophy in Engineering Sciences (Mechanical Engineering)

University of California San Diego, 2023

Professor Keiko K. Nomura, Chair

In combustion applications such as gas turbines, swirling jets are used to generate a vortex breakdown recirculation region that serves as a non-invasive flame stabilizer. The present work performs direct numerical simulations to study the effects of vortex breakdown on the structure and stabilization of laminar low-Mach-number gaseous diffusion flames.

Vortex breakdown transitions are first studied for heated/cooled variable-density, non-reacting jets in solid body rotation issuing into an unconfined ambient atmosphere. For increasing values of the swirl number S, two vortex breakdown modes are observed, the bubble and the cone, and the associated transitions S_B^* and S_C^* are determined for different values of the ambient-to-jet temperature ratio Λ. Both axisymmetric and three-dimensional

simulations show decreasing values of S_B^* with increasing Λ, while critical swirl numbers for the transition to the cone S_C^*, remain relatively constant for a fixed effective Reynolds number.

The first study is then extended to evaluate the same transitions in axisymmetric methane-air flames in the Burke-Schumann limit of infinitely fast chemistry. Transitions S_B^* are relatively unaffected by fuel-feed dilution, and result in jet-like flames. For moderate values of dilution, further increase in S to S_C^* generates a steady conical breakdown, with the flame sheet again passing around the recirculating fuel and products. Extreme dilution, on the other hand, generates an enlarged cone that recirculates the ambient air, stabilizing the flame near the jet inlet.

Effects of bubble vortex breakdown are then explored for finite-rate chemistry flames in an axisymmetric concentric swirling jet configuration, for which a central fuel jet is surrounded by a swirling co-annular stream of air. Liftoff and blow-off are analyzed by systematically varying the two relevant parameters, the swirl number S and the Damköhler number, D_N. For sufficiently low values of D_N, and large values of S, flames lift off the injector, and thermal expansion at the base of the triple flame redirects the flow radially inward, promoting the formation of a small recirculation zone. Axisymmetric and three-dimensional simulations of the isothermal flow are used to analyze the mechanism for the onset of the bubble, and identify post-breakdown flow structure for larger values of the Reynolds number.

Chapter 1

Introduction

1.1 Motivation

In non-premixed combustion chambers, swirling jets are utilized to enhance fuel/air mixing and improve combustion efficiency (Syred and Beer, 1974). For sufficiently large values of the swirl number S, a measure of the ratio of azimuthal to axial inlet velocity components, vortex breakdown, characterized by the formation of an internal stagnation point and a reversed axial flow (Leibovich, 1978), is known to occur. The onset of vortex breakdown in a reacting flow produces a transition in the flame structure, and the reversed axial flow serves as a non-invasive flame-stabilizer. Of particular interest are stationary low-Mach-number combustion applications like gas turbine flames, where vortex breakdown is used to mitigate adverse events like flame blow-off and pollutant emissions. On the other hand, increasingly large values of swirl may cause excessive recirculation of combustion products and undesired heating of burner hardware, or flame instabilities. The coupled interaction of swirl and chemical reaction with heat release leads to complex flows that lack a complete understanding, and a more fundamental analysis of the physics is warranted, which serves as the primary motivation for this work.

1.2 Literature review

Before considering swirling jet flames and flame transitions, a basic understanding of vortex breakdown in incompressible swirling jets is required. Difficulty in obtaining a comprehensive understanding of the phenomenon arises from the variety of swirl-production methods and geometrical configurations studied. Controlled physical experiments have been performed in pipes and containers with a rotating end wall while, more recently, unconfined swirling flows have been studied and were found to exhibit entirely new forms of breakdown. The present work will focus on two specific swirling jet configurations:

1. Single jet: a round swirling jet is issued from a nozzle into an unconfined atmosphere. An axisymmetric schematic is shown in Figure 2.1. It should be noted that in this image, the upstream region of the jet nozzle has been excluded. This configuration is primarily used in premixed combustion applications

2. Concentric jets: a central non-swirling jet is surrounded by a coaxial swirling annular jet, and both are issued into an unconfined atmosphere, as shown in the axisymmetric schematic of Figure 2.2. This configuration is used in non-premixed combustion applications

The present study will only consider unconfined jets that discharge into an open atmosphere; effects of radial confinement from combustor walls add further complexity and are thus neglected. The following sections will review previous studies of vortex breakdown in each of the above configurations for incompressible flow, variable-density non-reacting flow, and diffusion flames.

1.2.1 Incompressible flow

Despite numerous theoretical investigations, the mechanism for vortex breakdown is not yet fully agreed upon, as discussed in a variety of reviews (Hall, 1972; Leibovich, 1978, 1984; Escudier, 1988; Althaus et al., 1995; Lucca-Negro and O'Doherty, 2001). One such

theory, proposed by Benjamin (1962), suggests that vortex breakdown can be attributed to a jump in the criticality of the flow and its ability to support infinitesimal standing waves. An alternative theory by Brown and Lopez (1990) is based on the development of negative azimuthal vorticity, and can be summarized as follows. An initial adverse axial pressure gradient, caused by swirl and entrainment in the case of a jet, decelerates the flow, and through continuity, produces a radial outward flow and corresponding opening of the streamsurfaces. From conservation of angular momentum and the vorticity transport equation, the axial vorticity is tilted into negative azimuthal vorticity. This decrease in the azimuthal vorticity further decelerates the axial velocity near the axis, increasing the radially outward flow. This feedback mechanism continues until a stagnation point is formed along with a region of reversed axial flow, known as vortex breakdown. Thus, vortex breakdown represents a special case of flow separation that arises from a centrifugal effect ($\rho v_\theta^2/r > \partial p/\partial r$), which corresponds to a development of radial velocity, analogous to two-dimensional boundary layers (Hall, 1972).

Single jet

Although for the large Reynolds numbers typically found in applications the flow can be expected to be highly turbulent, analyses of laminar configurations can be instrumental in providing fundamental understanding of the flow field. In this chapter, and the remainder of this work, the swirl number S is defined as the ratio of the azimuthal velocity of the rotating jet to the mean axial velocity of the jet (equation (2.22)), and the Reynolds number Re is defined based on the jet radius (equation (2.12)). The seminal experimental investigation by Billant et al. (1998) identified two qualitatively different forms of vortex breakdown in laminar ($150 \leq Re \leq 600$) incompressible swirling jets:

1. bubble vortex breakdown (Figure 1.1)

2. conical vortex breakdown (Figure 1.2),

which possess distinctly different recirculation regions. Based on these observations, a critical swirl number S^* can be defined as the lowest swirl number at which each breakdown first occurs, and the subscripts B and C are used to denote the transition to the bubble and cone states. Starting from a zero-swirl round jet, the swirl was increased, increasing the adverse axial pressure gradient. When the swirl reached the first critical swirl number, S_B^*, the slender pre-breakdown jet transitioned to bubble breakdown, identified by a stagnation point and reversed axial flow. The term bubble breakdown arises from observations by Harvey (1962), who noted this form is "best described as giving the impression that an imaginary body of revolution has been placed on the axis of the vortex around which the fluid is obliged to flow." It is also synonymous with the terms central recirculation zone (CRZ) and inner recirculation zone (IRZ) commonly found in swirling jet literature. As the swirl was increased further, the adverse axial pressure gradient continued to increase, increasing the size of the bubble and shifting the stagnation point upstream. Once the swirl reached a second critical swirl number, S_C^*, the bubble opened into a 90 degree conical sheet. Using the Bernoulli equation along the streamline on the vortex axis and a cyclostrophic balance at an upstream location x_0, a necessary condition for vortex breakdown was derived

$$Si = \frac{\left(\int_0^\infty \frac{v_\theta^2(x_0,r)}{r}\mathrm{d}r\right)^{1/2}}{v_x(x_0,0)} \geq \frac{1}{\sqrt{2}}, \tag{1.1}$$

where Si is an integral swirl number. For a uniform jet in solid body rotation, $S = \sqrt{2}Si$. Billant et al. (1998) reasoned that for cases undergoing conical breakdown, the pressure at the stagnation point reached the ambient value and the criterion reduces to $S_C^* = 1$. For bubble breakdown, the stagnation pressure cannot exceed the surrounding pressure, leading to the weaker condition $S_B^* \geq 1$. For increasing values of Re, the first transition S_B^* initially decreased, before reaching a nearly constant value at larger Reynolds numbers, a result consistent with breakdown in the swirling flow over delta wings, which can be modeled by a Burger's vortex (Spall et al., 1987). Although both recirculation zones were

statistically axisymmetric, a precessing vortex core (PVC) form of each mode was found for larger Reynolds numbers ($Re \geq 400$), during which the stagnation point rotated around the jet axis. Using the same experimental setup, Gallaire et al. (2004) analyzed effects of swirl in both unforced and forced jets at $450 \leq Re \leq 745$. In the weakly swirling unforced jets, axial Kelvin-Helmholtz roll-up dominated the shear layer. As the swirl was increased in the pre-breakdown regime, the trident mode, previously studied by Billant et al. (1998), was identified. Further increase in the swirl led directly to the transition to the cone at S_C^*, so that the bubble was bypassed entirely. The authors also confirmed the negative azimuthal vorticity theory (Brown and Lopez, 1990; Darmofal, 1993; Althaus et al., 1995).

Moise and Mathew (2019) used three-dimensional simulations to numerically study bubble and conical breakdown through a series of simulations at fixed Reynolds number ($Re = 200$) and incrementally increasing values of S. At the fixed inlet plane, the Maxworthy profiles (Ruith et al., 2004) were prescribed, which correspond to smooth profiles for a jet in solid body rotation, originally defined to match the experimental results of Billant et al. (1998). As the swirl was increased to a near-critical value ($S < S_B^*$), a swelling of the streamlines was apparent, and since the Reynolds number was low, the transition from the slender pre-breakdown jet to bubble breakdown at $S_B^* = 1.40$ was gradual. Further increase in swirl revealed the abrupt transition from the bubble to the unsteady cone at $S_C^* = 1.58$. At the transition, the pressure at the stagnation point jumped to the ambient value, confirming the prediction made by Billant et al. (1998). For further increase in S, a second type of conical breakdown was identified, termed the wide-open cone, during which the conical sheet attached to the jet inlet plane. The same authors conducted a similar investigation for a transitional Reynolds number ($Re = 1000$) through large-eddy simulations (Moise and Mathew, 2021). At this moderately large Reynolds number the recirculation zone and wake were turbulent, and critical swirl numbers were lowered considerably compared to the laminar jet. This analysis also suggested that the wide-open cone state might be the result of the Coanda effect that occurs along the fixed inlet plane.

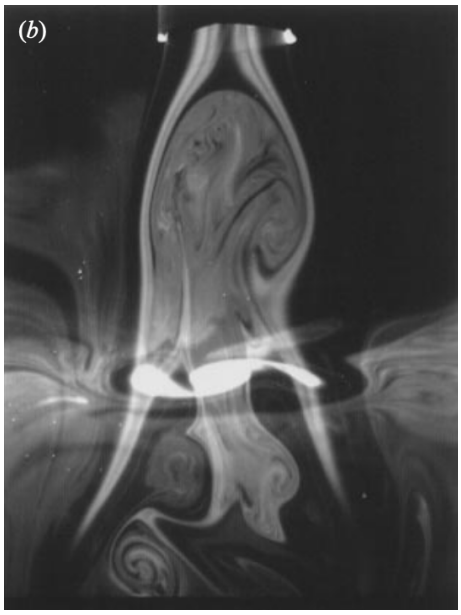

Figure 1.1. Bubble vortex breakdown reproduced from Billant et al. (1998).

Axisymmetric simulations of the same flow were conducted by Ruith et al. (2004). The computations for $S = 1.7$, however, did not detect the conical breakdown that was identified in the three-dimensional (Moise and Mathew, 2019) simulations. Instead, an enlarged two-celled bubble formed. Both of the bubble breakdown cases analyzed, $S = 1.5$ and $S = 1.7$, reached a steady-state in these axisymmetric simulations, unlike the corresponding three-dimensional simulations. Another set of axisymmetric simulations by Fitzgerald et al. (2004) tested a variety of inlet velocity profiles intended to reproduce results by Billant et al. (1998). For ($Re \leq 300$), the simulations were able to successfully reproduce the first critical swirl number S_B^*. For larger Reynolds numbers, bubble breakdown was bypassed and the pre-breakdown state transitioned directly to the cone. This observation is inconsistent with experimental (Billant et al., 1998) and three-dimensional numerical simulations (Moise and Mathew, 2019, 2021) at similar Reynolds numbers. These results suggest that while the final flow state may be statistically axisymmetric, transitions to the cone may involve asymmetric instabilities.

Hysteresis, in which transitions occur at different values of S, depending on whether S is being increased or decreased, was identified experimentally (Billant et al., 1998) and

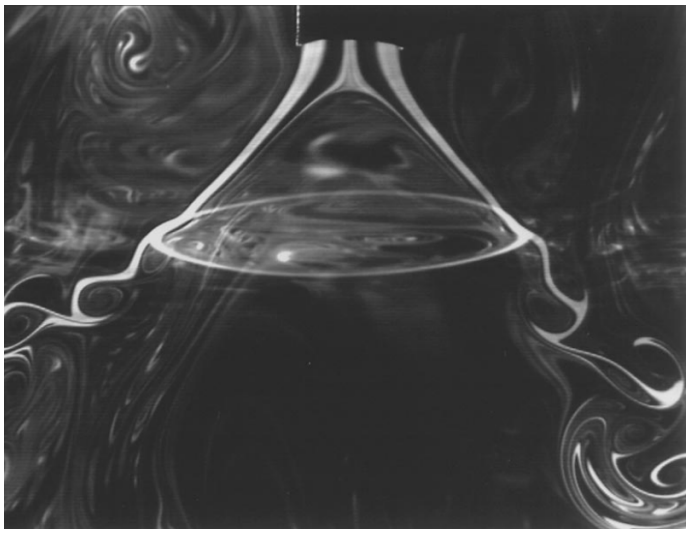

Figure 1.2. Conical vortex breakdown reproduced from Billant et al. (1998).

also studied numerically through time-dependent inflow-swirl computations (Moise, 2020; Moise and Mathew, 2021). These three-dimensional computational results confirmed the bi-stability of the bubble and the cone and emphasized that S^* may depend, in general, on the initial conditions. The analysis by Moise (2020) for $Re = 200$ identified five types of bubble breakdown: steady, one-celled with a spiral tail, pulsating, two-celled with a spiral tail and an asymmetric bubble. The one and two-celled structures were distinguished by the number of toroidal structures in the bubble, and the pulsating form rotated between the two.

The salient flow structures discussed above arise due to the interaction of centrifugal (Leibovich and Stewartson, 1983; Billant and Gallaire, 2013), axial and azimuthal Kelvin-Helmholtz (Loiseleux et al., 1998; Gallaire and Chomaz, 2003; Liang and Maxworthy, 2005), and inertial (Squire, 1960; Benjamin, 1962) instabilities. These modes often interact, leading to the complex flow structures previously mentioned. The resulting dynamics were explored by Douglas et al. (2021) through bifurcation analysis of fully-developed laminar ($Re \leq 150$) swirling jets issuing from a pipe. Unlike the fixed inlet plane employed in previous computations (Ruith et al., 2004; Fitzgerald et al., 2004; Moise and Mathew, 2019; Moise, 2020; Moise and Mathew, 2021), the upstream portion of the pipe was included in the

computational domain. Their steady, axisymmetric base-flow calculations detected the cone, indicating that the flow state is not solely a result of a fixed inflow condition. A later analysis (Douglas and Lesshafft, 2022) suggested that for this flow, the Coanda effect on the walls was the cause of conical breakdown. Clearly confinement effects and the use of a fixed inflow profile affect conical breakdown results, and further analysis is required.

Motivated by applications to combustion, many of the early experimental studies focused on the turbulent regime. Farokhi et al. (1989) used a variable-swirl apparatus at $Re = 187\,500$ to study the downstream mixing for two separate azimuthal velocity profiles: solid body rotation and a free vortex. For the same integral swirl number, the two inflow profiles produced varying time-averaged jet statistics, indicating the sensitivity of the flow to the inlet conditions and that a single swirl number was insufficient to determine the onset of breakdown. The coherent structures in a turbulent ($20\,000 \leq Re \leq 60\,000$) bubble breakdown jet were studied experimentally by Panda and McLaughlin (1994), and it was concluded that the recirculation bubble rapidly increased the turbulence in the jet core as compared to non-swirling jets. The experiments by Oberleithner et al. (2011) at $Re = 10\,000$ identified PVC as a self-excited global mode, and a later analysis at $Re = 1650$ (Oberleithner et al., 2012) validated the criticality theory of Benjamin (1962) by showing that the onset of bubble breakdown at $S = S_B^*$ corresponds to a time-averaged transition from supercritical-to-subcritical flow. As the swirl was increased above S_B^*, the bubble recirculation region grew linearly. Manoharan et al. (2020) reasoned that the unsteady bubble breakdown behaviour at $Re = 29\,500$ is a result of intrinsic changes in the time-averaged state at S_B^*. In this analysis, and others (Panda and McLaughlin, 1994; Billant et al., 1998), the Reynolds numbers were high enough that the stagnation point traveled upstream into the injector for large values of S.

These results indicate that laminar and turbulent swirling jets exhibit remarkable similarities in the bubble vortex breakdown flow structure. While transition values S_B^* are larger for laminar flow, insight can be gained by studying this regime. For highly

turbulent conditions, no signs of conical breakdown were observed, and it remains to be confirmed whether this mode arises due to experimental and numerical setups. In general, the single-jet swirling flow field depends on the two relevant parameters, namely the swirl number S and the Reynolds number Re. While attempts have been made to correlate S for different inflow profiles, the complex nature of the flow prevents a universal swirl number, and separate analysis is required for different flow configurations.

Concentric jets

In the concentric swirling jet configuration, two new parameters arise. The first is the central to outer jet mean velocity ratio U_c'/U_j', and the second is the ratio of the injector radii, R_c'/R_j', the latter of which is often fixed due to experimental constraints. The former is commonly expressed in terms of a mass flow rate $\dot{m}_c'/\dot{m}_j'$, or the global equivalence ratio ϕ_0 in combustion applications, to be discussed later. Combined effects of swirl and the velocity ratio are also frequently discussed in terms of a modified Rossby number (Giannadakis et al., 2008; Santhosh et al., 2014), $Ro = |\Delta v_x|/v_{\theta,avg}$, where $\Delta v_x = |U_j' - U_c'|/U_j'$ is the dimensionless velocity difference, and $v_{\theta,avg}$ is the dimensionless spatially averaged azimuthal velocity. This dimensionless number effectively provides a measure of the axial and radial pressure gradient.

Because of the increased complexity in the two-jet flow, early analysis focused on mixing and instabilities in the non-swirling case (Chigier and Beér, 1964; Werner et al., 1992; Balarac and Metais, 2005). By adding swirl to the annular stream, Champagne and Kromat (2000) studied the transition to bubble breakdown through experiments for fixed $R_c'/R_j' = 0.25$ and $Re = 13\,000$ at different values of S and U_c'/U_j'. In the pre-breakdown regime, an increase in S was found to decrease the required distance for the merging of the inner and outer jets. Further increase in S to S_B^* resulted in a bubble breakdown with a stagnation point located close the jet exit plane. During this transition, the rms axial and radial velocity fluctuations in the bubble increased considerably, and

were found to be in good agreement with the comparable single jet experiment by Panda and McLaughlin (1994). The same vortex breakdown modes observed in single jets, the bubble and the cone, were identified in the concentric jet configuration by Santhosh et al. (2014), and their associated transitions S_B^* and S_C^* were examined through through time-averaged two-dimensional particle image velocimetry (PIV). In this experiment, the swirl was generated by tangential entry inlets in the annular jet, a common technique used in gas turbine combustors. The bubble breakdown flows took a variety of complex forms that differed from the single jet configuration, and the transition to the cone was found to occur during a rapid increase in a newly defined non-dimensional swirl momentum factor. Using the same experimental setup, this group further explored the transition to the cone through time-resolved PIV (Rajamanickam and Basu, 2018), and showed that the sudden transition to the cone was associated with a rapid increase in vortex shedding modes. The precise mechanism for the onset of the cone, however, was not clear. In both of these works, hysteresis was present, similar to that discussed in the single jet configuration.

More recently, numerical simulations have been used to study turbulent concentric swirling jets. Kadu et al. (2019) investigated passive scalar mixing through direct numerical simulations (DNS) at $Re = 5720$, and later used a spectral proper orthogonal decomposition (SPOD) to identify the counter-rotating vortex pairs in a partially-penetrated breakdown bubble (Kadu et al., 2020). The same experiments conducted by Santhosh et al. (2014) and Rajamanickam and Basu (2018) were also studied numerically by Pattanshetti et al. (2022) in order to assess turbulence models for the Reynolds-Averaged Navier-Stokes equations. While numerical simulations of the turbulent flow are useful to uncover the dynamics for a specific set of parameters, the breakdown transitions and their origin remain elusive due to the high computational cost of running multiple simulations. Numerical simulations have been conducted for the laminar flow (Montagnani and Auteri, 2019), although only for pre-breakdown swirl levels. No such analysis exists in the post-breakdown regime.

The two primary vortex breakdown modes found in single jets, the bubble and the

cone, have been identified in concentric swirling jets. Depending on its strength, the central fuel jet may penetrate the breakdown bubble, and alter the flow pattern found in single jet configurations. Conical breakdown, on the other hand, exhibits the same qualitative form as the single jet configuration. Nearly all of the previous work has focused on the turbulent flow-field.

1.2.2 Variable-density non-reacting flow

In a combustion chamber, the density exhibits large spatial variations, exceeding a factor of five, associated with the temperature changes induced by the chemical heat release. There is interest therefore in first studying primary effects of variable density on vortex breakdown in low-Mach-number gaseous swirling jets.

Single jet

The convective/absolute stability of a typical bubble breakdown encountered in lean premixed combustion was studied by Manoharan et al. (2015). The authors showed that the density gradient in the inner shear layer stabilized the co-rotating $|m| = 1$ absolute instability, in agreement with the suppression of the PVC encountered in flames. Similar to previous works, to avoid confusion on sign convention, a helical instability will be described by the magnitude of the azimuthal wavenumber $|m|$, as well as its sense of temporal (rotation) and spatial (winding) variation, both of which will use the prefix co- for the direction of swirl, and counter- for the opposing direction. Adzlan and Gotoda (2012) analyzed vortex breakdown flows in a co-axial jet configuration, with swirl only imparted on the central stream. Thus, for zero-coflow, the experimental setup resembled that of a single jet in solid body rotation. Density changes were introduced by using either an air or carbon-dioxide central jet, which was surrounded by the coaxial air jet. The experiments revealed that the higher density (lower viscosity) carbon-dioxide jet exhibits a greater degree of flow divergence and lower critical swirl numbers than the air jet and that increasing the coflow decreases the flow divergence, and tends to suppress vortex breakdown. Both conical breakdown, and

what appears to be the wide-open cone, were observed for small values of the coflow velocity. The effects of buoyancy were non-negligible for these low-Reynolds number ($Re \leq 469$) experiments, and the jet-to-ambient density ratio was small (1.53), far below values realistic for combustion.

1.2.3 Diffusion flames

Unlike the variable-density flows considered above, the density and temperature variation across a jet diffusion flame are no longer monotonic, and the swirling flow field interacts with chemical reaction and the resulting heat release to modify vortex breakdown. The resulting flow field affects key areas of combustion performance such as flame stability (lift-off and blow-off), thermal stress on combustion hardware, and pollutant (NO_x) formation.

It is first useful to consider the stabilization mechanism of non-swirling jet diffusion flames, which can be assessed based on whether the flame is attached, lifted, or blown-off, all of which are summarized below (Liñán et al., 2015). After ignition, for sufficiently fast chemistry, the laminar diffusion flame exists in a sheet located where the fuel and oxygen are in stoichiometric proportions, except in the vicinity of the inlet, where it takes the form of a planar premixed flame that moves relative to the flow with a propagation velocity that is a function of the upstream velocity, temperature and composition. Since the laminar flame speed S_L' decreases for non-stoichiometric proportions of fuel and oxygen (Williams, 1985), the rich and lean branches of the planar premixed flame curve downstream. Oxygen and fuel are completely consumed on the rich and lean branches, respectively, and a trailing diffusion flame forms behind the premixed front. This triple flame structure depends critically upon the Damköhler number D_N, a ratio of the stoichiometric flame speed to the jet inlet velocity (equation (2.16)). For sufficiently large values D_N, the radius of curvature of the triple flame is comparable to the flame-front thickness, and an attached edge flame (Buckmaster, 2002) sits near the injector. For decreasing values D_N, the flame lifts off the injector, and the triple flame stabilizes at a downstream distance known as the liftoff height, redirecting the

upstream flow at the base of the flame (Ruetsch et al., 1995). Further decrease in D_N leads to a lean premixed front with a negligibly weak trailing diffusion flame, followed by a critical value $D_{N,b}$ for which blow-off occurs.

Single jet

The effect of weak swirl (pre-breakdown) on lifted laminar and turbulent propane flames was investigated experimentally by Cha et al. (1999) for a rotating nozzle configuration similar to that considered in the numerical study on isothermal swirling jets by Douglas et al. (2021). In the non-swirling case, a lifted triple flame is stabilized downstream of the fuel jet exit. For increasing values of S, air entrainment increased, decelerating the axial flow and reducing the liftoff height as a non-linear function of S. For post-breakdown levels of swirl, Qadri (2014) calculated a base flow with a triple flame positioned just outside of the bubble, and performed global stability analysis to show that the flame was unstable to a counter-rotating $|m| = 1$ mode

Concentric jets

In practical applications, concentric jets are used so that the flame base, located between the two jets in the inner shear layer, coincides with the primary swirl-induced deceleration of the flow. In an early experimental study on the flame aerodynamics, Claypole and Syred (1981) identified four distinct flame types as a function of the inflow swirl. At pre-breakdown swirl levels, a jet-like flame formed; these flames are typically undesirable, but may be found in smaller combustors where the Reynolds number is low and critical swirl numbers S_B^* are high. For $S \geq S_B^*$, three distinct flame types were found depending on whether the flame was positioned downstream, on the boundary, or upstream of the recirculation zone. Tangirala et al. (1987) found that breakdown considerably reduced the flame height, but for values $S \gg S_B^*$, the recirculation zone strength and flame height remained relatively constant, and were accompanied by undesired heating of the burner. Although no conical breakdown was observed at these large values of S, this may be influenced by

the diverging quarl placed at the burner exit, which is often used to enhance flame stability. Effects of this specific geometry have previously been explored experimentally by Degenève et al. (2019a), but the focus of this work is on the purely unconfined flame, to provide a more basic understanding of the physics. A subsequent experimental investigation by Tangirala and Driscoll (1988) classified four distinct flame types for various levels of inflow swirl and jet velocity ratio U_c'/U_j'. Excessive fuel jet velocity led to a penetration and weakening of the recirculation zone, lowering the centerline temperature. Increasing swirl, on the other hand, strengthened the recirculation zone, leading to hotter more compact flames with increased turbulent intensities. A similar experimental investigation (Chen and Driscoll, 1989) analyzed effects of the mean flow on flame shape, also including an analysis of flame-height scaling laws.

Three types of blow-off limits have been identified in non-premixed swirling flames. The first, rich blow-off, occurs for increasing values of the fuel jet velocity. In the experimental investigation by Feikema et al. (1990), the maximum fuel velocity at blow-off was measured for various levels of S, R_c'/R_j', fuel type, and U_c'/U_j'. The recirculation zone for $S \geq S_B^*$ was found to reduce the centerline fuel jet velocity, thus improving rich blow-off limits. A second form of blow-off, known as lean blow-off, occurs for excessively large values of the air coflow velocity. Both Yuasa (1986) and Feikema et al. (1991) experimentally quantified the improved lean blow-off limits that occur after the formation of breakdown, the latter focusing on increasing coflow to reduce NO_x emission. A similar result was obtained by Saediamiri et al. (2014) for biogas flames, which are inherently unstable due to their low burning velocity. Tummers et al. (2009) used an experimental setup with a rotating air pipe, unlike the conventional tangential entry methods discussed above. The fuel was issued in an annular channel which led to a transition between a lifted vortex breakdown flame and a bluff body stabilized flame, with both flame types occurring for the same conditions depending on whether the fuel flow rate was increasing or decreasing. Blow-off limits were measured by simultaneously increasing both the fuel and air flow rates while maintaining

a constant global equivalence ratio. The last blow-off limit, excessive swirl, has been the subject of a more recent experimental investigation by Santhosh and Basu (2016). Increasing levels of swirl led to flame transitions between lifted and attached flames, but the exact mechanisms for the transitions were unclear. One specific flame identified at low levels of swirl was lifted off the injector, with a recirculation zone forming just upstream of the maximum heat release. At the extreme swirl limit, excessive straining of the flame led to blow-off. Conical breakdown was not detected in this work, or any of the other flames mentioned in this section. It was however, reported in studies of incompressible flow (Santhosh et al., 2014; Rajamanickam and Basu, 2018) that use the same experimental setup.

The high pressures used in practical gas-turbines lead to thin flames that are computationally challenging to resolve. DNS is typically intractable at the Reynolds numbers encountered in these applications, although simplifications or modeling of turbulence may be used to numerically study these flames. By considering a moderately large Reynolds number ($Re = 1925$), Xiao et al. (2021) studied the effects of turbulence on a concentric swirling jet flame with radial confinement, showing the strong role of dilatation and baroclinic torque. Large eddy simulation (LES) were used by Dagan et al. (2016) to analyze the dominant structures in a more practical confined concentric jet flame at $Re = 49\,219$. The non-swirling and swirling cases studied were found to exhibit quenching near the fuel inlet, leading to an axially asymmetric flame.

For oxygen-enriched flames at different values of S and U_c'/U_j', Degenève et al. (2019b) proposed a scaling relationship for the flame height that accounted for the increased turbulent diffusion associated with pre-breakdown swirl levels. A subsequent paper (Degenève et al., 2019a) studied the effects of co-rotating swirl on the central fuel jet. With zero fuel-jet swirl, as is the case in the present investigation, all flames remained attached to the burner. When swirl was added to the central jet, compact bubble breakdown lifted flames were generated. This analysis was continued to include the effects of counter-rotation of the central jet (Degenève et al., 2021), which effectively decreased the strength of the recir-

culation zone. Oxygen-enriched flames significantly alter the location of the reaction with respect the recirculation region, and thus care must be taken in drawing conclusions from these studies.

1.3 Summary and open issues

Turbulent vortex breakdown flame transitions have received considerable attention, but the fundamental influence of swirl on stabilization lacks a complete understanding, and can be better understood through analysis of laminar configurations. For the single swirling jet, these breakdown transitions have recently been investigated through both axisymmetric (Douglas et al., 2021; Douglas and Lesshafft, 2022) and three-dimensional (Moise and Mathew, 2019; Moise, 2020) numerical simulations of the isothermal flow. Effects of non-uniform temperature and heat release, however, have not yet been explored, and warrant further analysis. In the swirling concentric jet configuration, there are no fundamental studies of the laminar flow field with or without heat release. These results would provide insight into the basic mechanism by which swirl enhances flame-stability. Simplification of these problems to both axisymmetric and steady forms may provide further insight into the underlying physics, while also reducing the computational cost.

1.4 Objectives

The overall objective of this work is to investigate vortex breakdown in swirling jets and swirling jet diffusion flames using numerical simulations. Because of the complex nature of turbulent swirling flames and incomplete existing knowledge, laminar and transitional flow regimes will be considered. A fundamental study of vortex breakdown and flame behaviour is carried out through a systematic approach with increasing levels of physical and computational complexity. There are three primary objectives of this research, that will be outlined below.

The first objective is to understand the effects of temperature variation on both

vortex breakdown modes. This is done by extending previous studies of laminar single swirling jets to account for effects of variable temperature (density). Axisymmetric and three-dimensional numerical simulations of heated and cooled gaseous single jets are conducted, with temperature ratios representative of combustion, which serves as an intermediate step towards understanding the behavior associated with flames. These simulations are supplemented with theoretical predictions for the onset of bubble breakdown by reducing the Navier-Stokes (NS) equations to a parabolic problem analogous to boundary layer flow. Results for the isothermal jet are used to validate the simulations. This work is presented in chapter 3.

The second objective, discussed in chapter 4, is to study the same single swirling jet flow in the presence of a non-premixed flame, so that realistic temperature variation is accounted for. To focus on the fluid mechanics, the analysis assumes that methane reacts with air according to an irreversible reaction in the Burke-Schumann limit of infinitely fast chemistry. The physics of these burner-attached flames, including effects of the thermochemistry, are explored using the same numerical and theoretical techniques. Vortex breakdown transitions are identified and their impact on the flame shape is discussed.

Both of the previous objectives relate to fundamental studies on the interaction of temperature variation and vortex breakdown. The third and final objective extends these studies to consider non-premixed swirling flames in more realistic gas-turbine geometry, namely the concentric jet configuration. Similar to the procedure for single jets, the analysis begins by studying the axisymmetric laminar flow for isothermal and Burke-Schumann cases, and will then consider finite-rate chemistry. This analysis includes calculations of critical swirl numbers, liftoff heights and blow-off limits, all of which provide fundamental insight into these phenomena in turbulent flames. To present a more complete picture of these flows, three-dimensional simulations at moderately large Reynolds numbers are used to supplement the axisymmetric analysis. These results are presented in chapter 5, and comparisons are made with single jet vortex breakdown modes.

The remainder of the dissertation is organized as follows. Chapter 2 will introduce the governing equations and solution technique. In chapter 3, results will be presented for the variable-density single jets, followed by Burke-Schumann single jet swirling flames in chapter 4. The results for concentric jet flows and flames will be presented in chapter 5. The work will be summarized in chapter 6, along with a discussion of possible future work.

Chapter 2

Mathematical formulation and numerical simulations

This chapter describes the basic physical problem, mathematical formulation and numerical solution procedure for the general unsteady three-dimensional reacting flow considered. Since the three objectives described in chapter 1 involves different flow/computations, additional specific information on each of these sets of simulations is provided in the corresponding chapters.

2.1 Flow configuration

Schematics for the two flow configurations used in this study, the single swirling jet and the concentric swirling jets, are shown in Figures 2.1 and 2.2, respectively (axisymmetric representation shown). In the single jet configuration, the upstream flow in the jet nozzle and surrounding atmosphere is replaced by a fixed inflow plane. For the reacting flows, the fuel-feed stream is the swirling jet which flows into the surrounding air. The jet properties in this configuration are denoted by the subscript j. In the concentric jet configuration, on the other hand, the computational domain extends upstream to include both the injectors and surrounding atmosphere, as is needed for a correct description of vortex breakdown when the stagnation point moves close to the jet discharge plane. The annular jet serves as the primary jet, and is again denoted by the subscript j, while the central jet uses the subscript c. The walls of the injectors have a small thickness $e' = 0.01R'_j$ (dimensional variables are

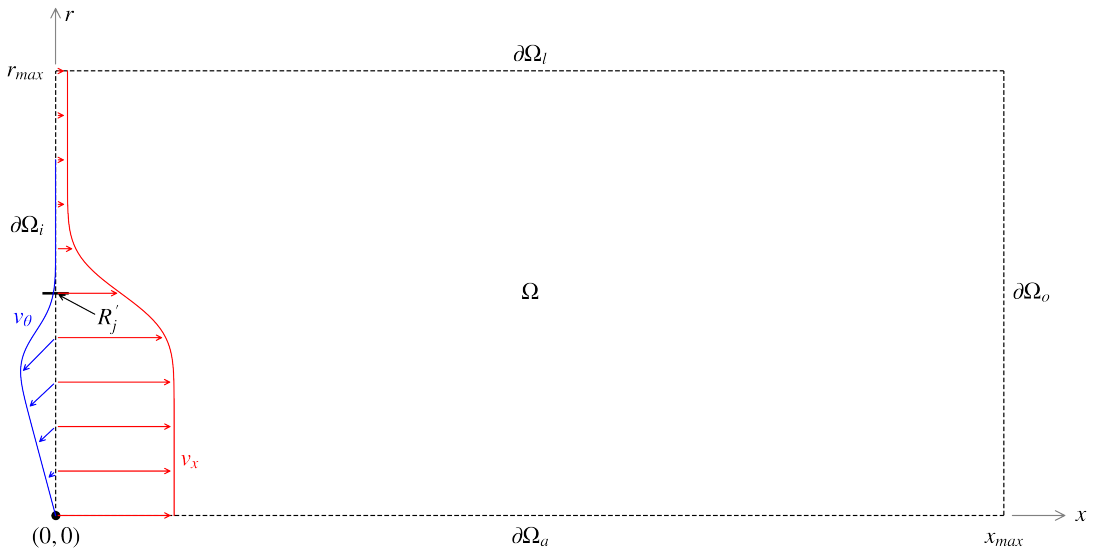

Figure 2.1. Schematic of axisymmetric single swirling jet configuration. The region upstream of the nozzle has been truncated to the inlet plane $\partial\Omega_i$.

denoted with a prime $'$). To minimize the wake of the injectors at the jet exit plane, the injector walls are tapered near the end, as indicated in Figure 2.2, with the resulting spire aspect ratio taking the value $d'/e' = 20$. The taper direction was selected for consistency with previous computations of non-swirling jet flames (Moreno-Boza et al., 2016), and is expected to have negligible effect given the small thickness of the injector. In the reacting flows, the fuel-feed stream is the central non-swirling jet, and the air-feed stream is the co-axial swirling annular jet, both issuing into the surrounding air. All computational domains Ω were built with GMSH (Geuzaine and Remacle, 2009), and will be discussed separately in each chapter.

2.2 Governing equations

The flows considered in this study are low-Mach-number, viscous, gaseous, chemically reactive flows with no external forces. The governing equations are the time-dependent, three-dimensional conservation equations for density, momentum and energy.

Consideration is given to diluted and undiluted methane-air systems, so that the mass fractions of methane (Y_{F}) and oxygen ($Y_{\mathrm{O_2}}$) take the values $Y_{\mathrm{F},F} \leq 1$ and $Y_{\mathrm{O_2},A} = 0.23$

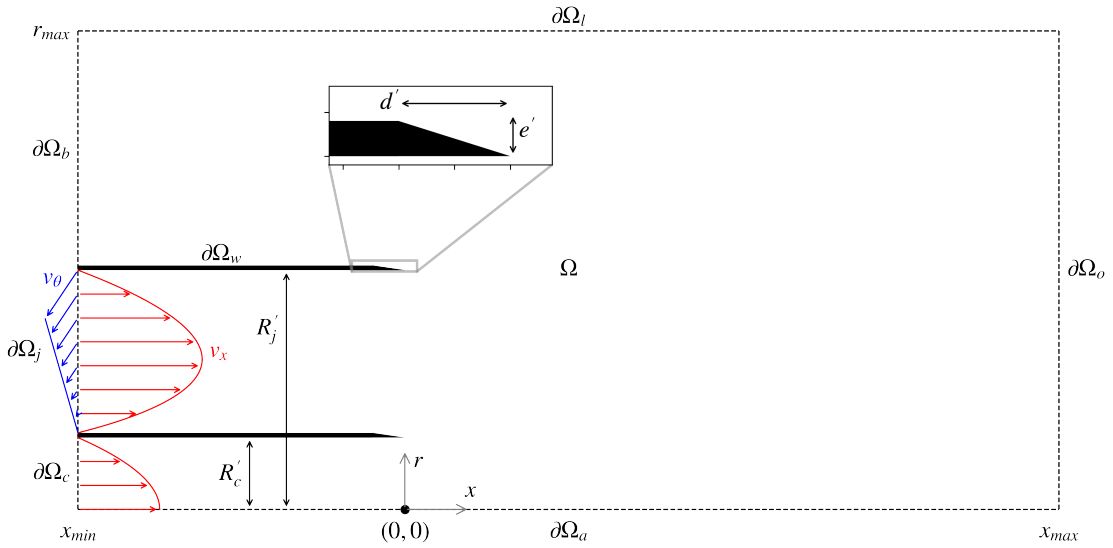

Figure 2.2. Schematic of axisymmetric concentric swirling jet configuration.

in their feed streams. All gases are supplied at a jet temperature T_j' equal to the temperature in the surrounding ambient air T_a', except in the non-reactive variable-density problem, to be discussed chapter 3. Soret, Dufour, and pressure gradient diffusion effects will all be neglected.

The description assumes that the fuel reacts with the oxygen of the air according to the overall irreversible reaction

$$\mathrm{F} + s\,\mathrm{O}_2 \rightarrow (1+s)\,\mathrm{P} + Q', \tag{2.1}$$

with P, s, and Q' representing, respectively, the combustion products (carbon dioxide and water vapor), the mass of oxygen required to burn a unit mass of fuel, and the heat released per unit mass of fuel burnt. The dimensionless heat of reaction is $q = (Q'Y_{\mathrm{F},F})/(c_p'T_a')$, where the specific heat at constant pressure, c_p', is assumed to be constant. For unity Lewis numbers ($Le = Sc/Pr = 1$), an excellent approximation for methane-air combustion (Smooke, 1991), the mass fraction of fuel Y_{F} and oxygen Y_{O_2} can be computed in terms of

the temperature and the mixture fraction (Liñán et al., 2015)

$$Z = \frac{sY_{\mathrm{F}} - Y_{\mathrm{O}_2} + Y_{\mathrm{O}_2,A}}{sY_{\mathrm{F},F} + Y_{\mathrm{O}_2,A}} = \frac{T-1}{q} + \frac{Y_{\mathrm{F}}}{Y_{\mathrm{F},F}}, \tag{2.2}$$

which has been normalized to be unity in the fuel stream and zero in the air stream. The dimensionless temperature T has been normalized by T_j'. The fuel consumption rate (moles per unit volume per unit time) is assumed to take the Arrhenius form

$$\omega' = B' C_{\mathrm{F}}' C_{\mathrm{O}_2}' \mathrm{e}^{-T_a/T} \tag{2.3}$$

where C_{F}' and C_{O_2}' are the concentration of fuel and oxygen, respectively, B' is the frequency factor, and T_a is the dimensionless activation temperature. (not to be confused with the ambient air temperature T_a'). To enable accurate descriptions of partially premixed combustion, following Fernández-Tarrazo et al. (2006a) the activation temperature is allowed to vary with the local equivalence ratio $\phi = (sY_{\mathrm{F},F}/Y_{\mathrm{O}_2,A})Z/(1-Z)$ according to the equations

$$T_a/T_{a,0} = \begin{cases} 1 + 2(0.7-\phi)^2 & \text{for } \phi \le 0.7 \\ 1 & \text{for } 0.7 \le \phi \le 1.0 \\ 1 + 1.472(\phi-1)^2 & \text{for } 1.0 \le \phi \end{cases} \tag{2.4}$$

which effectively mimic changes in the chemistry occurring in rich and lean branches of the flame, with $T_{a,0} = 50.11$ selected to match the stoichiometric burning velocity for methane (Liñán et al., 2005). The stoichiometric value of the mixture fraction is

$$Z_s = \frac{1}{sY_{\mathrm{F},F}/Y_{\mathrm{O}_2,A} + 1}, \tag{2.5}$$

and the adiabatic flame temperature is $T_s = 1 + \gamma$, with the parameter

$$\gamma = qZ_s \tag{2.6}$$

measuring the exothermicity of the reaction. For a given fuel-feed mass fraction $Y_{\mathrm{F},F}$, the thermochemical parameters Z_s and γ can be evaluated from (2.5) and (2.6). For methane (i.e. $s = 4$ and $Q' = 50\,150$ kJ/kg) with a feed temperature $T'_j = 300$ K and a presumed average specific heat $c'_p = 1.4\,\mathrm{kJ/(kg \cdot K)}$, it follows that $Z_s = (0.365, 0.223, 0.103, 0.054)$ and $\gamma = (4.36, 5.33, 6.16, 6.49)$ for values $Y_{\mathrm{F},F} = (0.1, 0.2, 0.5, 1.0)$. The stoichiometric value of Zeldovich number is $\beta_s = T_{a,0}\gamma/T_s^2$ and $\alpha = \gamma/T_s$ is the heat release parameter. The simplified chemistry described above has also been used to successfully describe liftoff and blowoff in planar mixing layers (Fernández-Tarrazo et al., 2006b).

In the low-Mach-number formulation (Majda and Sethian, 1985), perturbation methods are used to decouple acoustic waves from the Navier-Stokes equations. The pressure is split into a spatially uniform thermodynamic pressure p_0 and a hydrodynamic pressure p_1

$$p = p_0(t) + \gamma_c Ma^2 p_1(\boldsymbol{x}, t), \tag{2.7}$$

where γ_c is the ratio of specific heats, and Ma is the Mach number. The subscript 1 will be dropped from the hydrodynamic pressure in the remainder of this work for convenience. For the unconfined atmospheric flames considered, the thermodynamic pressure is assumed constant ($\mathrm{d}p_0/\mathrm{d}t = 0$).

The inner radius of the jet R'_j (see Figures 2.1 and 2.2) and the mean jet velocity U'_j (volume flow rate divided by cross-sectional area) will be used to scale the cylindrical coordinates $\boldsymbol{x} = (x, \theta, r)$ and accompanying velocity components $\boldsymbol{v} = (v_x, v_\theta, v_r)$. Correspondingly, the dimensionless time t is scaled with the residence time R'_j/U'_j. The jet values of the density ρ'_j, viscosity μ'_j, and thermal conductivity k'_j will be used to define the dimensionless mixture density ρ, viscosity μ, and thermal conductivity k, respectively. In terms of these variables, the non-dimensional Navier-Stokes, energy and species concentration equations, written in the low-Mach-number approximation for unity Lewis number, take the

dimensionless form

$$\frac{\partial \rho}{\partial t} + \boldsymbol{\nabla} \cdot (\rho \boldsymbol{v}) = 0 \tag{2.8}$$

$$\rho \left(\frac{\partial \boldsymbol{v}}{\partial t} + \boldsymbol{v} \cdot \boldsymbol{\nabla} \boldsymbol{v} \right) = -\nabla p + \frac{1}{Re} \boldsymbol{\nabla} \cdot \tau \tag{2.9}$$

$$\rho \left(\frac{\partial T}{\partial t} + \boldsymbol{v} \cdot \boldsymbol{\nabla} T \right) = \frac{1}{Re\, Pr} \nabla \cdot (k \boldsymbol{\nabla} T) + q D_N \omega \tag{2.10}$$

$$\rho \left(\frac{\partial Z}{\partial t} + \boldsymbol{v} \cdot \boldsymbol{\nabla} Z \right) = \frac{1}{Re\, Pr} \nabla \cdot (k \boldsymbol{\nabla} Z), \tag{2.11}$$

where

$$Re = \frac{\rho_j' U_j' R_j'}{\mu_j'} \tag{2.12}$$

is the Reynolds number defined based on the properties of the jet stream, $Pr = \mu_j' c_p' / k_j' = 0.72$ is the Prandtl number, $\tau = \mu[\boldsymbol{\nabla} \boldsymbol{v} + \boldsymbol{\nabla} \boldsymbol{v}^T - 2(\boldsymbol{\nabla} \cdot \boldsymbol{v})\mathbf{I}/3]$ represents the dimensionless viscous stress tensor, and p is the pressure difference with respect to the ambient value, scaled with the characteristic dynamic pressure $\rho_j' U_j'^2$. Neglecting variations in the mean molecular weight, a reasonably good approximation for methane-air combustion, the ideal gas equation of state in the low-Mach-number limit takes the dimensionless form

$$\rho T = 1. \tag{2.13}$$

The viscosity and thermal conductivity are assumed to vary with temperature according to the power-law expressions

$$\mu = k = T^\sigma, \tag{2.14}$$

with a value $\sigma = 0.7$ selected for the exponent, an appropriate value given the high concentration of air in the mixture. Based on the normalization given above, the Péclet number $Pe = RePr = R_j' U_j' / D_{T,j}'$ can be introduced into the definition of the non-dimensional fuel consumption rate

$$\omega = \frac{Pe \beta_s^3 T_s}{4(1 - Z_s) Y_{\mathrm{O_2,A}}} \rho^2 Y_{\mathrm{F}} Y_{\mathrm{O_2}} \exp(\beta_s/\alpha - T_a/T), \tag{2.15}$$

so that the associated Damköhler number becomes

$$D_N = \left(\frac{S'_{L,s,\infty}}{U'_j} \right)^2 , \tag{2.16}$$

where $S'_{L,s,\infty} = [4(1-Z_s)\beta_s^{-3} T_s^{-1} \hat{B}' D'_{T,j} Y_{O_2,A} \exp(-\beta_s/\alpha)]^{1/2}$ denotes the stoichiometric value of the burning velocity as obtained at leading order in the asymptotic limit of large activation energy (Williams, 1985), $\hat{B}' = \rho'_j B'/W'_{O_2}$ is a normalized frequency factor, W'_{O_2} is the molecular weight of oxygen and $D'_{T,j} = k'_j/(\rho'_j c'_p)$ is the thermal diffusivity in the air-jet stream. Since lifted flames propagate at velocities that are of the order of the planar-flame propagation velocity (Liñán et al., 2015), it can be anticipated that the scaling selected results in order-unity values of the critical Damköhler number characterizing flame liftoff and blowoff.

A special limiting case occurs as $D_N \to \infty$, known as the Burke-Schumann limit of infinitely fast chemistry (Burke and Schumann, 1928), in which the flame appears as an infinitesimally thin layer (a flame sheet) separating the fuel from the oxygen, and the composition and temperature can be described in terms of conserved scalars (Liñán et al., 2015). If the injectors are adiabatic, then the solution further reduces to a single scalar, the mixture fraction, governed by the chemistry-free transport equation (2.11). At the flame, where $Y_{\mathrm{F}} = Y_{\mathrm{O}_2} = 0$, the mixture fraction takes the value $Z = Z_s$ while the temperature reaches the adiabatic maximum value $T = T_s$. Since $Y_{\mathrm{F}} = 0$ on the air side, where $Z < Z_s$, while $Y_{\mathrm{O}_2} = 0$ on the fuel side, where $Z > Z_s$, it follows from (2.2) that

$$T = 1 + \gamma \frac{Z}{Z_s} \qquad \text{for} \quad Z \le Z_s \tag{2.17}$$

$$T = 1 + \gamma \frac{1-Z}{1-Z_s} \qquad \text{for} \quad Z \ge Z_s. \tag{2.18}$$

and only (2.8), (2.9), (2.11) and (2.13) are needed to complete the system. From the piecewise linear relations (2.17) and (2.18), the derivative of the temperature with respect to

the mixture fraction involves a discontinuity represented by a Heaviside function. Following previous numerical studies (Higuera and Moser, 1994), to facilitate numerical convergence, the Heaviside function is replaced by a smooth hyperbolic tangent function

$$H(Z - Z_s) = \frac{1}{2}\tanh(\xi Z - \xi Z_s) + \frac{1}{2}, \tag{2.19}$$

where ξ^{-1} represents a non-dimensional flame width in mixture fraction space. The smooth temperature derivative

$$\frac{\mathrm{d}T}{\mathrm{d}Z} = \frac{\gamma}{Z_s} - \left[\frac{1}{2}\tanh(\xi Z - \xi Z_s) + \frac{1}{2}\right]\left[\frac{\gamma}{1 - Z_s} + \frac{\gamma}{Z_s}\right], \tag{2.20}$$

can be integrated to obtain the temperature distribution as a function of the mixture fraction

$$T = 1 + \frac{\gamma}{Z_s}Z + \frac{1}{2}\left[\frac{\gamma}{1 - Z_s} + \frac{\gamma}{Z_s}\right]\left(\frac{\ln(\cosh[\xi Z_s])}{\xi} - \frac{\ln(\cosh[\xi Z_s - \xi Z])}{\xi} - Z\right). \tag{2.21}$$

For small flame thickness ξ^{-1}, temperature and density gradients increase and additional computational resources are required to resolve the grid across the flame. Large values of ξ^{-1}, on the other hand, decrease the adiabatic flame temperature and present an artificial smoothing that may affect the numerical results. The values $\xi = 50$ and 500 were used in chapters 4 and 5, respectively, and validation is provided in the corresponding chapters.

2.3 Boundary conditions

Boundary conditions for $\boldsymbol{v}$, T and Z are specified along the boundaries $\partial\Omega$ of the computational domain Ω (see Figures 2.1 and 2.2).

2.3.1 Swirl number

For both configurations, swirl is imparted on the flow by rotating a nozzle with angular speed Ω' (clockwise in the $y-z$ plane). The swirl number is selected to be consistent

with previous numerical studies (Ruith et al., 2004; Moise and Mathew, 2019; Moise, 2020; Moise and Mathew, 2021), and is defined by the ratio of the azimuthal velocity of the pipe to the mean axial velocity of the jet U_j', so that

$$S = \frac{\Omega' R_j'}{U_j'}. \tag{2.22}$$

Although the swirl number S is often defined as the ratio of the axial flux of angular momentum to the axial flux of axial momentum (Vignat et al., 2022), the simplified ratio is retained in this analysis to provide consistency with previous numerical studies of single (Ruith et al., 2004; Moise and Mathew, 2019; Moise, 2020; Douglas et al., 2021; Moise and Mathew, 2021) and annular (Douglas et al., 2022) swirling jets.

2.3.2 Inlet: single swirling jets

The single jet configuration considers a swirling jet under solid-body rotation surrounded by a negligible swirl-free coaxial stream with velocity $\epsilon U_j'$. To facilitate computations, smooth radial distributions of axial and azimuthal velocity components v_x and v_θ, given by the so-called Maxworthy profiles (Ruith et al., 2004) were prescribed at the inflow boundary $\partial\Omega_i$, and the radial velocity v_r was set equal to zero. Thus, at $x = 0$ for $0 \leq r \leq r_{\max}$,

$$v_x = (1-\epsilon)\left[\frac{1}{2}\mathrm{erfc}\left(\frac{r-1}{\delta}\right)\right] + \epsilon \tag{2.23}$$

$$v_r = 0 \tag{2.24}$$

$$v_\theta = \frac{Sr}{2}\mathrm{erfc}\left(\frac{r-1}{\delta}\right). \tag{2.25}$$

Here erfc is the complementary error function, and δ represents the relative thickness of the mixing layer separating the jet from the coflow ϵ. Note that the canonical case of a jet with uniform velocity and solid-body rotation discharging into a stagnant atmosphere is

recovered from the above expressions by taking the limit $\epsilon \ll 1$ and $\delta \ll 1$. Unless otherwise specified, the values $\delta = 0.2$ and $\epsilon = 0.01$ were used for consistency with previous numerical studies (Moise and Mathew, 2019; Moise, 2020; Moise and Mathew, 2021). In chapter 3, effects of these parameters on critical swirl numbers will be identified. It should also be noted that given the smooth nature of the azimuthal velocity profile, the peak azimuthal velocity at the inflow only reaches the value S in the limiting case $\delta \to 0$.

As discussed by Moise and Mathew (2019), the use of a prescribed velocity field at the inlet plane is questionable for cases when the breakdown occurs near the inlet, since the downstream evolution then may be expected to modify the flow field upstream from this boundary, but accounting for such effects can complicate computations. This will be addressed in the concentric jet configuration.

The temperature (or mixture fraction) must be prescribed at the Dirichlet inlet $\partial\Omega_i$. For the low-Mach-number gaseous jets considered in chapter 3, differences in density emerge in connection with differences in temperature between the jet and the ambient gas. The jet is issued at temperature T_j' and is surrounded by a negligible ambient coflow of the same gas at temperature T_a', so that the boundary temperatures are related to the jet-to-ambient density ratio ρ_j'/ρ_a' by

$$\Lambda = \frac{\rho_j'}{\rho_a'} = \frac{T_a'}{T_j'}. \tag{2.26}$$

Thus, for heated jets, $\Lambda < 1$, and for cooled jets, $\Lambda > 1$. For consistency, the same mixing-layer thickness δ used in (2.23) is used to define the associated inflow boundary ($\partial\Omega_i$) temperature profile

$$T = (1 - \Lambda)\,\frac{1}{2}\mathrm{erfc}\left(\frac{r-1}{\delta}\right) + \Lambda, \tag{2.27}$$

which is normalized to be unity at the jet inlet, and Λ in the ambient gas.

In the Burke-Schumann swirling flames (chapter 4), δ is again used to define the

mixture-fraction inflow ($\partial\Omega_i$) profile

$$Z = \frac{1}{2}\mathrm{erfc}\left(\frac{r-1}{\delta}\right), \tag{2.28}$$

which is unity in the fuel-jet and zero in the small ambient coflow of air.

2.3.3 Inlet: concentric swirling jets

At the central jet inlet $\partial\Omega_c$, a fully-developed Poiseuille profile was prescribed for the axial velocity, and the accompanying radial and azimuthal velocity components were set to zero. Thus, at $x = x_{\min}$ for $0 \le r \le R_c'/R_j'$,

$$v_x = 2\frac{U_c'}{U_j'}\left(1 - \frac{r^2}{R_c'^2/R_j'^2}\right) \tag{2.29}$$

$$v_r = 0 \tag{2.30}$$

$$v_\theta = 0. \tag{2.31}$$

At the primary annular jet inlet $\partial\Omega_j$, the axial velocity corresponds to fully-developed annular flow, and the swirling motion is imposed by rotating the air pipe with an angular velocity Ω', so that at $x = x_{\min}$ for $R_{c,o} \le r \le 1$,

$$v_x = \frac{2(1-R_{c,o}^2)\left[R_{c,o}^2 - r^2 + (1-R_{c,o}^2)\frac{\ln(r/R_{c,o})}{\ln(1/R_{c,o})}\right]}{1 - R_{c,o}^4 - \frac{(1-R_{c,o}^2)^2}{\ln(1/R_{c,o})}} \tag{2.32}$$

$$v_r = 0 \tag{2.33}$$

$$v_\theta = \frac{S}{1-R_{c,o}^2}\left[r - \frac{R_{c,o}^2}{r}\right], \tag{2.34}$$

where $R_{c,o} = (R_c' + e')/R_j'$ is the dimensionless outer radius of the central pipe, and the swirl number S is identical to that given in (2.22).

The injector walls $\partial\Omega_w$ use a no-slip condition, and the location of the inlet boundary was set at $x_{\min} = -10$, sufficiently upstream for the fully-developed profiles to remain

unperturbed in configurations undergoing vortex breakdown. To avoid imparting swirl on the surrounding ambient air, the outer wall of the annular jet, located at $r = (R_j' + e')/R_j'$, is stationary ($\boldsymbol{v} = 0$), a procedure also used in previous single jet computations (Douglas and Lesshafft, 2022) and concentric jet experiments (Tummers et al., 2009).

While this setup is simple to implement numerically, the rotating wall introduces a steep velocity gradient $\partial v_\theta/\partial r$ just off the injector, that must be handled carefully so as to not trigger artificial instabilities. This method differs from traditional experimental techniques such as swirler vanes (Degenève et al., 2019a) and tangential entry inlets (Santhosh and Basu, 2016) where all walls are stationary, but it provides consistency between experiments and computations, and has also been used by Tummers et al. (2009).

To reduce parametric dependencies, the fuel-to-air jet-radius ratio R_c'/R_j' is fixed to 0.3 and the bulk velocity ratio U_c'/U_j' is fixed to 0.5, giving a global equivalence ratio $\phi_0 = (\dot{m}_F/\dot{m}_A)/(\dot{m}_F/\dot{m}_A)_s = 0.86$, a value that is close to stoichiometric proportions ($\phi_0 = 1$). These ratios are both consistent with previous experimental investigations of turbulent non-premixed swirling flames (Tangirala et al., 1987; Tangirala and Driscoll, 1988; Chen and Driscoll, 1989; Santhosh and Basu, 2016).

For the flames studied in chapter 5, the mixture fraction is unity in the central fuel jet ($\partial\Omega_c$) and zero in the surrounding air jet ($\partial\Omega_j$), with both streams set to the ambient temperature $T = 1$. A non-penetrating Neumann condition $\boldsymbol{n} \cdot \boldsymbol{\nabla} Z = 0$ is used along the injector walls $\partial\Omega_w$, with $\boldsymbol{n}$ representing the unit normal vector. As discussed in § 2.2, the walls for the Burke-Schumann solution are assumed adiabatic. For the finite-rate chemistry problem, the temperature boundary condition there can play a significant role in the solution of burner attached flames. If an adiabatic condition is used, the reaction may proceed along the outer fuel-jet wall where the axial velocity is zero. On the other hand, for an isothermal wall, attached flames produce high temperature gradients along the injector, which feed into the thermal divergence (2.37), thereby affecting the velocity there. For $S = 1$ and $D_N = 0.95$ in chapter 5, which produce the smallest axial flame position $x_f = 0.08$, both

solutions were found to be identical, confirming that the boundary condition plays no role in the solutions for the set of parameters under investigation. Thus, for simplicity, isothermal walls ($T = 1$) will be adopted for finite-rate chemistry problems, unless otherwise specified.

2.3.4 Open boundaries

Stress-free adiabatic conditions $-p\boldsymbol{n} + \boldsymbol{n} \cdot \left[\mu(\boldsymbol{\nabla}\mathbf{v} + \boldsymbol{\nabla}\mathbf{v}^T)/Re\right] = 0$, $\boldsymbol{n} \cdot \boldsymbol{\nabla} T = 0$ and $\boldsymbol{n} \cdot \boldsymbol{\nabla} Z = 0$ were applied on the lateral $\partial\Omega_l$ boundary of both configurations. The same conditions were applied to the upstream boundary $\partial\Omega_u$ in the concentric jet configuration. At the outflow plane of both configurations, $\partial\Omega_o$, the velocity components, temperature and mixture fraction all satisfied the convective condition

$$\frac{\partial \psi}{\partial t} + C\boldsymbol{n} \cdot \boldsymbol{\nabla}\psi = 0, \tag{2.35}$$

where ψ is an arbitrary scalar. For simplicity, the constant convective speed C was taken to be unity, and the outflow boundary was positioned sufficiently far downstream to prevent spurious effects on the flow. Although this boundary condition requires storage of previous fields to evaluate the temporal derivative, tests with a modified stress-free condition (Dong et al., 2014) showed negligible changes in computational cost. This non-reflective boundary condition has previously been applied to both single (Ruith et al., 2004; Moise and Mathew, 2019; Moise, 2020; Moise and Mathew, 2021) and concentric (Salvetti et al., 1996; Kadu et al., 2019) jet configurations. A more detailed review of the theory and application can be found in a study by Boström (2015).

2.4 Initial conditions

For the single-jet problems (chapters 3 and 4), following Moise and Mathew (2019), the transient numerical integrations were initialized at $t = 0$ using as an initial condition at all x the velocity, temperature and mixture-fraction radial distributions given by the

inlet boundary profiles (2.23)-(2.25), (2.27) and (2.28). For the $Re = 200$ axisymmetric isothermal jet, in addition to these columnar initial conditions, numerical simulations were conducted with a stagnant-flow initial condition, the jet discharging into a quiescent domain ($\boldsymbol{v} = 0$ at $t = 0$). The results reproduced the same critical swirl numbers, thereby indicating that the initial conditions play a negligible role in determining the critical swirl numbers reported in this study. Initial conditions for the concentric jet configuration will be described in chapter 5.

2.5 Numerical solution

Solutions to the unsteady low-Mach-number governing equations (2.8)-(2.11) are carried out with the high-order spectral element code Nek5000 (Fischer et al., 2008). A brief outline of the numerical procedure will be summarized below. More details can be found in reviews by Deville et al. (2002) and Fischer et al. (2017).

2.5.1 Velocity divergence

In a low-Mach-number flow, the thermal equations (energy and mixture fraction) are coupled to continuity and the momentum equations through the density, viscosity and velocity divergence, and the latter is typically enforced as a constraint on the velocity during the temporal integration. From continuity (2.8) and the equation of state (2.13), the velocity divergence can be expressed as

$$\boldsymbol{\nabla} \cdot \boldsymbol{v} = -\frac{1}{\rho}\frac{D\rho}{Dt} = \frac{1}{T}\frac{DT}{Dt}. \tag{2.36}$$

For the finite-rate chemistry and variable-density problems, it follows from (2.10) and (2.36) that

$$\boldsymbol{\nabla} \cdot \boldsymbol{v} = \frac{1}{Re\,Pr}\nabla \cdot (k\boldsymbol{\nabla} T) + qD_N\omega, \tag{2.37}$$

so that the velocity divergence can be computed from the diffusive and chemical source terms, rather than requiring the temporal derivative given in (2.36). In the Burke-Schumann problem, the relationship given in equation (2.37) no longer holds because of the infinite reaction rate ($D_N \to \infty$), so the velocity divergence must be calculated using the material derivative of the temperature from equation (2.36). Since the convective boundary condition given in equation (2.35) requires storage of previous velocity and mixture fraction fields, this does not significantly increase the computational cost of the simulations.

2.5.2 Spatial discretization

The spectral element method (SEM), originally developed by Patera (1984), is a weighted residual technique that derives its high-order from the use of Lagrangian basis functions. Similar to the finite-element method (FEM), the conservation equations (2.8)-(2.11) are solved in their weak form, where one must find $\boldsymbol{v}, T, Z \in X_b^N$ and $p \in Y^N$ such that:

$$(h, \boldsymbol{\nabla} \cdot v) = \left(h, \frac{1}{T}\frac{DT}{Dt}\right) \tag{2.38}$$

$$\left(\boldsymbol{w}, \frac{1}{T}\frac{D\boldsymbol{v}}{Dt}\right) = (\boldsymbol{\nabla} \cdot \boldsymbol{w}, p) + \frac{1}{Re}(\boldsymbol{\nabla}\boldsymbol{w}, \boldsymbol{\tau}) \tag{2.39}$$

$$\left(h, \frac{1}{T}\frac{\partial T}{\partial t}\right) = -\left(h, \frac{1}{T}\boldsymbol{v} \cdot \boldsymbol{\nabla} T\right) + \frac{1}{RePr}(\boldsymbol{\nabla} h, T^{\sigma}\boldsymbol{\nabla} T) + qD_N(h, \omega) \tag{2.40}$$

$$\left(h, \frac{1}{T}\frac{\partial Z}{\partial t}\right) = -\left(h, \frac{1}{T}\boldsymbol{v} \cdot \boldsymbol{\nabla} Z\right) + \frac{1}{RePr}(\boldsymbol{\nabla} h, T^{\sigma}\boldsymbol{\nabla} Z). \tag{2.41}$$

for all test functions $\boldsymbol{w} \in X_0^N$ and $h \in Y^N$ in the computational domain Ω. These equations must also be supplemented by appropriate boundary conditions. The density, viscosity and thermal conductivity have been removed via equations (2.13) and (2.14), and the divergence theorem has been applied to the viscous term in (2.9). The collocated $\mathbb{P}_N - \mathbb{P}_N$ formulation is used so that the velocity and pressure are of the same order, and $Y^N = X^N$ is the set of continuous N^{th}-order spectral element basis functions. Here, X_b^N is the subset of

X^N satisfying Dirichlet conditions on the boundary $\partial\Omega$, X_0^N is the subset of X^N satisfying homogeneous Dirichlet conditions on $\partial\Omega$, and the standard inner product is defined as

$$(h, p) = \int_\Omega hpd\boldsymbol{x} \tag{2.42}$$

$$(\boldsymbol{w}, \boldsymbol{v}) = \int_\Omega \boldsymbol{w} \cdot \boldsymbol{v}d\boldsymbol{x}. \tag{2.43}$$

The computational domain Ω with dimension $d = 2$ or 3 is discretized with E non-overlapping quadrilateral or hexahedral elements. Solutions are represented in terms of Nth-order tensor-product polynomials using Lagrangian basis functions located on Gauss-Lobatto-Legendre (GLL) quadrature points, for a total of $(N + 1)^d$ grid points. In all of the simulations, $N = 7$ is used, and grid refinement is performed by increasing the number of spectral elements E. Grid resolution for specific simulations will be given in the corresponding chapters.

2.5.3 Time discretization

Temporal integration of the spatially-discretized conservation equations (2.38)-(2.41) employs a high-order splitting method (Tomboulides et al., 1997) which decouples the thermal and hydrodynamic equations, as is summarized below. The energy and mixture fraction equations (2.40) and (2.41) are first advanced in time by treating diffusive and chemical source terms implicitly, and non-linear convective terms explicitly. The time derivatives use kth order backward difference formulas (BDFk) and the convective terms are treated with kth order extrapolation (EXTk), with $k = 2$ selected. The updated values of temperature and mixture fraction are used to determine the density, viscosity, thermal conductivity and reaction rate at the next time level through equations (2.13), (2.14), and (2.15). The thermal divergence, determined from either (2.36) or (2.37) depending on problem type, can also be updated.

The momentum equation (2.39) is advanced through a fractional step (splitting)

method first introduced by Orszag et al. (1986). The non-linear convective terms are first used to obtain a predicted velocity field, and a variable coefficient Poisson equation is solved for the hydrodynamic pressure. Finally, the velocity is corrected by solving a Helmholtz equation with the implicit viscous terms and the known pressure.

As an alternative to the BDFk scheme, the material derivative in (2.39) can be solved using the operator-integration-factor splitting scheme (OIFS) developed by Maday et al. (1990). This approach treats linear terms implicitly and the non-linear terms are solved with a characteristics-based explicit scheme, allowing for larger time steps than the traditional BDFk method outlined above. More details on this approach can be found in previous works (Deville et al., 2002; Patel et al., 2019). The BDFk method will be used for all simulations unless otherwise noted.

2.5.4 Axisymmetric solution with swirl and variable-viscosity

By default Nek5000 is capable of solving any number of convection-diffusion scalars of the form given in (2.10). If μ is constant, viscous contributions to the momentum equation reduce to $\boldsymbol{\nabla} \cdot \boldsymbol{\tau} = \boldsymbol{\nabla}^2 \boldsymbol{v} + \boldsymbol{\nabla}(\boldsymbol{\nabla} \cdot \boldsymbol{v})/3$, and for axisymmetric ($\partial/\partial\theta = 0$) flow, the azimuthal velocity can be obtained with the standard convection-diffusion solver. The solution is then fed into the radial momentum equation through the centrifugal force $-\rho v_\theta^2/r$. In the case of variable-viscosity axisymmetric flow, the full stress tensor is required, and the standard convection-diffusion equation for the azimuthal velocity is missing the diffusive term $-(v_\theta/r)(\partial\mu/\partial r)$. In the present work, this term is treated explicitly, which was found to produce stable solutions.

2.5.5 Code scalability

The strong parallelization of the code, also demonstrated by Offermans et al. (2016), is based on the message passing interface (MPI). To validate the scalability of the modified version described in this work, strong and weak scaling tests were conducted for a three-dimensional finite-rate chemistry swirling flame. The results, run on TACC Stampede2

Knights Landing (KNL) nodes, are presented in Figure 2.3. The strong scaling test considers a fixed problem size of $E = 326\,161$ spectral elements, and performance was assessed by increasing the number of cores and measuring the time/time-step. The speedup curve shown in Figure 2.3(a) matches the ideal linear curve for 2048-8192 cores, and only drifts slightly from the ideal case at 16 384 cores. The problem size/core for the weak scaling test was fixed to 19.9 elements/core, corresponding to the 16 384 core case in the strong scaling results. To maintain this fixed problem size/core while varying the number of cores, the quantity of axial elements and the far-field axial boundary were simultaneously decreased so that Δx remained constant. This approach permits the use of the same physical time step needed to meet the Courant-Friedrichs-Lewy (CFL) criteria, and minimizes the effects of the problem size on the parallel efficiency. For the same range of cores considered in the strong scaling test, $(2048, 4096, 8192, 16\,384)$, the domains consist of $E = (40.8, 81.5, 163, 326) \times 10^3$ spectral elements. The results, shown in Figure 2.3(b), indicate parallel efficiencies greater than 77% across the range of cores considered. The change in domain size through the axial boundary can have a small but non-negligible effect on the solution that is reflected in the reported time/time-step. To test this fact, we compare the average number of Generalized Minimal Residual Method (GMRES) iterations required to solve the pressure Poisson equation, the most computationally expensive portion of the integration. For the entire range of cores considered, the average iterations/time-step were identical, giving us confidence in the constant problem size/core.

2.5.6 Code validation

For the variable-density (chapter 3) and Burke-Schumann (chapter 4) single swirling jets, code validation is performed by comparing axisymmetric and three-dimensional solutions at moderate values of S and Re so that the flow reaches a steady state. The curves shown in Figures 2.4 and 2.5 show excellent agreement. These figures also include the steady-state solutions, to be addressed in § 3.5.2.

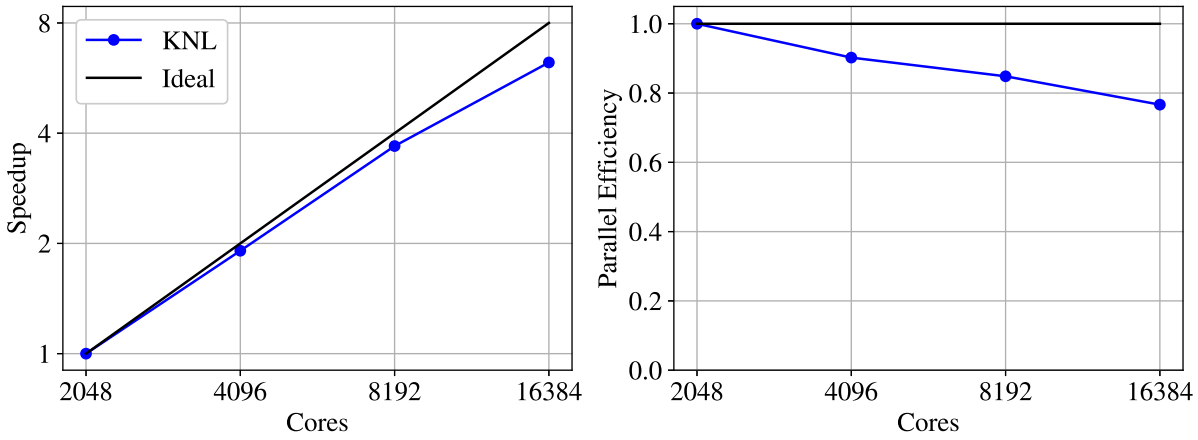

Figure 2.3. Strong (a) and weak (b) scaling tests conducted on Stampede2 Knights Landing nodes.

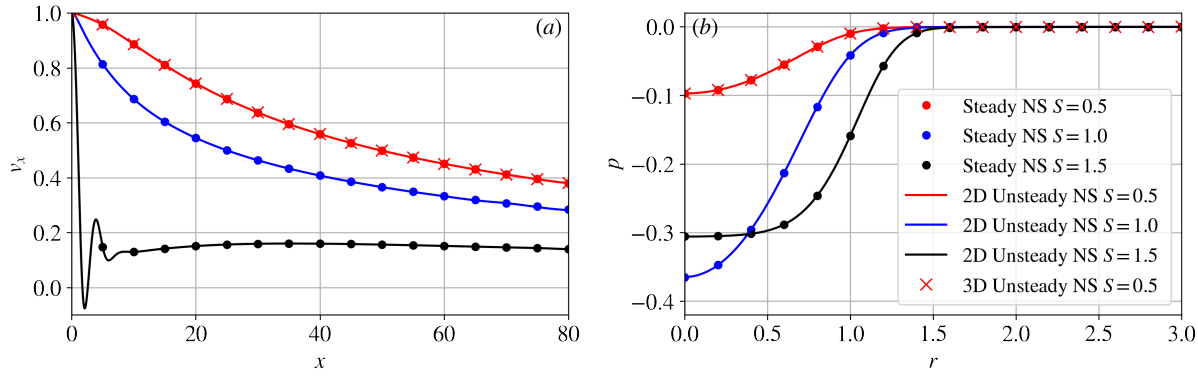

Figure 2.4. Variable-density code validation for $\Lambda = 0.5$ and $Re = 111$: (a) centerline velocity and (b) radial pressure distribution at $x = 2$.

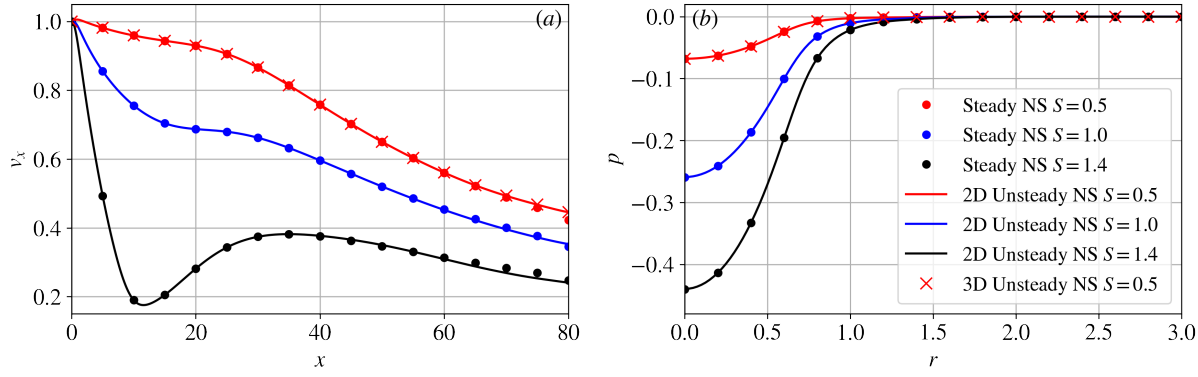

Figure 2.5. Burke-Schumann code validation for $Y_{\mathrm{F},F} = 0.1$ and $Re = 500$: (a) centerline axial velocity and (b) radial pressure distribution at $x = 2$.

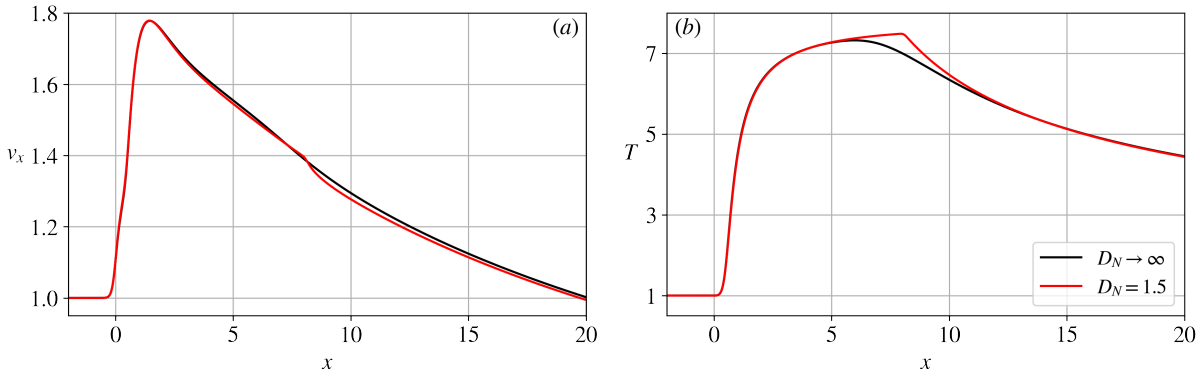

Figure 2.6. Axisymmetric finite-rate code validation for $Y_{\mathrm{F},F} = 1$, $S = 1$ and $Re = 200$: (a) centerline axial velocity and (b) centerline temperature distribution.

To validate the finite-rate chemistry code used in chapter 5, a numerical simulation was conducted for a sufficiently large value D_N, and compared with the corresponding Burke-Schumann solution ($D_N \to \infty$). Since the Burke-Schumann solution uses adiabatic walls, the same condition is applied for the finite-rate problem, unlike the remainder of this work, where isothermal walls are used for finite-rate calculations. See § 2.3.3 for more discussion. The solutions, shown in Figure 2.6, are in excellent agreement, validating the finite-rate chemistry code. In this figure, it should be noted that the peak temperature of the Burke-Schumann solution is in fact slightly lower than the high-D_N solution because of the numerical filter width $\xi^{-1} = 1/80$.

Chapter 3

Variable-density swirling jets

This chapter presents a study of the effects of varying temperature (density) on vortex breakdown in non-reacting swirling jets. Both axisymmetric and three-dimensional simulations describing heated ($\Lambda < 1$) and cooled ($\Lambda > 1$) single jets are performed for different vales of the jet-to-ambient density ratio $\Lambda = \rho'_j/\rho'_a = T'_a/T'_j$ for a fixed effective Reynolds number. Critical swirl numbers for the onset of the bubble (S^*_B) and the cone (S^*_C) are determined. New theoretical predictions for the transition to the bubble assuming steady axisymmetric quasi-cylindrical flow are also presented. The axisymmetric results and analysis are published in the Journal of Fluid Mechanics (Keeton et al., 2022), and serve as an extension to the isothermal case considered by Moise and Mathew (2019). This chapter begins with a description of the simulations and parameters in § 3.1. Results and analysis of the axisymmetric flows are given in § 3.3, followed by results of the three-dimensional flows in § 3.4. Theoretical predictions using the quasi-cylindrical approximation are presented in § 3.5.

3.1 Simulation description

Axisymmetric and three-dimensional simulations are carried out by solving the governing equations (2.8), (2.9), (2.13) and the non-reactive form of (2.10) in terms of the parameters S, Re and Λ. To identify each critical swirl number, the Reynolds number was fixed, and a series of numerical simulations were performed in increments of $\Delta S = 0.01$

for each value of Λ. For the first transition S_B^*, the bubble was distinguished from the pre-breakdown state at S_B^* by the development of a recirculation zone near the jet axis.

The transition to the cone at S_C^* was identified by a sudden increase in the pressure along the jet centerline to the ambient value. As S was increased by 0.01, all transitions at S_C^* exceeded a 75% increase in the pressure at the first stagnation point (see Figures 3.5 and 3.12, to be discussed later). More details on the transition for the axisymmetric case $(Re_{eff}, \Lambda) = (200, 5)$ will be addressed.

To assess the accuracy of the unsteady axisymmetric simulations, the values S_B^* and S_C^* are computed and compared to the three-dimensional values. The results for $\Lambda = 1$ and $Re = 200$ in Table 3.1 show excellent agreement, and are also identical to those obtained by Moise and Mathew (2019) from their three-dimensional isothermal simulations.

3.2 Effective Reynolds number definition

For sufficiently large Reynolds numbers, the axisymmetric flow becomes unstable and transitions from a pre-breakdown state directly to the cone, bypassing the bubble. When direct transition to the cone occurs, S_C^* is the first critical swirl number to appear, and S_B^* is not present. The kinematic viscosity $\nu = \mu/\rho$, normalized as in the formulation, varies with temperature according to $\nu = T^{1+\sigma}$, so that ν, unity in the jet by definition, is less than unity in the ambient gas (to be identified by the subscript a) for $\Lambda < 1$ and greater than unity there for $\Lambda > 1$. For $\Lambda < 1$, the low kinematic viscosity in the ambient region can render the flow unstable, so that the cone is the first to appear, while for $\Lambda > 1$, the ambient viscosity increases and can significantly delay the transition to conical breakdown. To maintain stable flow capable of exhibiting both types of breakdown, an effective viscosity is defined as the geometric mean of the viscosities of the jet and ambient streams, $\nu_{eff} = \sqrt{\nu_a}$, whence, since $\nu_a = \Lambda^{1+\sigma}$, it follows that $\nu_{eff} = \Lambda^{(1+\sigma)/2}$. The effective Reynolds number associated with these variable properties is defined by scaling the jet Reynolds number with the effective

viscosity,

$$Re_{eff} = \frac{Re}{\nu_{eff}}. \tag{3.1}$$

The effective Reynolds number was fixed at the value $Re_{eff} = 200$ for all Λ, and the resulting jet Reynolds number as a function of Λ is $Re = Re_{eff}\Lambda^{(\sigma+1)/2}$. The value of the effective Reynolds number was chosen for consistency with previous numerical studies on isothermal swirling jets (Ruith et al., 2004; Moise and Mathew, 2019; Moise, 2020). In the axisymmetric constant-density study by Fitzgerald et al. (2004), the pre-breakdown state transitioned directly to the cone for $Re_{eff} = Re > 300$. Since the inlet profiles used in that study were close to those of Billant et al. (1998) and the profiles here, values much larger than 200 would not be appropriate for the present work. For $Re_{eff} = 230$, both $\Lambda = 0.2$ and $\Lambda = 0.5$ transitioned from the pre-breakdown state directly to the cone, validating the choice of $Re_{eff} = 200$. Effects of increasing Reynolds number will be explored in § 3.3.5.

3.3 Axisymmetric simulations

3.3.1 Computational grid

A computational grid with $x_{\max} = 80$ and $r_{\max} = 30$ was used to ensure that the radial and axial boundaries were placed sufficiently far away, thereby avoiding contamination of predictions by the boundary conditions applied there. The $(n_x, n_r) = (112, 21)$ spectral elements were stretched to allow finer regions where the velocity and temperature gradients were large, which primarily occur near the jet inlet. All axisymmetric simulations use a fixed time step $\Delta t = 0.01$, determined to satisfy the CFL condition.

3.3.2 Effects of inflow parameters δ and ϵ

To explore the effects of the mixing-layer thickness δ and the coflow strength ϵ on critical swirl numbers, calculations were performed for the isothermal jet at $Re = 200$ with different values of these parameters. For fixed $\epsilon = 0.01$, the critical swirl numbers for $\delta = (0.1, 0.2, 0.3)$ are $S_B^* = (1.36, 1.40, 1.42)$ and $S_C^* = (1.47, 1.57, 1.61)$, indicating that S_B^*

Table 3.1. Summary of unsteady Navier-Stokes results for axisymmetric (2D) and three-dimensional simulations with $Re_{eff} = 200$, $\delta = 0.2$ and $\epsilon = 0.01$. Predicted results using the quasi-cylindrical (QC) approximation are included.

Λ	Re	QC	S_B^* 2D	S_B^* 3D	S_C^* 2D	S_C^* 3D
0.2	51	1.334	1.57	1.57	1.85	1.60
0.5	111	1.326	1.47	1.47	1.60	1.59
1	200	1.317	1.40	1.39	1.57	1.57
2	361	1.312	1.36	1.36	1.52	1.64
5	786	1.323	1.33	1.36	1.75	1.63

and S_C^* increase with increasing values of δ for fixed ϵ. This may be explained by considering the integral swirl number defined in equation (1.1), the values of which, for $\delta = 0.1$ and 0.2 at fixed $S = 1.40$, are $Si = 0.91$ and 0.84, respectively, demonstrating that the effective swirl number decreases with increasing δ in these computations, leading to the increase in S^*. For fixed $\delta = 0.2$, critical swirl numbers for $\epsilon = (0, 0.01, 0.05)$ are $S_B^* = (1.40, 1.40, 1.40)$ and $S_C^* = (1.55, 1.57, 1.68)$. Variation of ϵ from 0 to 0.05 had no effect on S_B^*, but the transition from the bubble to the cone, characterized by S_C^*, is significantly delayed when the coflow velocity is increased by increasing ϵ. For the remainder of the single swirling jet results, including chapter 4, nominal inlet parameter values $\delta = 0.2$ and $\epsilon = 0.01$ are used.

3.3.3 Transition to the bubble S_B^*

Numerical calculations of S_B^* in Table 3.1 display a moderate dependence on Λ, monotonically decreasing with increasing Λ. Steady-state projected streamlines for the first transition are shown in Figure 3.1. The effects of Λ on S_B^* can be better understood by comparing the intermediate cases of $\Lambda = (0.5, 1, 2)$ at fixed $S = 1.5$, for which the steady-state bubble streamlines are shown in Figure 3.2. As the value of Λ is increased, the imbalance of the centrifugal force and radial pressure gradient increases, with the cenrtifugal force becoming more dominant, as shown in Figure 3.3(a), and this gives rise to an expansion of the flow. The resulting axial pressure gradient along the jet axis, shown in Figure 3.3(b),

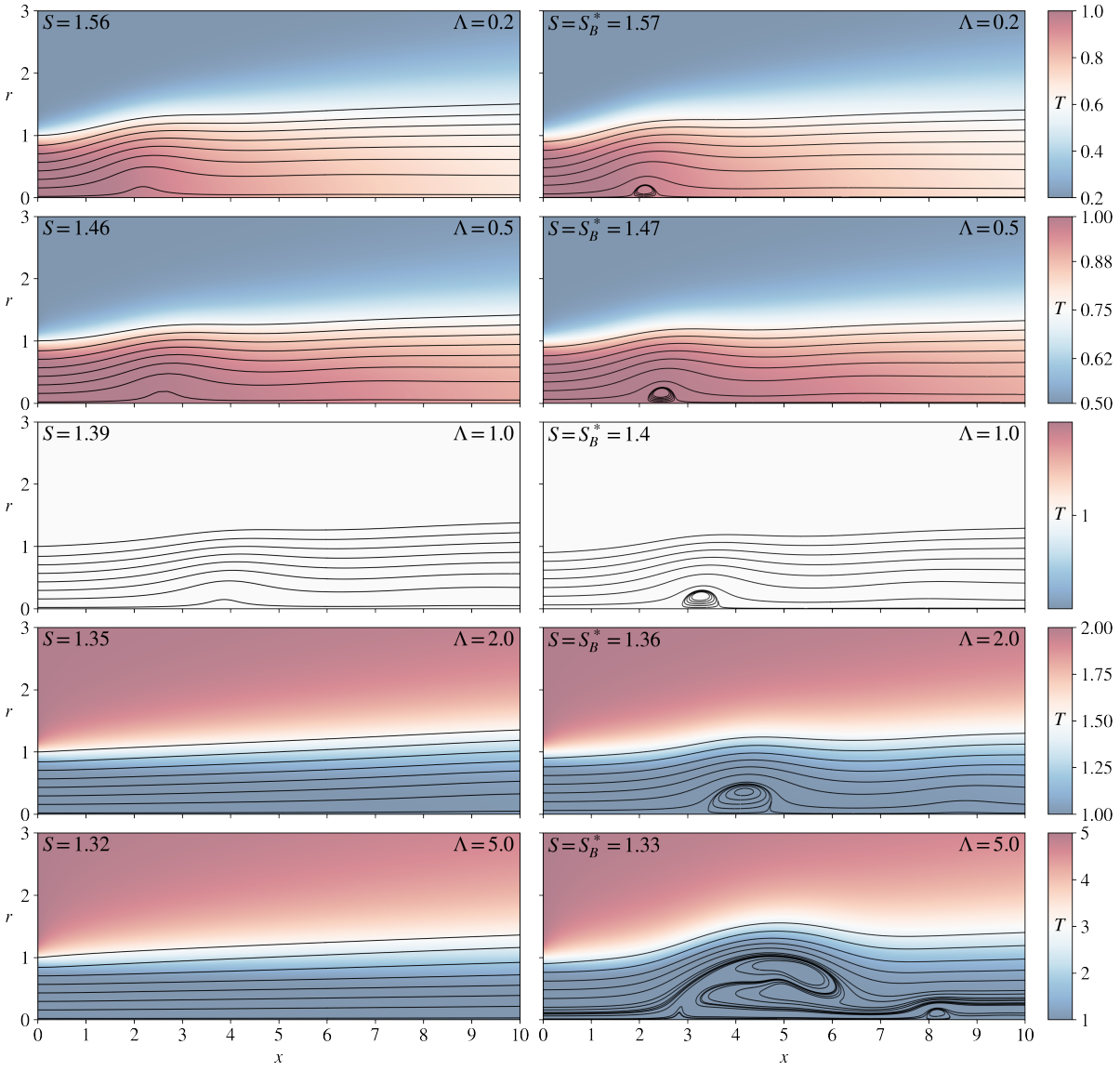

Figure 3.1. Axisymmetric solutions: steady-state projected streamlines colored by temperature showing the transition to the bubble at S_B^* for $Re_{eff} = 200$ and $\Lambda = (0.2, 0.5, 1, 2, 5)$.

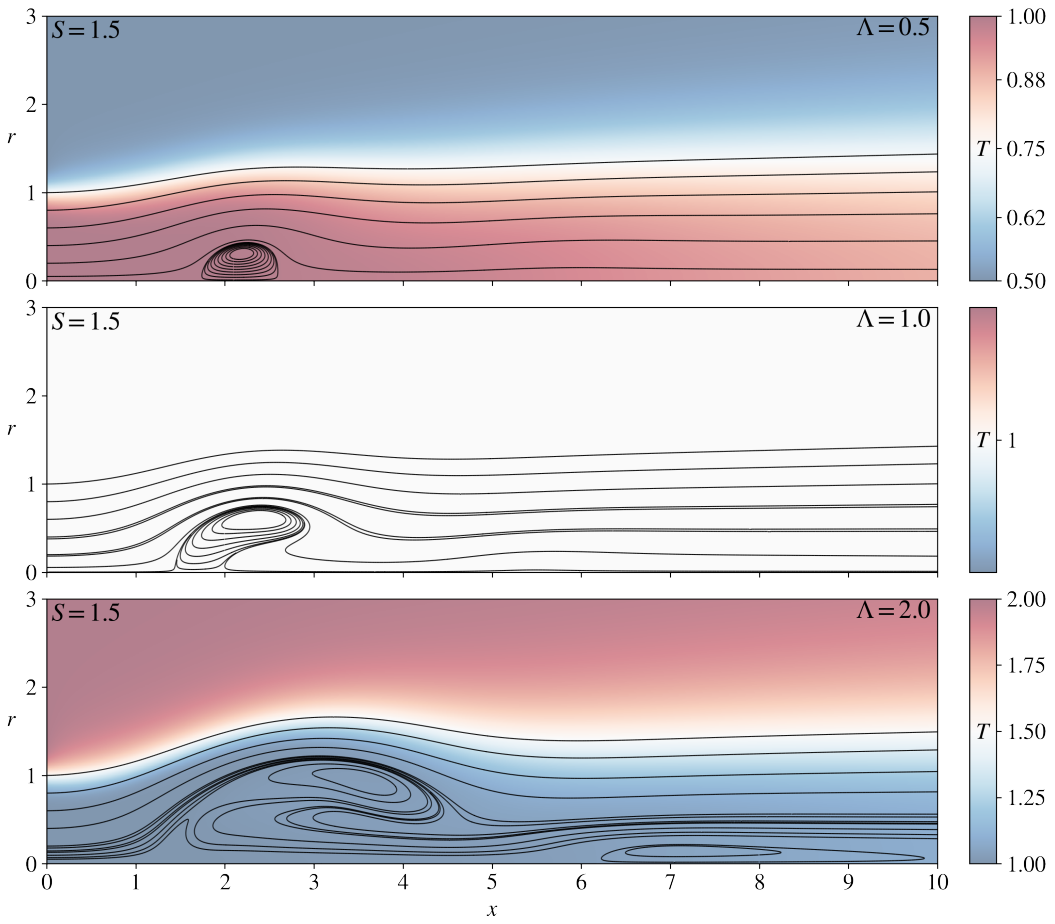

Figure 3.2. Axisymmetric steady-state projected streamlines colored with temperature for $S = 1.5$, $Re_{eff} = 200$ and $\Lambda = (0.5, 1, 2)$.

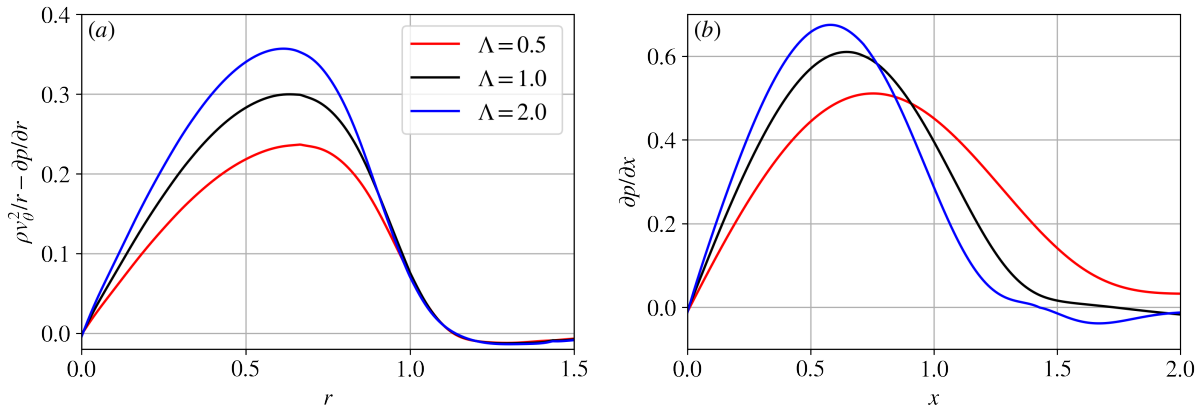

Figure 3.3. Axisymmetric steady-state solutions for $S = 1.5$ and $Re_{eff} = 200$: dependence of (a) $\rho v_\theta^2/r - \partial p/\partial r$ on r at $x = 0.1$ and of (b) $\partial p/\partial x$ on x at $r = 0$.

increases as Λ increases, lowering S_B^*. The increased axial pressure gradient drives the stagnation point upstream until it travels off the axis for $\Lambda = 2$, resulting in a two-celled bubble, with a secondary breakdown at $x = 6$. Although the two-celled bubble has been observed experimentally (Billant et al., 1998; Leibovich, 1978), vortex breakdown has been found to travel upstream into the nozzle exit for large values of S (Billant et al., 1998; Manoharan et al., 2020), allowing the possibility for effects from the prescribed steady inflow profile (Moise and Mathew, 2019). For the low Reynolds numbers considered here, the first solutions of bubble breakdown at S_B^* were steady, justifying the use of the steady theoretical predictions, to be discussed in § 3.5.1 and § 3.5.2.

3.3.4 Transition to the cone S_C^*

As the inlet swirl number increases beyond S_B^*, a critical swirl number S_C^* is encountered, and the bubble transitions to a conical structure with an open recirculation zone. All conical breakdown cases were unsteady, and a temporal average of 50 instantaneous fields spaced $\Delta t = 50$ was sufficient for determining the average behavior. Results are discussed first for $\Lambda = (0.2, 0.5, 1, 2)$, where S_C^* varies in a way similar to that of the numerical values of S_B^*, decreasing with increasing Λ. The time-averaged streamlines, plotted in Figure 3.4, show the abrupt transition from the bubble to the cone. As the recirculation zone increases,

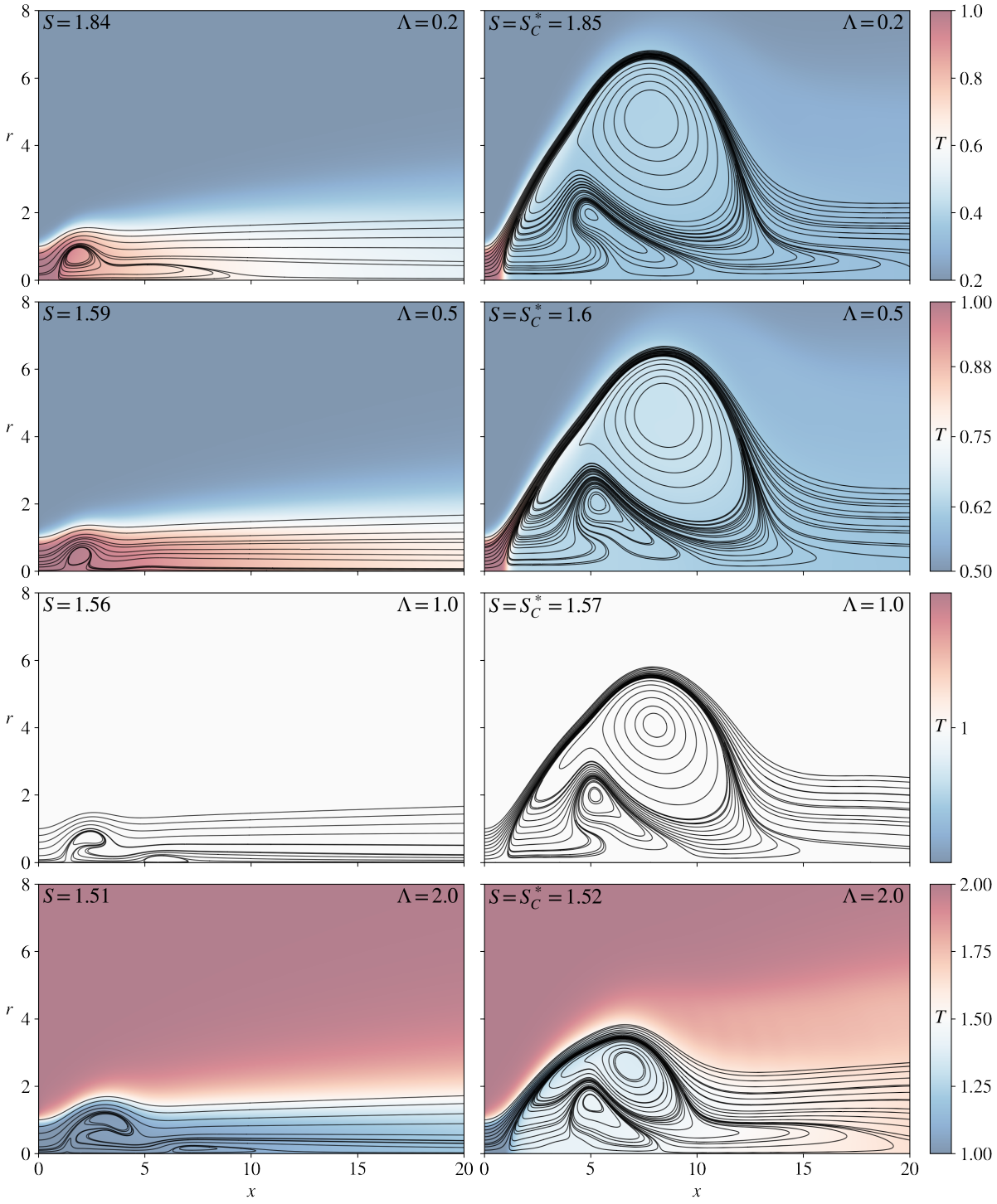

Figure 3.4. Axisymmetric solutions: time-averaged projected streamlines colored by temperature showing the transition to the cone at S_C^* for $Re_{eff} = 200$ and $\Lambda = (0.2, 0.5, 1, 2)$.

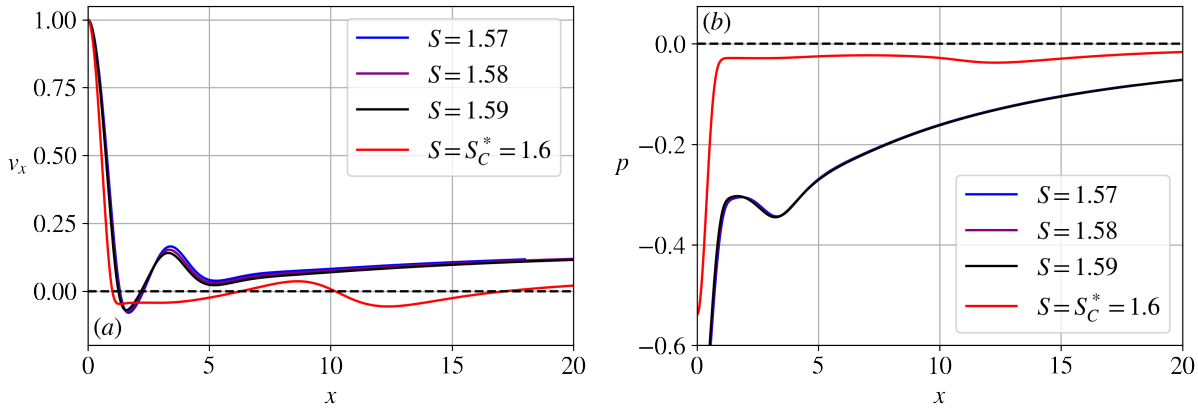

Figure 3.5. Axisymmetric solutions: time-averaged results for (a) centerline axial velocity and (b) centerline pressure before and at the transition to the cone for $\Lambda = 0.5$ and $Re_{eff} = 200$.

velocity magnitudes decrease and the pressure reaches a value near the ambient, which corresponds to $p = 0$ with the normalization, and is shown in Figure 3.5(b) for $\Lambda = 0.5$. The assumption of axisymmetric flow leads to a two-celled recirculation zone when the bubble first transitions to the cone, unlike the three-dimensional results to be discussed later in § 3.4.3.

For the case of $\Lambda = 5$ at $Re_{eff} = 200$, the jet Reynolds number is $Re = 786$, and the non-dimensional viscosity in the ambient gas increases to $\nu_a = 15.4$. For $S \leq 1.45$, the bubble is steady, with a secondary recirculation zone located on the jet axis (top row of Figure 3.6). As S is increased from 1.45 to 1.46, the recirculation zone and wake become unstable, elongating the secondary breakdown region. During this transition, there is a small jump in the pressure along the axis towards $p = 0$ (not shown), a typical sign of a transition to the cone. The increased viscosity in the ambient region, however, prevents the opening of the bubble into the cone. As S is continuously increased up to $S = 1.7$ (bottom row of Figure 3.6), the bubble grows to sizes comparable to that of the cone for other values of Λ (Figure 3.4), but it shows no signs of a sudden opening of the flow. At $S = S_C^* = 1.75$, the conical shear layer becomes unstable, and the bubble transitions to a one-celled cone much larger than the first cone encountered for $\Lambda \leq 2$, as seen in Figure 3.7.

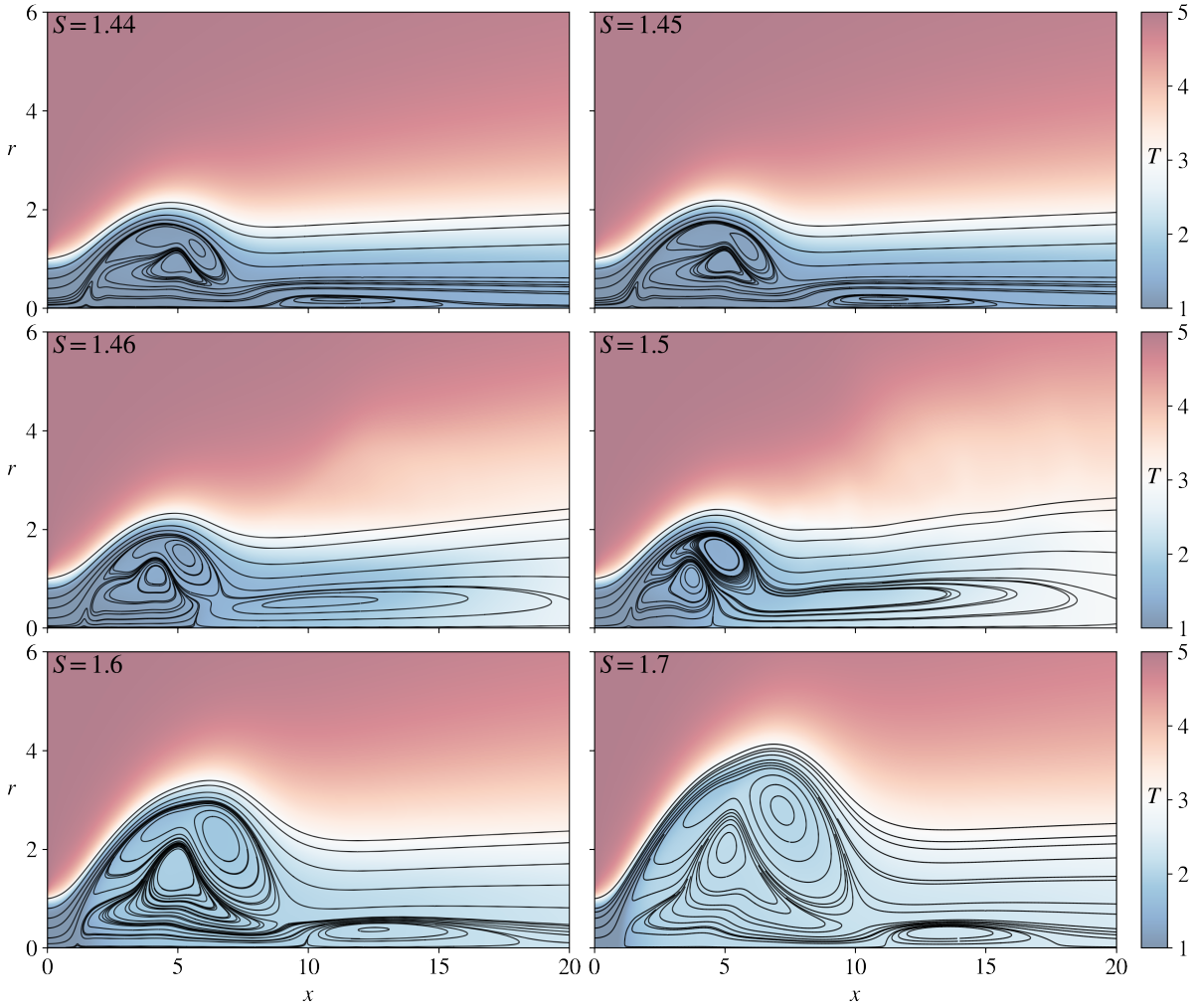

Figure 3.6. Axisymmetric solutions: time-averaged projected streamlines colored by temperature for increasing values of S with $\Lambda = 5$ and $Re_{eff} = 200$.

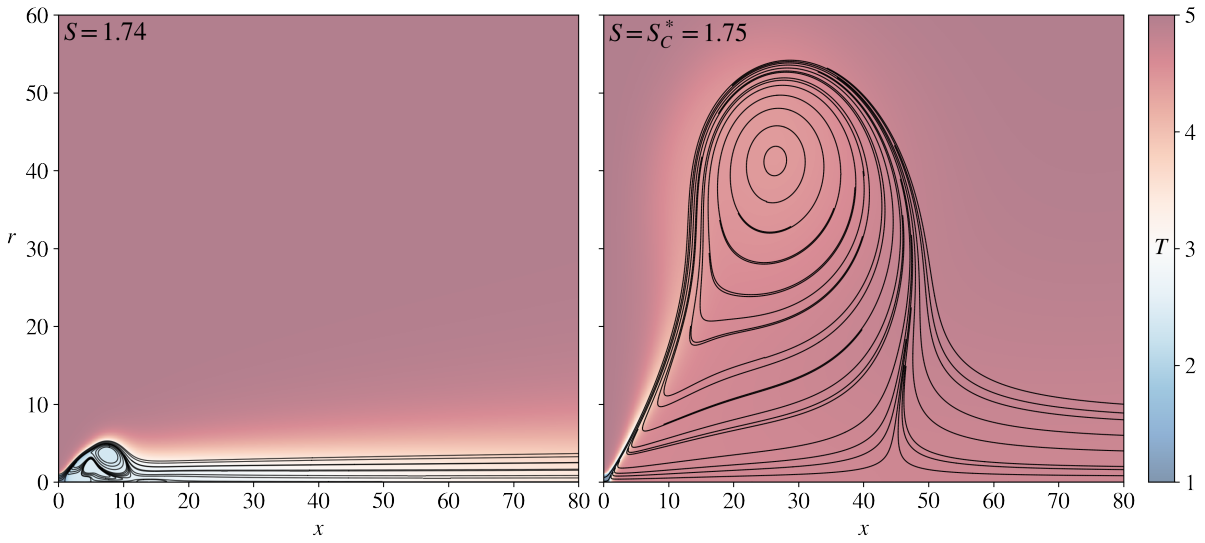

Figure 3.7. Axisymmetric solutions: time-averaged projected streamlines colored by temperature showing the transition to the cone at S_C^* for $Re_{eff} = 200$ and $\Lambda = 5$.

To accommodate the increased size, a new domain was adopted with $(n_x, n_r) = (69, 27)$ spectral elements spanning $x_{\max} = 100$ and $r_{\max} = 100$. For sufficiently large time, the cone spreads and contamination of the boundaries is observed. The increased viscosity of the ambient region thus delays the transition to the cone, destroying the otherwise monotonic trend of decreasing S_C^* with increasing Λ, which may be caused by the increase in jet Reynolds number with increasing Λ.

3.3.5 Effects of the Reynolds number

For hot jets $\Lambda = (0.2, 0.5)$, an increase from $Re_{eff} = 200$ to 230 led to the direct transition from the pre-breakdown state to the cone, at values $S_C^* = 1.52$ and 1.43, respectively. For $\Lambda = (1, 2, 5)$, critical swirl numbers for $Re_{eff} = 230$ were $S_B^* = (1.39, 1.36, 1.33)$ and $S_C^* = (1.48, 1.47, 1.64)$. The values S_B^* for this effective Reynolds number displayed only a small decrease from those for $Re_{eff} = 200$ given in Table 3.1. This result is consistent with previous experimental studies on isothermal breakdown for which S_B^* decreased for increasing Re up to a critical value, above which S_B^* remained constant (Spall et al., 1987). For the transition to the cone, the effect of the Reynolds number is greater, with values

S_C^* decreasing considerably from the $Re_{eff} = 200$ values, owing to the decrease in viscous damping effects.

For $\Lambda = 5$, the increase in effective Reynolds number from 200 to 230 causes the bubble to transition to the compact two-celled cone that is observed for all other values of Λ, rather than to the enlarged one-celled cone observed for $Re_{eff} = 200$. This confirms that the delayed transition from the bubble directly to the enlarged one-celled cone for $\Lambda = 5$ and $Re_{eff} = 200$ is strongly influenced by viscosity. It is thus understandable that, for sufficiently large Reynolds numbers, S_C^* exhibits a weaker dependence on Λ.

3.4 Three-dimensional simulations

3.4.1 Computational grid

The computational grid, shown in Figure 3.8, was constructed on a revolved version of the axisymmetric grid described above, using identical extents and $(n_x, n_r, n_\theta) = (80, 20, 12)$. In the region $0 \leq x \leq 5$ and $0 \leq r \leq 3$, the grid uses a spectral element skeleton that has approximately $\mathrm{d}x = \mathrm{d}r = 0.4$. For $r > 3$, elements were stretched radially while a constant grid spacing $\mathrm{d}x = 0.94$ is used for $x > 5$. The temporal integration used the characteristic based time stepping approach (OIFS), with a fixed time step $\Delta t = 2 \times 10^{-2}$.

3.4.2 Transition to the bubble S_B^*

Since the flow upstream of breakdown remains axisymmetric and steady, the three-dimensional results for S_B^* were nearly identical to those given by the axisymmetric computations (Table 3.1). The bubble recirculation regions for $\Lambda \leq 2$ were all steady, owing to the moderate Reynolds numbers, and three-dimensional effects only occurred downstream. For $\Lambda = 5$, an unsteady two-celled bubble with a spiral tail formed, which has also been identified in isothermal jets (Moise, 2020). The unsteady wake is shown in Figure 3.9 by the second invariant of the velocity gradient, Q. Because of the sufficiently large Reynolds number, the stagnation point is positioned close to the inlet plane, and lifts off the jet axis,

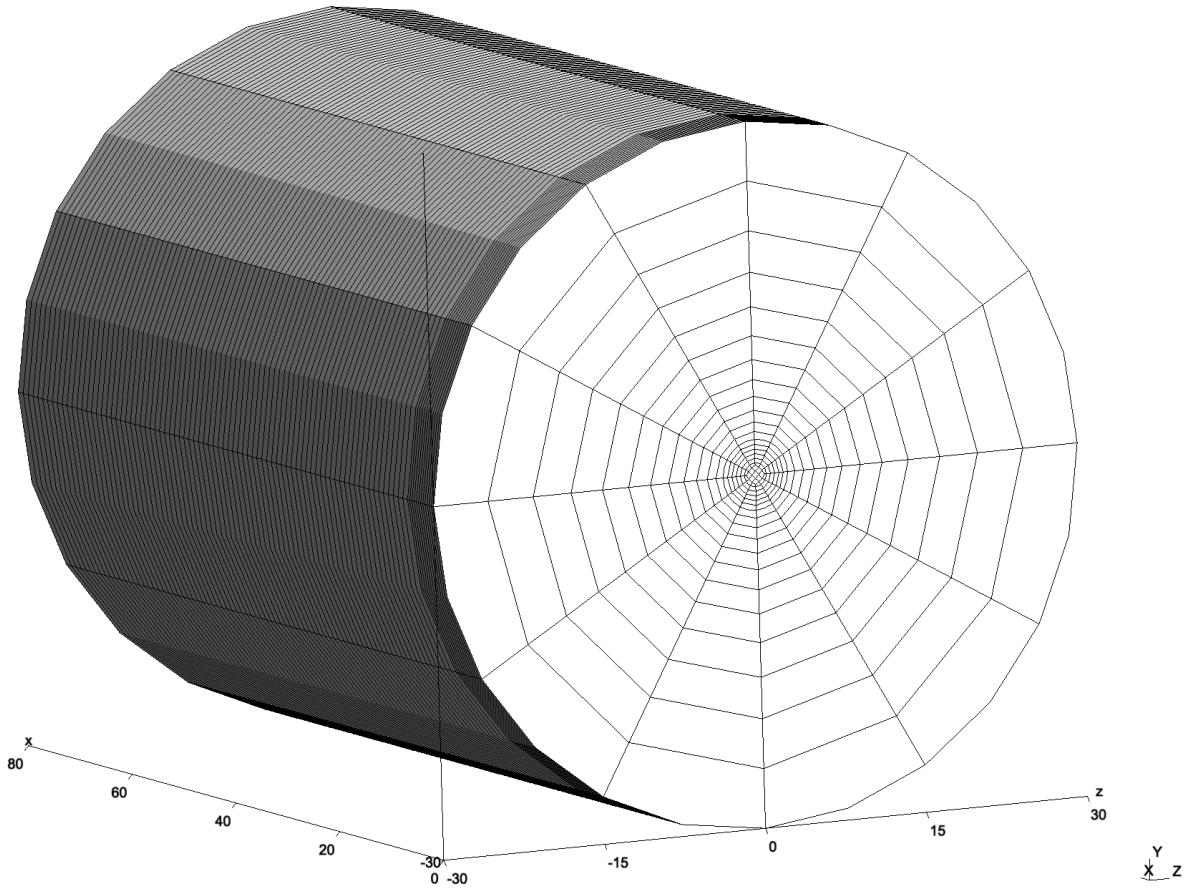

Figure 3.8. Three-dimensional spectral element skeleton for the variable-density computational grid.

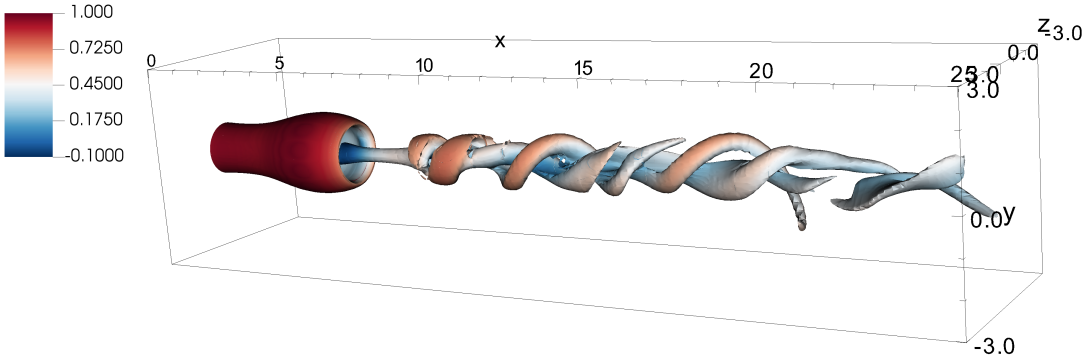

Figure 3.9. Instantaneous iso-surface of $Q = 0.3$ colored by v_x for $\Lambda = 5$, $Re_{eff} = 200$ and $S = S_B^* = 1.36$.

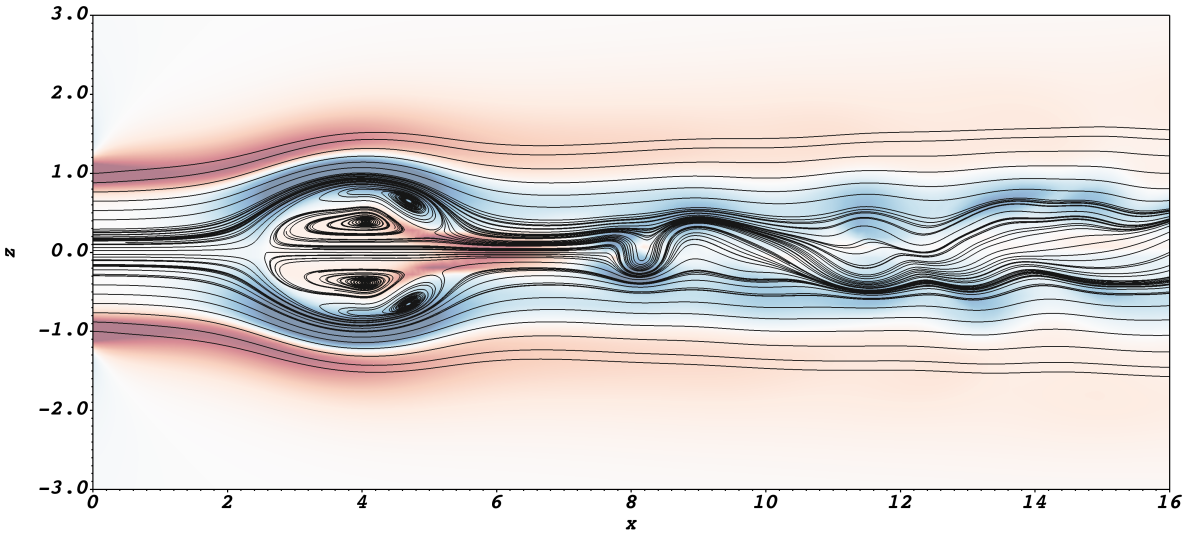

Figure 3.10. Instantaneous projected streamlines colored by azimuthal vorticity in the range $[-2, 2]$ for $\Lambda = 5$, $Re_{eff} = 200$ and $S = S_B^* = 1.36$.

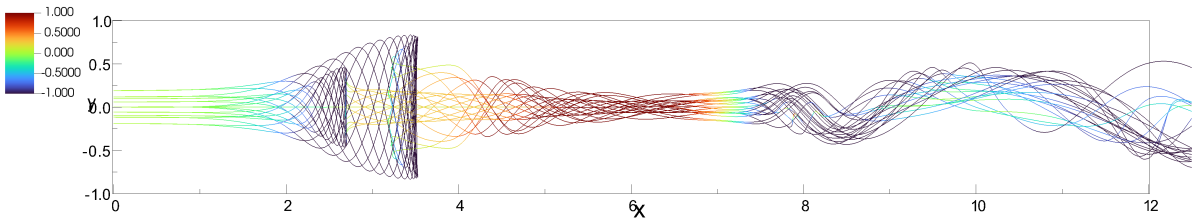

Figure 3.11. Instantaneous vortex lines colored by azimuthal vorticity for $\Lambda = 5$, $Re_{eff} = 200$ and $S = S_B^* = 1.36$. Lines originate from 10 equally spaced points in the azimuthal direction at $(x, r) = (0, 0.1)$ and $(x, r) = (0, 0.2)$.

recycling the swirling flow in the positive axial direction through the second cell of the bubble (Figure 3.10). This in turn produces a high concentration of axial vorticity (Figure 3.11) in the bubble's wake, which leads to the spiral mode that forms downstream.

3.4.3 Transition to the cone S_C^*

As discussed in the experimental work by Rajamanickam and Basu (2018), the transition to the cone involves high vortex shedding modes as the bubble opens radially. It may then be expected that azimuthal asymmetries interact with the axial and centrifugal instabilities, thereby leading to differences in S_C^*. Unlike the axisymmetric simulation results for S_C^*, which primarily decreased with increasing Λ (except for the case $\Lambda = 5$ discussed

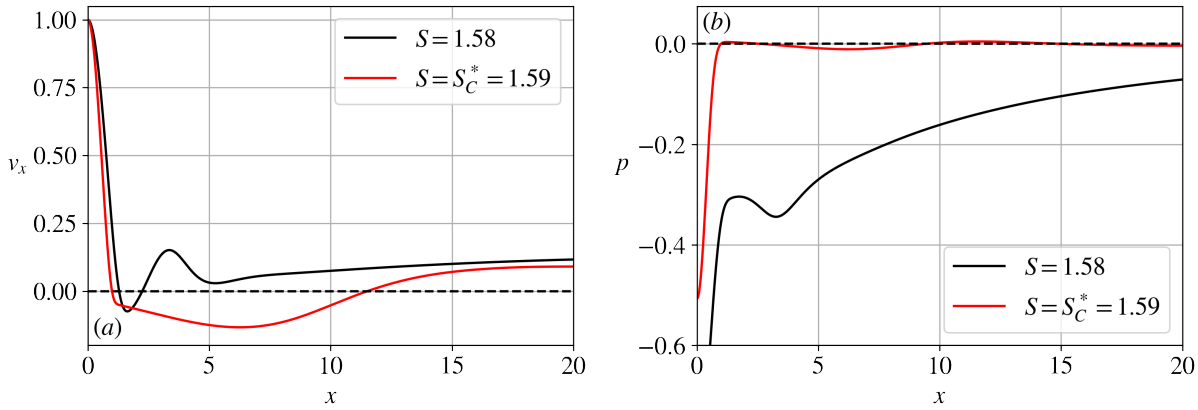

Figure 3.12. Three-dimensional solutions: time-averaged (a) centerline axial velocity and (b) centerline pressure before and at the transition to the cone for $\Lambda = 0.5$ and $Re_{eff} = 200$.

above), the three-dimensional simulation results for S_C^* remain relatively constant with Λ (Table 3.1). Except for $\Lambda = 5$, three dimensional results for S_C^* are found to be smaller than the axisymmetric results for $\Lambda < 1$, larger than the axisymmetric values for $\Lambda > 1$, and equal for $\Lambda = 1$. One possible source for the discrepancy in the values of S_C^* is the transient development from the columnar initial conditions. The asymmetric flow that emerges may influence the final state, which is known to be bi-stable (Moise, 2020).

The typical transition to the cone for $\Lambda = 0.5$ and $Re_{eff} = 200$ is shown in the centerline axial velocity and pressure plots in Figure 3.12, which may be compared to the same transition given by the axisymmetric solutions in Figure 3.5. In the three-dimensional case, the unsteady flow leads to a time-averaged single-celled recirculation zone that is completely open ($p = 0$), confirming the assumption made by Billant et al. (1998). The time-averaged streamlines showing the same transition for all values of Λ are shown in Figure 3.13, where temporal averages were performed with 50 field files with a snapshot interval of $\Delta t = 5$. For increasing values of Λ, the size of the last bubble before the cone increases. After the opening to the cone, the time-averaged structure of the recirculation zone remains relatively similar across the entire range of Λ, in contrast with the axisymmetric results in Figures 3.4 and 3.7.

For $\Lambda = 0.5$ and $S = S_C^* = 1.59$, the unsteady flow, shown in Figure 3.14, remains

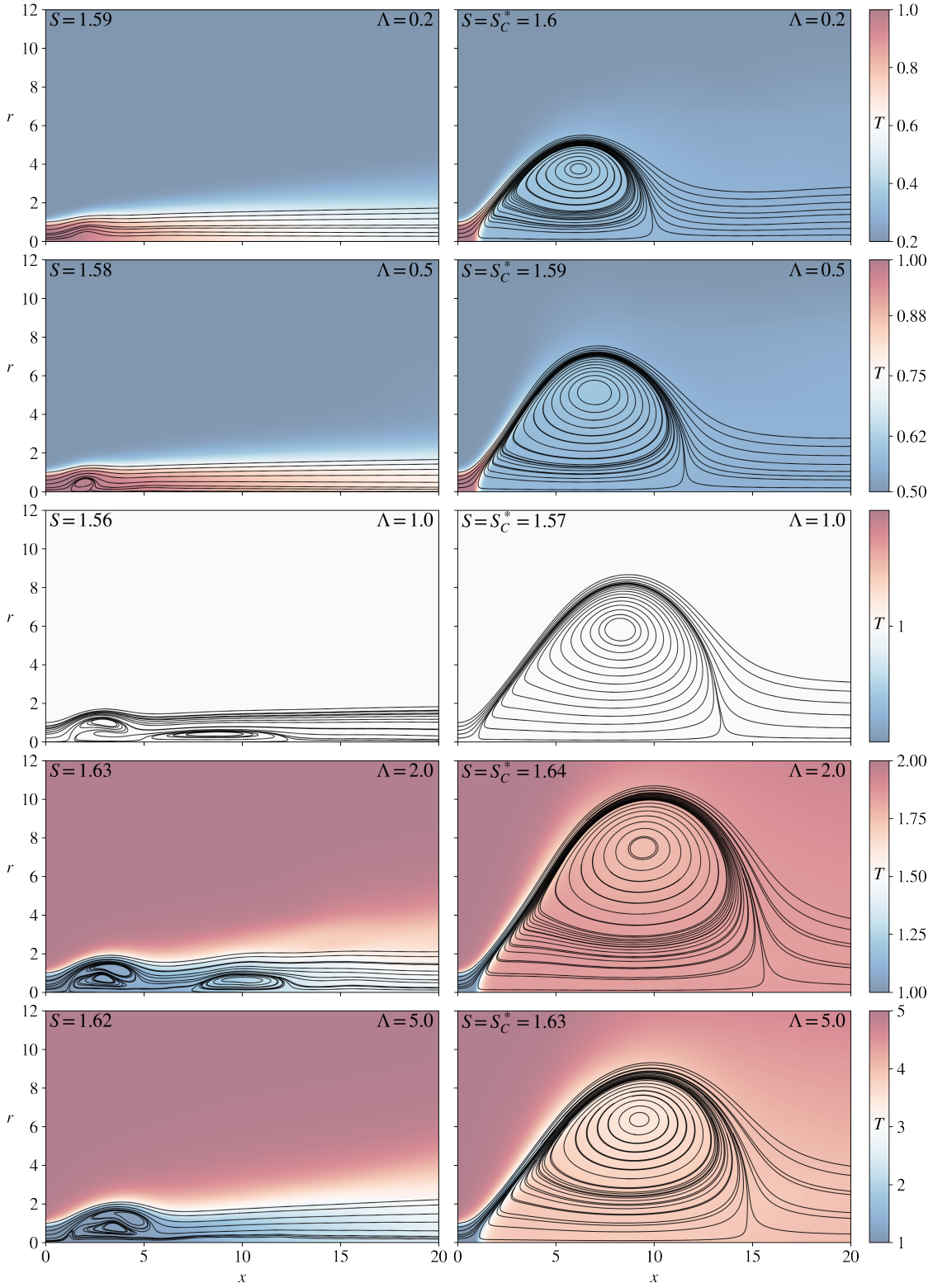

Figure 3.13. Three-dimensional solutions: time-averaged transition to the cone S_C^* for $Re_{eff} = 200$ and different values of Λ.

nearly axisymmetric in the near field ($x = 2$), and the azimuthal shear results in a loss of symmetry on the tails of the conical sheet at $x = 4$ (Figure 3.14(c)). For $\Lambda = 5$ and $S = S_C^* = 1.63$, on the other hand, the increase in viscosity leads to a nearly axisymmetric flow for $x \leq 4$ (Figure 3.15(b, c)), and a similar $|m| = 2$ mode forms at $x \approx 9$ (not shown).

3.5 Theoretical predictions of vortex breakdown

In this section, steady-state axisymmetric theoretical predictions will be made for the onset of bubble breakdown at $S = S_B^*$.

3.5.1 Quasi-cylindrical approximation

Hall (1967) proposed an entirely different approach to the computation of vortex breakdown based on the failure of the quasi-cylindrical (QC) approximation of viscous axisymmetric flow. This method applies specifically to bubble breakdown, when the flow upstream from the stagnation point is steady and varies only gradually in the axial direction. The approach builds on ideas developed in connection with two-dimensional boundary layers, where the separation is predicted based on the failure of the downstream-marching numerical integration of the boundary-layer equations. For swirling flows, it is reasoned that, if in the course of the calculation of a QC vortex core for a given value of S the results develop a singularity at a given location, characterized by rapid increase of axial gradients and radial velocities, there must also be appreciable axial gradients at that location in the associated real vortex core, corresponding to vortex breakdown. In this approximation, the predicted critical swirl number S_B^* (the smallest value of S for which a singularity develops), is independent of Re. Results will be computed below for different values of the jet-to-ambient density ratio Λ, thereby complementing previous results pertaining to constant-density jets (Revuelta et al., 2004) and light compressible jets (Gallardo-Ruiz et al., 2010).

For the moderately large values of Re considered, the jet remains slender for values of S smaller than S_B^*, which is of order unity. The slender flow includes a development region

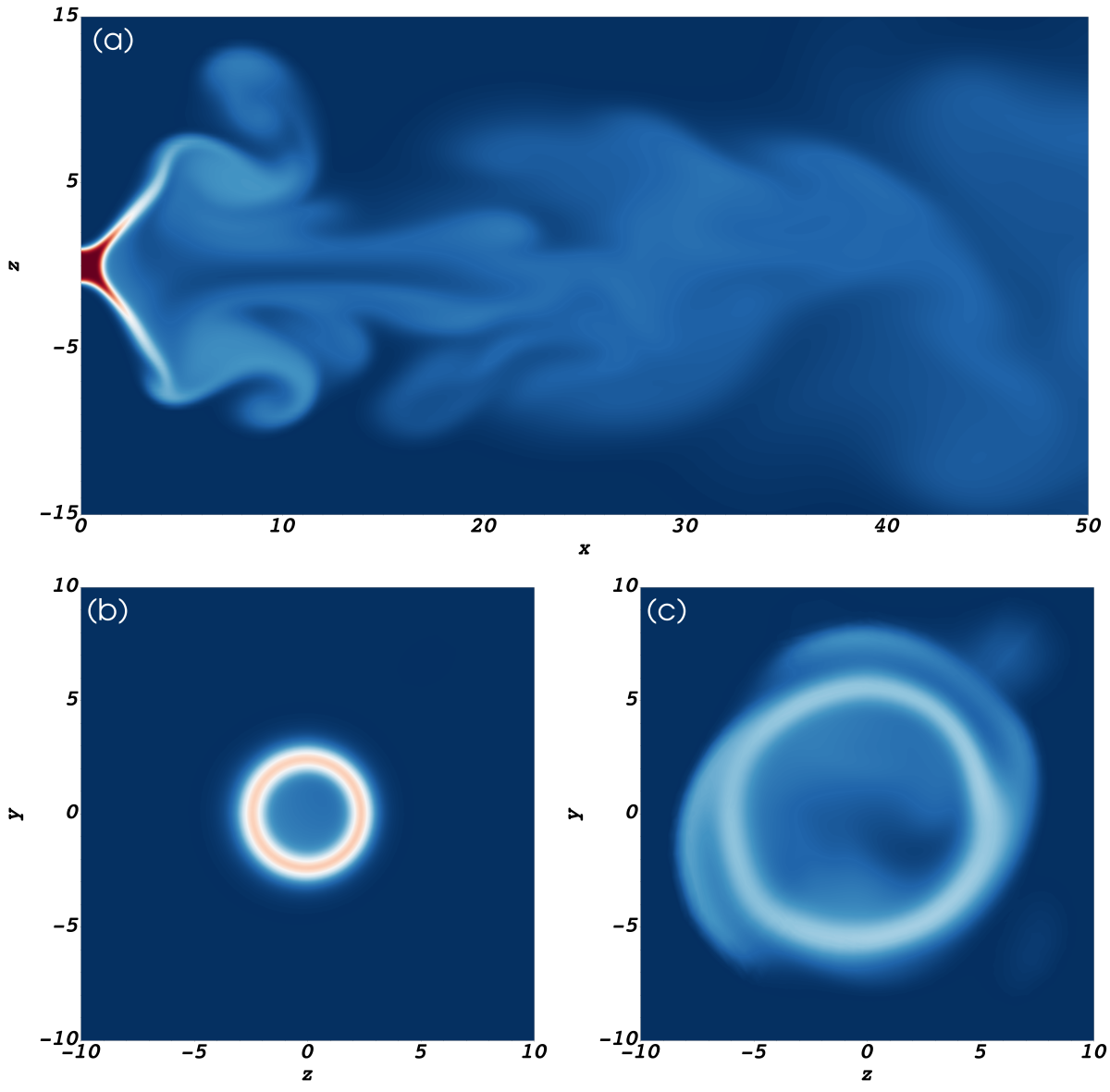

Figure 3.14. Instantaneous color contours of $T \in [\Lambda, 1]$ for $S = S_C^* = 1.59$, $\Lambda = 0.5$ and $Re_{eff} = 200$ at (a) $y = 0$, (b) $x = 2$, and (c) $x = 4$. Note that the swirl is clockwise.

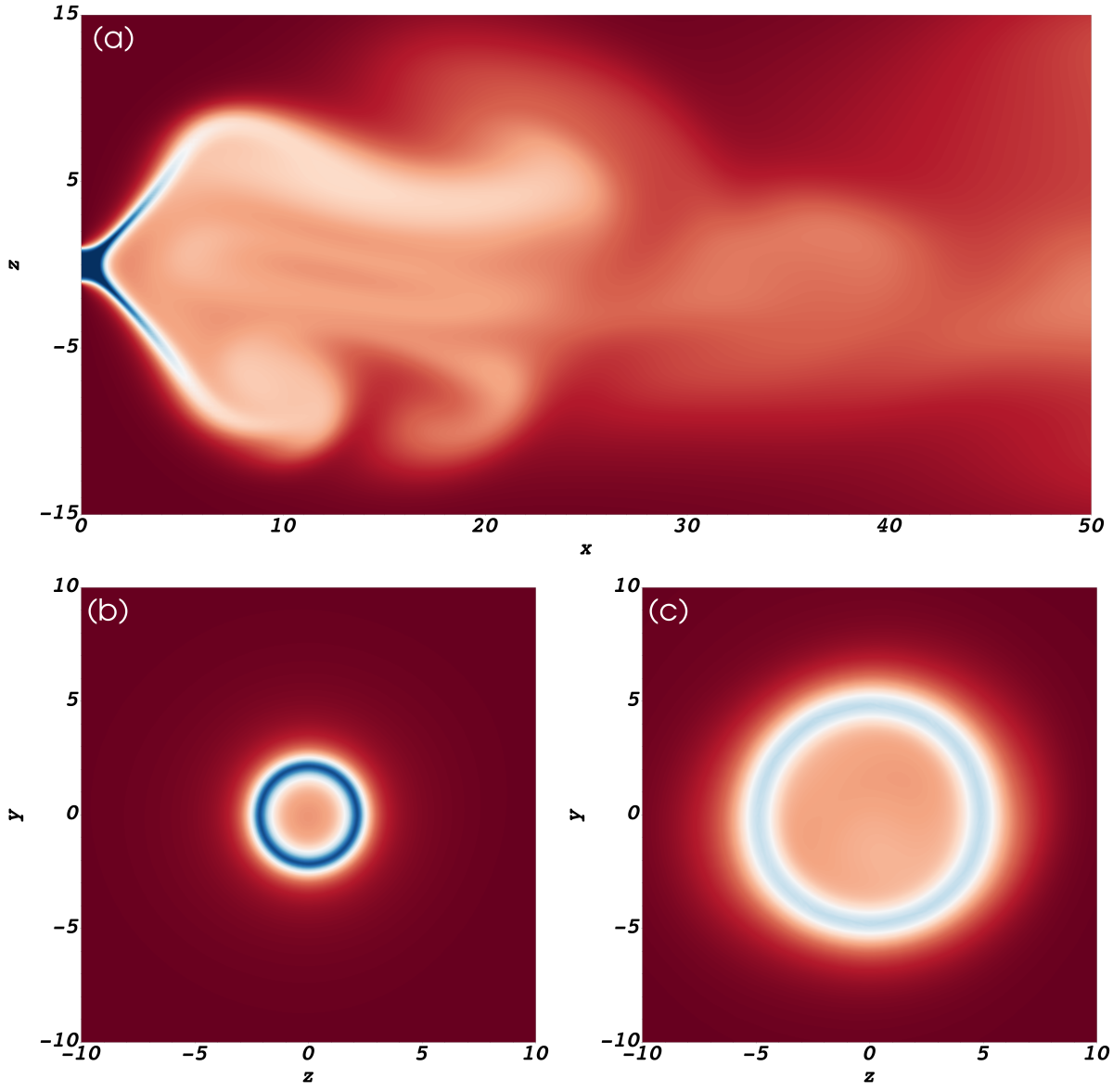

Figure 3.15. Instantaneous color contours of $T \in [1, \Lambda]$ for $S = S_C^* = 1.63$, $\Lambda = 5$ and $Re_{eff} = 200$ at (a) $y = 0$, (b) $x = 2$, and (c) $x = 4$. Note that the swirl is clockwise.

$x \sim Re$ where the axial velocity v_x is of order unity and the radial velocity v_r is of order $Re^{-1} \ll 1$. If the Reynolds number is also sufficiently low for the flow to remain stable, then the velocity in the far field approaches the well-known Schlichting solution (Von Schlichting, 1933), with accompanying weak swirling motion given by the Görtler-Loitsianskii solution (Görtler, 1954; Loitsianskii, 1953).

To facilitate the presentation, it is useful to describe the azimuthal motion in terms of the dimensionless circulation per unit azimuthal angle $\Gamma = rv_\theta/S$ and use the characteristic scales of the slender jet-development region to define a rescaled axial distance $\hat{x} = x/Re$ and a rescaled radial velocity $\hat{v}_r = Re\, v_r$. In terms of these new variables, the steady axisymmetric form of the conservation equations (2.8)–(2.10) is

$$\frac{\partial}{\partial \hat{x}}(\rho v_x) + \frac{1}{r}\frac{\partial}{\partial r}(\rho r \hat{v}_r) = 0, \tag{3.2}$$

$$\begin{aligned} \rho\left(v_x\frac{\partial v_x}{\partial \hat{x}} + \hat{v}_r\frac{\partial v_x}{\partial r}\right) &= -\frac{\partial p}{\partial \hat{x}} + \frac{1}{r}\frac{\partial}{\partial r}\left(\mu r\frac{\partial v_x}{\partial r}\right) \\ &+ \frac{1}{Re^2}\left[\frac{\partial}{\partial \hat{x}}\left(2\mu\frac{\partial v_x}{\partial \hat{x}}\right) + \frac{1}{r}\frac{\partial}{\partial r}\left(\mu r\frac{\partial \hat{v}_r}{\partial r}\right)\right] \end{aligned} \tag{3.3}$$

$$\begin{aligned} \rho\left(v_x\frac{\partial \hat{v}_r}{\partial \hat{x}} + \hat{v}_r\frac{\partial \hat{v}_r}{\partial r}\right) &= Re^2\left(S^2\rho\frac{\Gamma^2}{r^3} - \frac{\partial p}{\partial r}\right) + \frac{1}{r}\frac{\partial}{\partial r}\left(2\mu r\frac{\partial \hat{v}_r}{\partial r}\right) \\ &- 2\mu\frac{\hat{v}_r}{r^2} + \frac{\partial}{\partial \hat{x}}\left(\mu\frac{\partial v_x}{\partial r}\right) + \frac{1}{Re^2}\frac{\partial}{\partial \hat{x}}\left(\mu\frac{\partial \hat{v}_r}{\partial \hat{x}}\right) \end{aligned} \tag{3.4}$$

$$\rho\left(v_x\frac{\partial \Gamma}{\partial \hat{x}} + \hat{v}_r\frac{\partial \Gamma}{\partial r}\right) = \frac{1}{r}\frac{\partial}{\partial r}\left(\mu r\frac{\partial \Gamma}{\partial r} - 2\mu\Gamma\right) + \frac{1}{Re^2}\frac{\partial}{\partial \hat{x}}\left(\mu\frac{\partial \Gamma}{\partial \hat{x}}\right) \tag{3.5}$$

$$\rho\left(v_x\frac{\partial T}{\partial \hat{x}} + \hat{v}_r\frac{\partial T}{\partial r}\right) = \frac{1}{r}\frac{\partial}{\partial r}\left(\frac{k}{Pr}r\frac{\partial T}{\partial r}\right) + \frac{1}{Re^2}\frac{\partial}{\partial \hat{x}}\left(\frac{k}{Pr}\frac{\partial T}{\partial \hat{x}}\right), \tag{3.6}$$

which will be useful in analyzing molecular-transport effects. In the absence of breakdown, the flow is slender, so that with the scalings selected in (3.2)–(3.6), all dimensionless variables and their derivatives remain of order unity. Steady solutions can be described by integrating

for $\hat{x} > 0$ the QC equations

$$\begin{aligned}
\frac{\partial}{\partial \hat{x}}(\rho v_x) + \frac{1}{r}\frac{\partial}{\partial r}(\rho r \hat{v}_r) &= 0 && (3.7)\\
\rho\left(v_x\frac{\partial v_x}{\partial \hat{x}} + \hat{v}_r\frac{\partial v_x}{\partial r}\right) &= -\frac{\partial p}{\partial \hat{x}} + \frac{1}{r}\frac{\partial}{\partial r}\left(\mu r\frac{\partial v_x}{\partial r}\right) && (3.8)\\
0 &= S^2\rho\frac{\Gamma^2}{r^3} - \frac{\partial p}{\partial r} && (3.9)\\
\rho\left(v_x\frac{\partial \Gamma}{\partial \hat{x}} + \hat{v}_r\frac{\partial \Gamma}{\partial r}\right) &= \frac{1}{r}\frac{\partial}{\partial r}\left(\mu r\frac{\partial \Gamma}{\partial r} - 2\mu\Gamma\right) && (3.10)\\
\rho\left(v_x\frac{\partial T}{\partial \hat{x}} + \hat{v}_r\frac{\partial T}{\partial r}\right) &= \frac{1}{r}\frac{\partial}{\partial r}\left(\frac{k}{Pr}r\frac{\partial T}{\partial r}\right), && (3.11)
\end{aligned}$$

obtained by taking the limit $Re \gg 1$ in (3.2)– (3.6), with the same inlet velocity and temperature boundary conditions given in (2.23)-(2.25) and (2.27). At the lateral boundary $\partial\Omega_l$, located at $r = r_{\max}$,

$$\begin{aligned}
v_x &= \epsilon && (3.12)\\
\frac{\partial v_r}{\partial r} &= 0 && (3.13)\\
\Gamma &= 0 && (3.14)\\
T &= \Lambda && (3.15)
\end{aligned}$$

are applied to simplify the numerical procedure, justified by the slender flow approximation and a sufficiently large value $r_{\max}$. Along the axis $\partial\Omega_a$, the standard regularity conditions are applied

$$\begin{aligned}
\frac{\partial v_x}{\partial r} &= 0 && (3.16)\\
v_r &= 0 && (3.17)\\
\Gamma &= 0 && (3.18)\\
\frac{\partial T}{\partial r} &= 0. && (3.19)
\end{aligned}$$

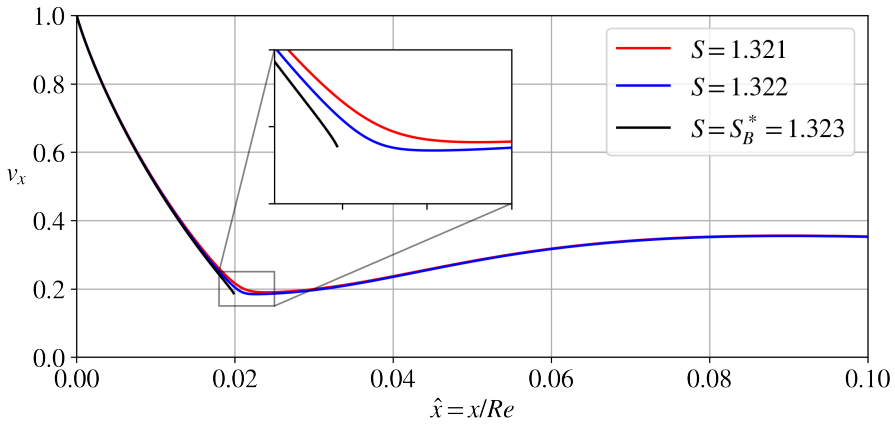

Figure 3.16. Centerline axial velocity for QC integrations indicating singularity corresponding to bubble vortex breakdown for $\Lambda = 5$.

The problem defined in (3.7)–(3.19) was integrated numerically for given values of S and Λ by marching downstream from $\hat{x} = 0$. The integration of the parabolic QC equations employed an implicit method using first-order/second-order approximation schemes for axial/radial derivatives, respectively. At each axial location, a Newton method with a 10^{-5} tolerance is first utilized to compute v_x and $\hat{v}_r$ from (3.7) and (3.8). Next, the boundary value problems given by (3.10) and (3.11) are solved for Γ and T, and the result is used to compute the radial distribution of pressure from (3.9). The density and viscosity are calculated through (2.13) and (2.14), respectively, and a fixed point iteration scheme with a 10^{-5} tolerance is applied until convergence is achieved at the given axial location. The integration then moves to the next axial location, and repeats the same process. The finite difference grid uses spacing $\delta\hat{x} = 5 \times 10^{-5}$ and $\delta r = 10^{-3}$, and integrations were carried out to an axial distance $\hat{x}_{\max} = 0.1$. In the radial direction, the $r \to \infty$ conditions are applied at a truncated boundary placed at $r_{\max} = 15$. Tests were conducted with the radial boundary extended to $r_{\max} = 50$, and critical swirl numbers were found to be identical. To obtain the critical swirl numbers, subsequent integrations were performed in increasing increments of $\Delta S = 0.001$.

The typical evolution of the axial velocity along the axis is shown in the curves of Figure 3.16 for $\Lambda = 5$. The adverse pressure gradient induced by the jet swirl leads to a significant deceleration of the flow that becomes more pronounced for larger values of S.

The numerical integration could no longer converge for $S = 1.323$, with the axial gradients developing a singularity at $\hat{x} = 0.02$. According to Hall (1967), this breakdown of the QC approximation at a given downstream location identifies the critical swirl number S_B^* as the pre-breakdown slender jet transitions to the bubble, an aspect of the problem to be further explored below in § 3.5.2.

The critical swirl number S_B^* associated with the development of a singularity in the numerical integration was calculated for values of the jet-to-ambient density ratio in the range $0.2 \leq \Lambda \leq 5$, with results presented in Table 3.1. Although the critical swirl number varies with Λ, the variation is not very pronounced, $< 1\%$ as Λ increases from 0.2 to 5. The QC theoretical values are smaller than the unsteady values of S_B^*, as may be expected from the decrease of S_B^* with increasing Reynolds numbers (see § 3.3.5).

3.5.2 Steady-state solutions

The QC approximation assumes that the flow is steady and slender upstream from the breakdown point, which requires that the Reynolds number be moderately large, so that the laminar jet remains stable. Under such conditions, the bubble mode prevails when vortex breakdown first occurs on increasing the swirl number, so that the value S^* of S at which the numerical integration of the QC equations fails, shown in Table 3.1, can be reasoned to correspond to the critical swirl number S_B^*.

To further explore this aspect of the problem and ascertain the predictive capabilities of the QC description, the results of the QC approximation will be compared with numerical integrations of the steady form of the NS equations, for a range of large values of Re, shown in Figure 3.17. The numerical integration employs a root-finding scheme involving a Newton-Raphson algorithm (see Appendix), thereby enabling the description of steady solutions even for large values of the Reynolds number for which the flow is unstable. This type of description is needed, for example, in base-flow computations for global linear stability analyses (see, e.g., Moreno-Boza et al. (2016, 2018) for recent sample computations involving

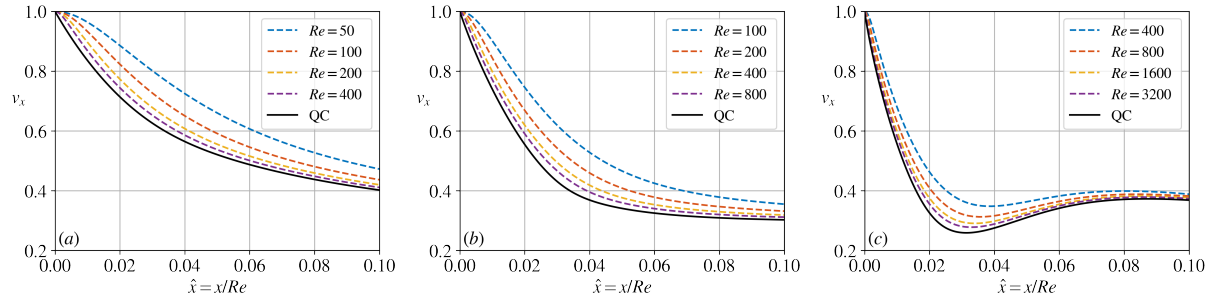

Figure 3.17. Plots of centerline velocity for steady NS and quasi-cylindrical solutions at $S = 1.3$ and (a) $\Lambda = 0.2$, (b) $\Lambda = 1$, and (c) $\Lambda = 5$.

low-Mach-number variable-density flows). The dimensions of the computational domain are identical to the unsteady calculations ($x_{\max} = 80$ and $r_{\max} = 30$), except for solutions with $Re > 800$, for which $x_{\max}$ was extended to 320 to allow for a full comparison with the QC integrations performed on $\hat{x} = x/Re \in [0, 0.1]$. In the former, a total of $E = 53\,460$ finite elements were stretched to produce finer regions where velocity and temperature gradients were large, and the latter employed a similar distribution with $E = 120\,060$ finite elements.

The asymptotic theory underlying the QC approximation envisions the QC velocity field as the limiting solution for $Re \gg 1$ of the steady NS equations, provided that the flow remains slender. This fundamental assumption is tested in Figure 3.17 by comparing the QC predictions of velocity distributions along the axis with solutions to the steady NS equations for $\Lambda = (1/5, 1, 5)$ and increasing values of Re. The value $S = 1.3$ is selected for the swirl number, thereby placing the system near the breakdown conditions predicted by the QC approximation (Table 3.1). The comparisons exhibit the expected convergence when Re increases. Close quantitative agreement of NS and QC results requires values of Re that are higher for the cold jet $\Lambda = 5$ than for the hot jet $\Lambda = 1/5$, as is to be expected given the temperature dependence of the kinematic viscosity and the accompanying associated reduction in effective Reynolds number with increasing Λ (see also the discussion in § 3.2).

To describe the growth of the steady bubble, the numerical integration was extended to values of $S > S_B^*$ for $\Lambda = 2$, where the solution was able to pass through the transition without any singularities. While conical breakdown has been detected in previous steady

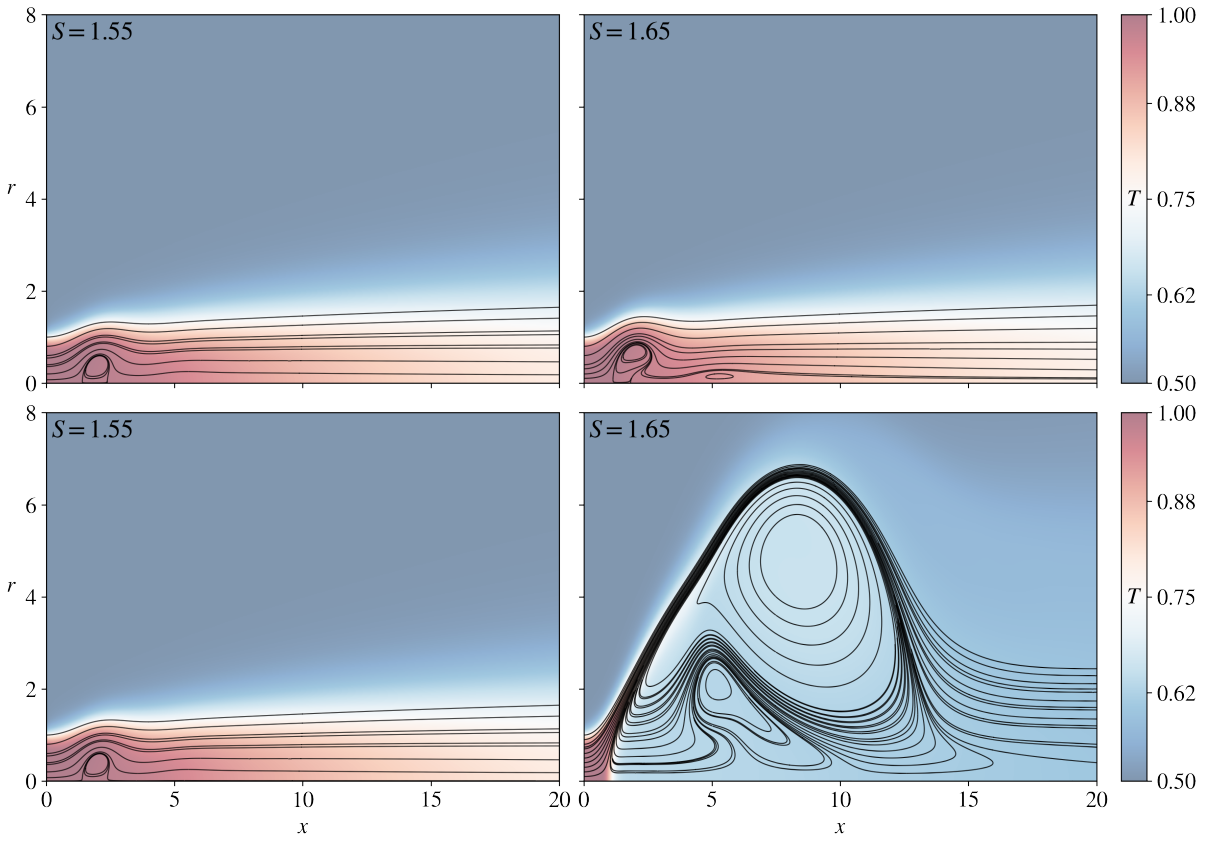

Figure 3.18. Projected streamlines colored with temperature for $\Lambda = 0.5$ and $Re_{eff} = 200$ obtained from the steady NS simulations (top row) and corresponding results obtained by time-averaging the solution of the unsteady axisymmetric NS computations (bottom row).

axisymmetric computations (Douglas et al., 2021), it was later determined that effects of confinement were responsible for these solutions (Douglas and Lesshafft, 2022). In the steady NS computations for this work, the bubble was seen to persist as the value of S was increased beyond the critical transition value S_C^* predicted by the unsteady simulations (discussed in § 3.3.4). The persistence of the bubble is illustrated in Figure 3.18, which shows projected streamlines corresponding to $\Lambda = 0.5$ and $Re_{eff} = 200$, for which $S_C^* = 1.6$ (Table 3.1). Instead of transitioning to a cone, the bubble recirculation region in the steady computations increases in size beyond S_C^*. These observations indicate that, for the specific boundary conditions considered in our analysis, where confinement is negligible, the description of conical breakdown necessitates the unsteady computations performed in § 3.3.4.

3.6 Conclusion

The steady and axisymmetric forms of the Navier-Stokes equations were successfully used describe the formation of bubble vortex breakdown. The quasi-cylindrical slender-jet conservation equations provide good descriptions of pre-bubble-breakdown flows, including predictions of values of critical swirl numbers for that breakdown and the dependence of such values on the jet-to-ambient density ratio Λ, showing only a small decrease with increasing Λ. These successful results have been verified here as being consistent with the large-Reynolds-number limit of predictions of steady-state, axisymmetric, Navier-Stokes equations, even though the flow, of course, necessarily becomes unstable at sufficiently large Reynolds numbers. Beyond the first transition, unsteady bubble breakdown solutions emerge for increasing values of S, including stagnation points that rotate around the jet axis.

Any breakdown to flows that open into a conical sheet necessitate three-dimensional, time-dependent conservation equations for their proper full description. While it was confirmed that critical swirl numbers were identical for the axisymmetric and fully three-dimensional numerical simulations of isothermal jets, the inclusion non-uniform temperature led to nearly constant values S_C^* from three-dimensional simulations, a trend that was not captured by the axisymmetric unsteady simulations.

The axisymmetric results in this chapter are published in the Journal of Fluid Mechanics 2022. Keeton, Benjamin W.; Carpio, Jaime; Nomura, Keiko K.; Sánchez, Antonio L.; Williams, Forman A.

Chapter 4

Burke-Schumann swirling jet flames

This chapter presents a study of vortex breakdown in non-premixed swirling jet flames. To focus on the fluid mechanics, the analysis considers the Burke-Schumann limit of infinitely fast chemistry, so that the flame is controlled by the mixing. Axisymmetric simulations for the single-jet are performed for fixed Re and different values of the fuel-feed mass fraction $Y_{\mathrm{F},F}$. Critical swirl numbers for the onset of the bubble (S_B^*) and the cone (S_C^*) are determined. Independent effects of the exothermicity γ and the stoichiometric value of the mixture fraction Z_s on these transitions are identified. Theoretical predictions for the transition to the bubble using the QC approximation are also presented. The results are published in the Proceedings of the Combustion Institute (Keeton et al., 2023), and serve as an extension to the variable-density case (Keeton et al., 2022). A description of the simulations will be provided in § 4.1. Results and analysis of the axisymmetric flames are given in § 4.2, followed by the quasi-cylindrical theoretical predictions in § 4.3.

4.1 Simulation description

Axisymmetric simulations are carried out by solving the governing equations (2.8), (2.9), (2.13) and (2.11) in terms of the parameters S, Re, γ and Z_s. To identify each critical swirl number, the Reynolds number was fixed to 800 or 1000, and a series of numerical simulations were performed in increments of $\Delta S = 0.01$ for different values of γ and Z_s. The states were identified in an identical manner to that described in § 3.1.

4.2 Axisymmetric simulations

4.2.1 Computational grid

Calculations for the transition to the bubble employed a non-uniform grid with $(n_x, n_r) = (211, 34)$ spectral elements and $(x_{\max}, r_{\max}) = (100, 50)$, while simulations for the transition to the cone used $(n_x, n_r) = (211, 39)$ and $(x_{\max}, r_{\max}) = (100, 70)$. The fixed time-steps, $\Delta t = 5 \times 10^{-3}$ and $\Delta t = 2.5 \times 10^{-3}$, respectively, were selected to satisfy the CFL condition. For both computational domains, the spectral elements were stretched to accommodate finer regions where the velocity and temperature gradients were large, which primarily occur at the reaction sheet (Figure 4.1). The axial and radial boundaries at $x_{\max}$ and $r_{\max}$ were placed sufficiently far away to avoid numerical contamination.

4.2.2 Transition to the bubble S_B^*

Values S_B^* for the transition to the bubble remain constant across the entire range of dilution ($0.1 \leq Y_{\mathrm{F},F} \leq 1$) for $Re = 800$, as is shown in Table 4.1 and Figure 4.2. In the latter, and the subsequent figures in this chapter, the gold curve is the reaction sheet $Z = Z_s$. The flow, which remains slender for $S \leq 1.35$, with streamlines aligned with the axis, displays for $S = S_B^* = 1.36$ the formation of a two-celled recirculation bubble of transverse size comparable to the jet radius, with a secondary breakdown occurring downstream. The reaction sheet is deflected and passes over the recirculating fuel and products, creating a jet-like flame that lies at radial distances from the axis that are slightly larger than the pre-breakdown case $S = 1.35$. In all cases, the breakdown exhibits only a minor effect on the flame sheet, which eventually reaches the axis downstream.

To explain the lack of influence of the dilution on S_B^* (and the QC predictions to be discussed in § 4.3.1), radial distributions of temperature and axial velocity corresponding to the near-critical case $S = 1.3 < S_B^*$ are shown in Figure 4.3 for different values of $Y_{\mathrm{F},F}$. As can be seen, fuel-feed dilution results in significant changes of the temperature across the

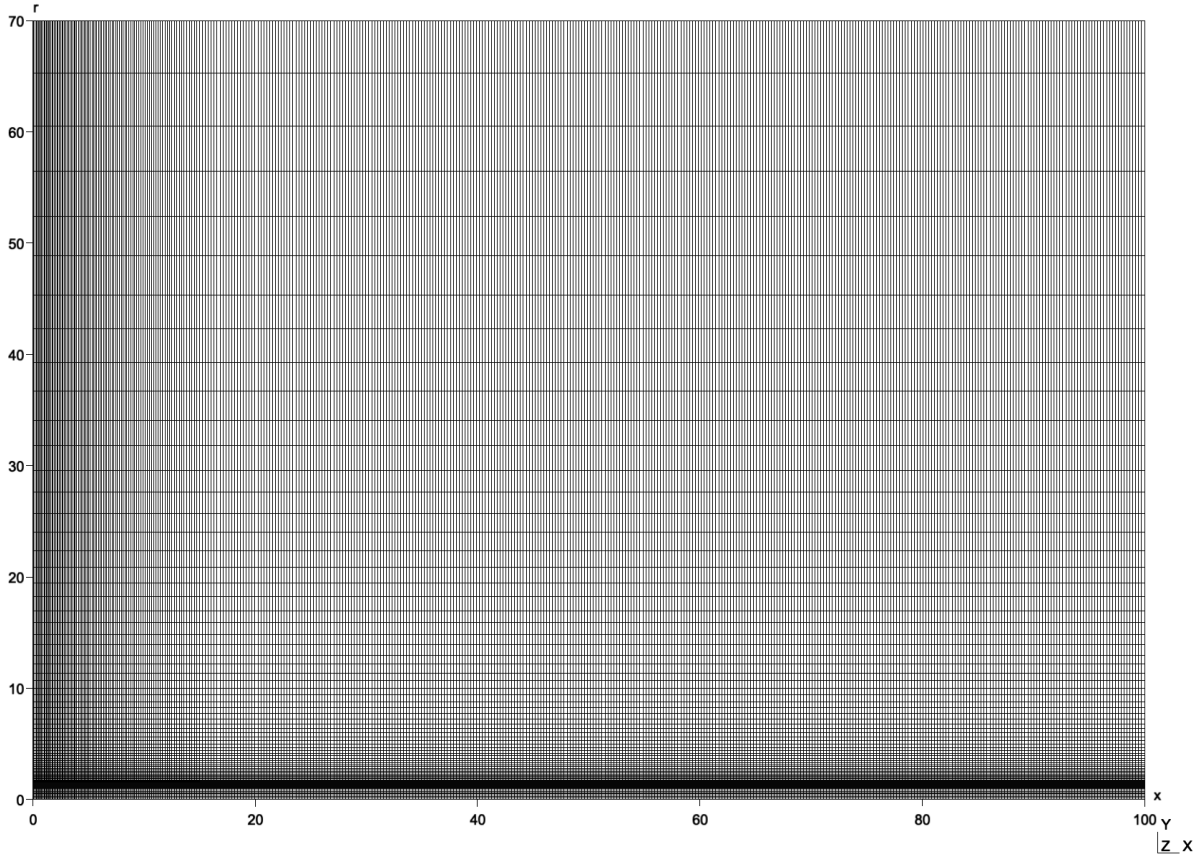

Figure 4.1. Axisymmetric spectral element skeleton for the Burke-Schumann solutions near the transition to the cone.

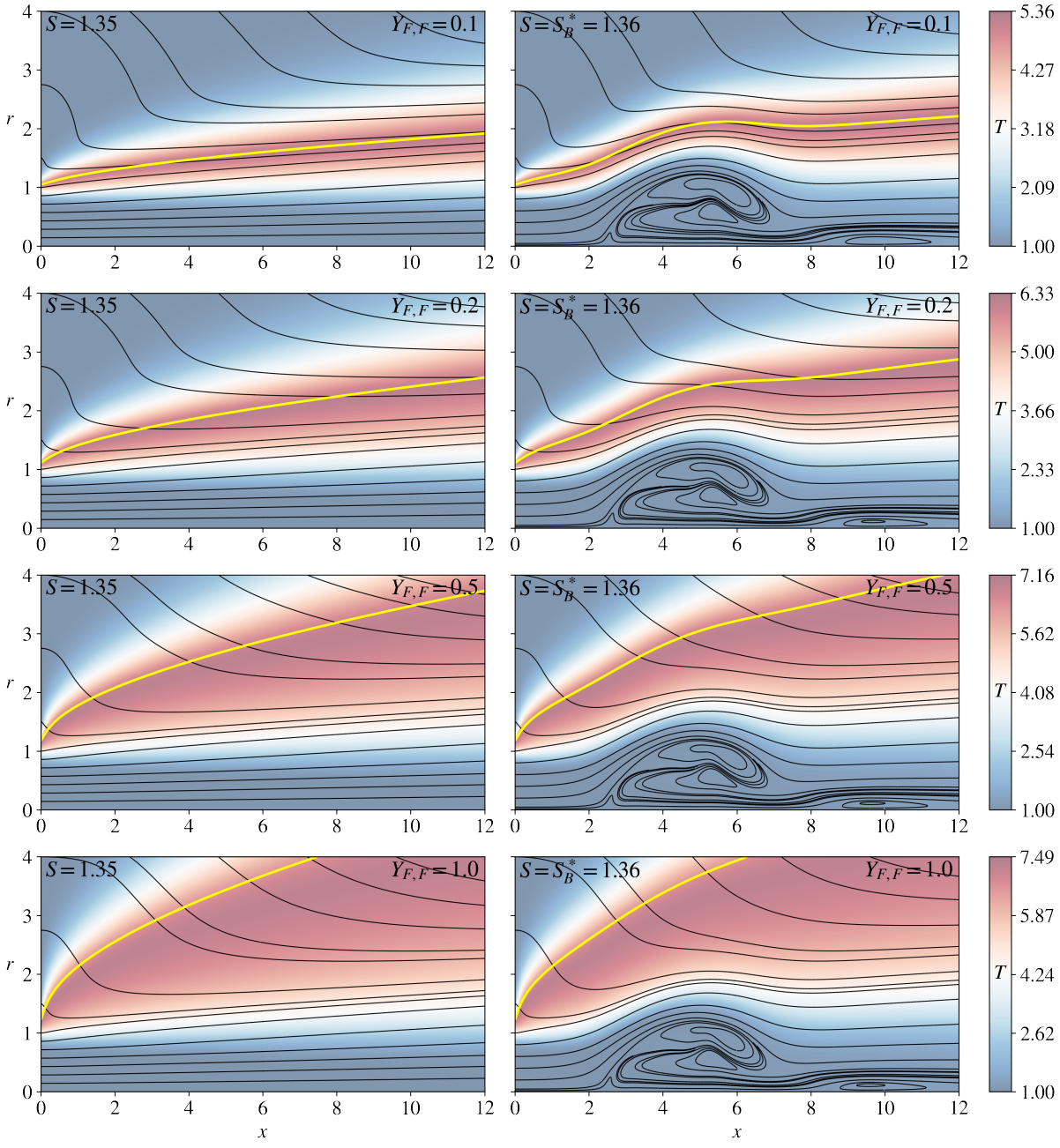

Figure 4.2. Steady-state transition to the bubble S_B^* for $Re = 800$. The gold curve is the reaction sheet $Z = Z_s$.

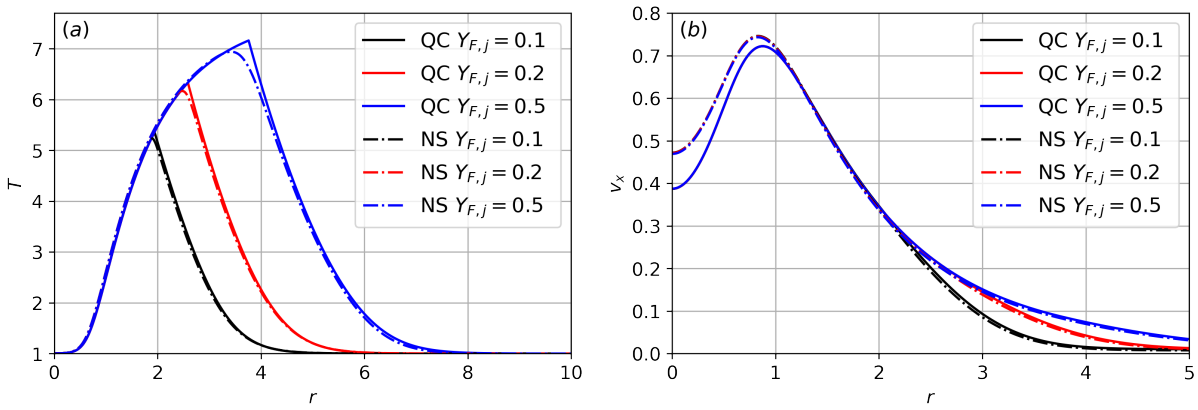

Figure 4.3. Comparison of temperature and axial velocity profiles at $\hat{x} = x/Re = 0.015$ for $S = 1.3$ and $Re = 1000$ and various values of $Y_{\mathrm{F},F}$.

Table 4.1. Critical swirl numbers for various values of fuel-feed mass fraction at $Re = 800$.

$Y_{\mathrm{F},F}$	QC	S_B^*	S_C^*
0.1	1.338	1.36	1.80
0.2	1.339	1.36	1.82
0.5	1.339	1.36	1.83
1.0	1.339	1.36	1.82

envelope of hot products and air that surrounds the flame, while the interior structure of the jet extending extending radially from the axis to the flame remains unperturbed. Since the stagnation point (and thus the singularity of the QC integrations) develops near the axis, where the flow is independent of $Y_{\mathrm{F},F}$, the resulting values of S_B^* are nearly identical in all cases.

4.2.3 Transition to the cone S_C^*

The conical breakdown flow and flame morphology at $S = S_C^*$ depends critically on the fuel dilution, as shown in the selected sample computations displayed in Figures 4.4 and 4.6 for $Re = 800$. Note that these two plots are scaled differently due to the difference in spatial extent of each transition.

The typical evolution will first be described for cases with moderate dilution ($Y_{\mathrm{F},F} \geq 0.2$), corresponding to Figure 4.4. As S is increased beyond $S_B^* = 1.36$, the swirl-induced

adverse pressure gradient increases and the steady two-celled bubble continuously grows in size. The enhanced scalar transport with increasing S results in reduced values of the mixture fraction within the jet and a corresponding reduction in flame length. For $Y_{\mathrm{F},F} = 0.2$ and $S = S_C^* = 1.82$, a second abrupt transition occurs leading to the formation of a steady compact one-celled cone, shown in the top panel of Figure 4.4. Except for $(Y_{\mathrm{F},F}, S) = (0.1, S_C^*)$, to be discussed below, all flows reached a statistically steady state characterized by changes in the axial velocity smaller than 7.5×10^{-3} over a duration of $\Delta t = 250$. During this transition, the flow opens and the pressure along the centerline jumps to the ambient value, as shown in Figure 4.5(b). The negative axial velocities, shown in Figure 4.5(a), continue further downstream, corresponding to the single large cell which recirculates hot products, increasing the temperature inside the breakdown region. The flame sheet, however, again passes around the recirculation region similar to the bubble, maintaining a jet-like flame. A similar two-stage transition is observed for $Y_{\mathrm{F},F} = 0.5$ and 1, as is shown in the bottom panels of Figure 4.4.

The most diluted jet, corresponding to $Y_{\mathrm{F},F} = 0.1$, exhibits similar behavior for $S < S_C^*$ as described above. However, a transition to an unsteady cone occurs at $S_C^* = 1.80$, with corresponding time-averaged streamlines shown in the right panel of Figure 4.6, and instantaneous fields in Figure 4.7. A temporal average of 41 instantaneous fields spanning the interval $47\,000 \leq t \leq 48\,000$ was sufficient for determining the average behavior. For this small value of $Y_{\mathrm{F},F}$, Z_s is large, moving the reaction sheet inward closer to the jet axis. The viscosity is reduced because of the small value of γ (4.36), and the recirculation region becomes unstable, opening into an enlarged unsteady cone, a state also found for cold variable-density jets (Figure 3.7).

The unsteady nature of the flow is shown in the instantaneous temperature contours in Figure 4.7, where vortex shedding modes persist in the far-field. The resulting flame shape, which is relatively fixed in time (see Figure 4.7 and the inset of the right plot in Figure 4.6), is no longer jet-like, but is confined close to the inlet and surrounds the fixed

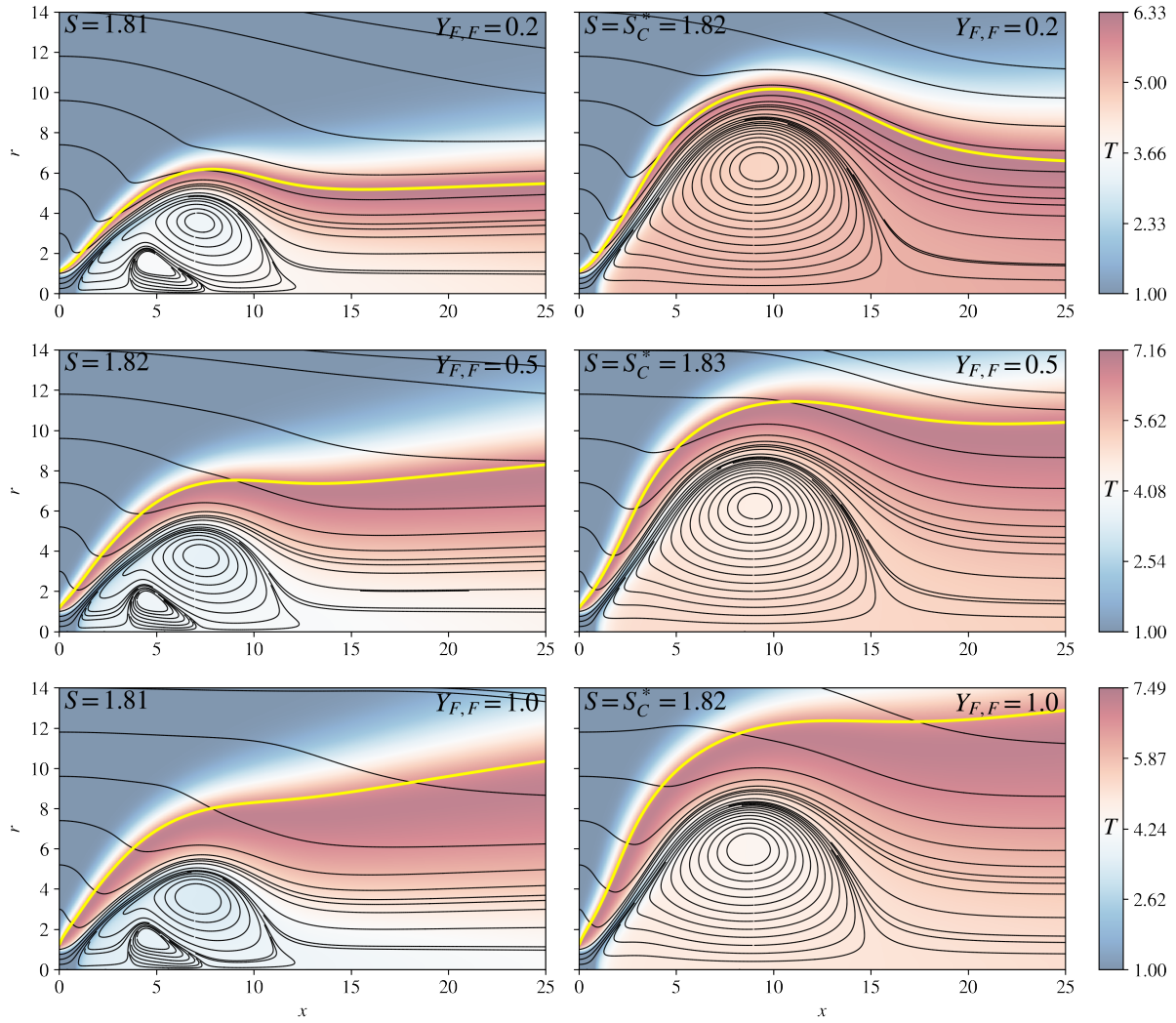

Figure 4.4. Projected streamlines superimposed on color contours of temperature before and at the transition to the cone for $Y_{\mathrm{F},F} = (0.2, 0.5, 1)$ and $Re = 800$.

portion of the conical sheet. As discussed earlier, enhanced mixing with increased S causes the flame length to decrease. For $Y_{\mathrm{F},F} = 0.1$, the larger value of Z_s causes the flame sheet to move into the recirculation region during the transition, and eventually stabilize along the cone. The resulting recirculation cell now extends further out and entrains fresh air that feeds the rear surface of the flame stabilized near the inlet.

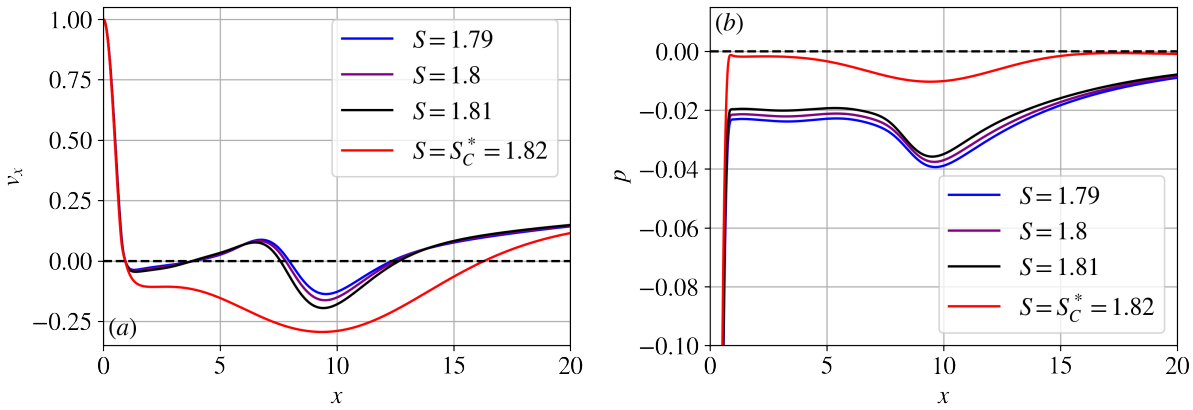

Figure 4.5. Plots of (a) centerline axial velocity and (b) centerline pressure before and at the transition to the cone for $Y_{\mathrm{F},F} = 0.2$ and $Re = 800$.

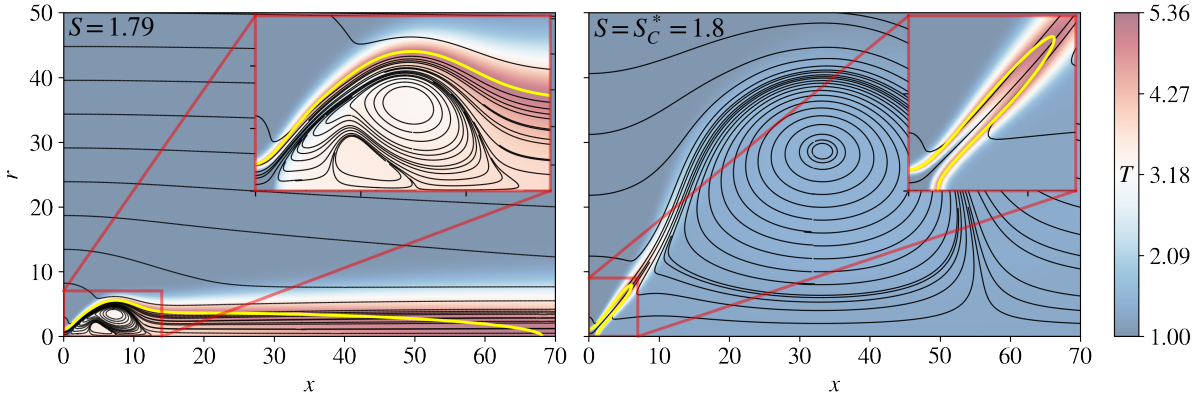

Figure 4.6. Time-averaged projected streamlines superimposed on color contours of temperature before and at the transition to the cone for $Y_{\mathrm{F},F} = 0.1$ and $Re = 800$.

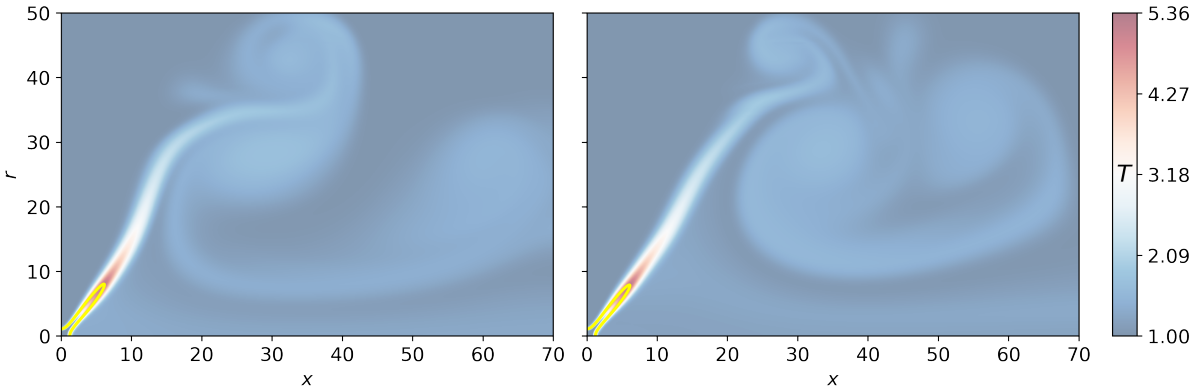

Figure 4.7. Instantaneous color contours of temperature for $S = S_C^* = 1.80$, $Y_{\mathrm{F},F} = 0.1$ and $Re = 800$ at $(a)\, t = 47\,000$ and $(b)\, t = 48\,000$.

Table 4.2. Critical swirl numbers for various values of thermochemical parameters at $Re = 800$.

γ	Z_s	QC	S_B^*	S_C^*
4.36	0.223	1.332	1.35	1.82
5.33	0.223	1.339	1.36	1.82
6.49	0.223	1.347	1.37	1.81
5.33	0.054	1.332	1.35	1.83
5.33	0.223	1.339	1.36	1.82
5.33	0.365	1.346	1.37	1.79

4.2.4 Effects of thermochemical parameters

For increasing dilution of the fuel jet (decreasing values of $Y_{\mathrm{F},F}$), Z_s increases and γ decreases. To identify the independent effects of Z_s and γ, critical swirl numbers were calculated after modifying one of these parameters, holding the other fixed, and the results were compared to the reference case $Y_{\mathrm{F},F} = 0.2$ ($\gamma = 5.33$, $Z_s = 0.223$) in Table 4.2, which also include predictions obtained using the quasi-cylindrical approximation, to be discussed in § 4.3.

Increasing γ delays the transition to the bubble through the increased viscosity, resulting in a higher S_B^*. This trend is consistent with previous computations of constant-density (Moise and Mathew, 2021) and variable-density (Keeton et al., 2022) jets, where values of S_B^* were found to increase for decreasing values of the Reynolds number. The physical mechanism for this trend will be elaborated in the following section (§ 4.2.5). Although viscous effects increase with higher γ, the transition to the cone is promoted (i.e. smaller S_C^*). This can be explained by noting that, unlike the previous investigations of constant-density and variable-density jets Keeton et al. (2022), the velocity divergence from equation (2.36) is non-negligible in the reactive case, and increases in magnitude for larger values of γ. The increased positive radial velocities inside the flame envelope, associated with this thermal expansion, enlarge the bubble's recirculation zone, leading to lower values of S_C^*.

As Z_s decreases, the reaction sheet is positioned at larger radial distances from the axis, decreasing the temperature in the mixing layer and increasing the centerline adverse axial pressure gradient, lowering S_B^*. Increases in Z_s move the reaction sheet radially inward, increasing the temperature in the recirculation region and decreasing S_C^*.

The counteracting effects of changes in Z_s and γ for changes in $Y_{\mathrm{F},F}$ lead to the constant values S_B^* in Table 4.1. For the transition to the cone, the effects from the decrease in Z_s outweigh the effects of increasing γ as $Y_{\mathrm{F},F}$ increases from 0.1 to 0.2, raising S_C^*. For further decrease in dilution in the range $0.2 \leq Y_{\mathrm{F},F} \leq 1$, the decrease in Z_s is small, and the increase in γ balances these effects, leading to nearly constant values S_C^*.

4.2.5 Effects of Reynolds number

Critical swirl numbers were calculated for increasing Re for $Y_{\mathrm{F},F} = 0.2$. For $Re = (800, 1000)$, it is found that $S_B^* = (1.36, 1.35)$ and $S_C^* = (1.82, 1.81)$, indicating that the small increase in the Reynolds number slightly decreases both critical swirl numbers. At the moderately low Reynolds numbers considered, increases in Re decrease the viscous damping effects on the wave motions associated with the formation of bubble breakdown, decreasing S_B^*. This effect also leads to an increase in the overshoot of the initial divergence of the streamlines (Figure 4.8), increasing the size of the bubble, and promoting the jump to the cone (lower S_C^*). While variation in both critical swirl numbers is small in the range $800 \leq Re \leq 1000$, the effect on the flow, illustrated in Figure 4.8, is more pronounced, and the enlarged breakdown of the higher Re bubble considerably increases the temperature along the jet axis. All of these observations are consistent with the previous analysis on variable-density swirling jets (§ 3.3.5), although the decrease in S_C^* with increasing Re is less pronounced for the flames.

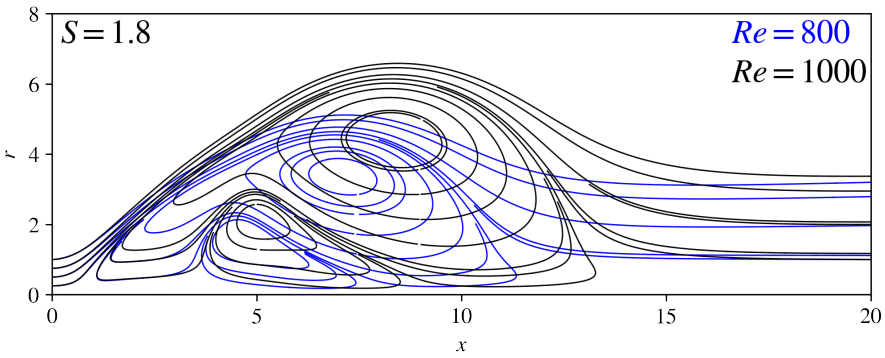

Figure 4.8. Projected streamlines for bubble breakdown at $Y_{\mathrm{F},F} = 0.2$ and $Re = 800$ (blue) and $Re = 1000$ (black).

4.3 Theoretical predictions of vortex breakdown

4.3.1 Quasi-cylindrical approximation

The QC problem defined in (3.7)–(3.19) can be used to describe the Burke-Schumann flames by replacing the energy equation (3.11) with the mixture fraction equation

$$\rho\left(v_x\frac{\partial Z}{\partial \hat{x}} + \hat{v}_r\frac{\partial Z}{\partial r}\right) = \frac{1}{r}\frac{\partial}{\partial r}\left(\frac{k}{Pr}r\frac{\partial Z}{\partial r}\right), \tag{4.1}$$

and the boundary conditions (3.15) and (3.19) with

$$Z = 0 \tag{4.2}$$

on the lateral boundary (Γ_l) and

$$\frac{\partial Z}{\partial r} = 0 \tag{4.3}$$

on the axis (Γ_a). The finite-difference grid and solver tolerances are identical to those described in § 3.5.1. Instead of using the numerical filter given by equation (2.21), the fine radial spacing of the grid permitted $\xi \to \infty$, so that the temperature is calculated from the piece-wise linear relations (2.17)-(2.18).

The quasi-cylindrical integrations were carried out using the same values of the ther-

mochemical parameters Z_s and γ as the Navier-Stokes simulations. Similar to the unsteady numerical calculations of S_B^* in § 4.2.2, fuel dilution was found to have a negligible effect on breakdown, in that for all values of dilution considered the numerical integration failed at a nearly constant value of S_B^* in the range $1.338 \leq S_B^* \leq 1.339$, as shown in Table 4.1, with the singularity developing at axial locations in the narrow range $0.016 < \hat{x} < 0.0172$. Additional integrations for other values of the thermochemical parameters, reported in Table 4.2, showed also minute changes in resulting values of S_B^*.

The reasoning used in the derivation of (3.7)-(3.11) implies that for slender flows with $S < S_B^*$ the results of the NS integrations should approach for $Re \gg 1$ those of the QC approximation. To test this premise, centerline axial velocities obtained from the unsteady NS simulations for a near-breakdown swirl level ($S = 1.3 < S_B^*$) are compared to those determined with the QC approximation in Figure 4.9. This figure also includes solutions to the steady form of the Navier-Stokes equations branched along Re, using an identical procedure to that described in § 3.5.2 and the Appendix. As the Reynolds number is increased, the slender flow approximation improves, and the Navier-Stokes solutions converge towards the QC prediction. Because of the large viscosity increase in the shear layer, larger Reynolds numbers are needed to obtain agreement in the solutions as compared to the isothermal flow, which was documented in the previous chapter (Figure 3.17). The radial distributions of the NS solutions at an axial location just before breakdown are also in excellent agreement with the QC results (Figure 4.3), except for the slight increase in the jet core axial velocity due to the moderately low Re. Thus, the QC approximation provides an excellent description of the slender pre-breakdown flow and the transition to the bubble S_B^*.

4.4 Conclusions

Unsteady Navier-Stokes simulations have been used to identify the transition to bubble and conical vortex breakdown in unconfined laminar swirling Burke-Schumann flames. For the hydrocarbon flames considered, critical swirl numbers for both the bubble and cone

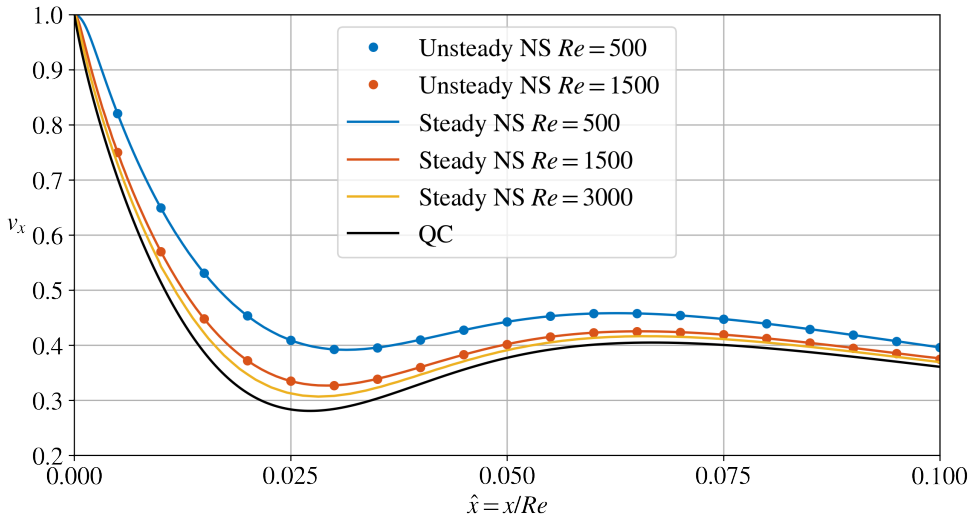

Figure 4.9. Centerline axial velocity obtained from the QC approximation and the steady and unsteady NS simulations for $S = 1.3$ and $Y_{\mathrm{F},F} = 0.2$.

remain relatively constant across a wide range of dilution. Two different forms of the conical breakdown flame were identified. For more realistic values of dilution, a steady compact cone is found with a flame sheet that passes around the recirculation region, forming a jet-like flame. For extreme dilution, an enlarged unsteady cone formed with a recirculation region that stabilizes the flame sheet near the jet inlet. In both cases, the transition from the bubble to the cone leads to increased recirculation of combustion products that considerably increases the temperature within the breakdown region.

The work discussed in this chapter is published in the Proceedings of the Combustion Institute 2022. Keeton, Benjamin W.; Nomura, Keiko K.; Sánchez, Antonio L.; Williams, Forman A. The dissertation author was the primary investigator in this project.

Chapter 5

Concentric swirling jet flames

The single jet flames in the previous chapter showed jet-like flames that passed around the recirculation zone. In practical applications of non-premixed jet flames, the concentric jet configuration (Figure 2.2) is employed so that the flame originates near the primary adverse axial pressure gradient, which is located in the inner shear layer. The flows that arise in this configuration are inherently more complex than the single jet configuration, so that additional analysis on the basic interaction of swirl and heat release is warranted. Progress can be made by first analyzing the laminar axisymmetric flow, and extending this work to higher Reynolds numbers where three-dimensional effects are expected. The work in this chapter will build in physical and computational complexity. First the axisymmetric flow will be discussed for isothermal, Burke-Schumann flames, and finite-rate chemistry. A small portion of the isothermal results will be extended to three-dimensions, to determine whether asymmetries need to be included. The axisymmetric results have been submitted as a manuscript to Combustion & Flame.

5.1 Simulation description

Axisymmetric steady-state solutions for $Re = 200$ were obtained through a series of ramp-and-dwell transient simulations, conducted by linearly increasing/decreasing either S or D_N by a small amount (ΔS or ΔD_N) over a time interval (Δt_S or Δt_{D_N}), and then allowing the solution to dwell at the new fixed value until a steady state is reached. Steady-states

were determined by the criterion that the axial-velocity changes remain smaller than 10^{-3}. This method, consistent with experimental techniques involving small adjustments of a free parameter, also reduces the physical and computational time needed to reach a steady-state. In § 5.2.4, a test will be presented confirming that results are independent of this initial condition. The increments $(\Delta S, \Delta D_N) = (0.1, 0.05)$ and intervals $(\Delta t_S, \Delta t_{D_N}) = (100, 50)$ employed in the computations rendered ramp rates that were sufficiently low to facilitate convergence to the subsequent steady-state solutions. The same breakdown detection criteria used in § 3.1 and § 4.1 will be adopted in this chapter.

For the three-dimensional simulations, initial conditions were generated in a sequential manner, so that variations of S all started from the same initial condition. First, a solution for $Re = 200$ and $S = 1$ was obtained beginning with a stagnant flow initial condition ($\boldsymbol{v} = 0, T = 0$), which was selected to provide a pre-breakdown value of the swirl. After the time-averaged flow reached a statistically steady-state, an instantaneous field file was used as the initial condition for all subsequent values of S at the same value Re. Results for other values Re were obtained in a similar manner. The computational grids used in the different calculations will be discussed in the following sections, along with an axisymmetric grid convergence test in § 5.2.4.

5.2 Axisymmetric simulations

5.2.1 Isothermal jet: increasing S

For the chemically frozen flow ($D_N = 0$), equations (2.8), (2.9) and (2.11) are solved with the stagnant flow initial condition ($\boldsymbol{v} = 0, Z = 0$) and the ramp-and-dwell procedure for increasing values of S. The computational grid consisted of $(n_x, n_r) = (92, 31)$ spectral elements compacted to resolve the mixing and shear layers, and the radial and axial outflow boundaries were placed at $r_{\max} = 60$ and $x_{\max} = 200$, respectively. The fixed time step, $\Delta t = 2 \times 10^{-3}$, was selected to satisfy the CFL condition.

For zero-swirl, the two jets behave independently just off the injector (Chigier and

Beér, 1964), and the centerline axial velocity decays as the central fuel-jet spreads radially and is entrained by the stronger annular jet, as shown in Figures 5.1 and 5.2(a). After the two jets are fully merged, which occurs by $x = 17$ for $S = 0$, the centerline axial velocity begins to decay as a combined jet. As S increases to 1.7, the swirl-induced adverse axial pressure gradient in the air-jet leads to a radial expansion of the flow just beyond the injector. This void is filled by the central fuel-jet, which in turn leads to a more rapid decay of the centerline velocity. At axial distances just beyond the initial expansion, the air-jet merges back toward the fuel-jet axis, where the axial and azimuthal velocity profiles resemble that of an annular jet in solid-body rotation, a flow previously studied through numerical simulations (Douglas et al., 2022). For $S = S_B^* = 1.9$, this distribution of swirl past the initial expansion is sufficient to cause a small vortex breakdown recirculation zone with a stagnation point at $x = 3.5$, as is shown in Figures 5.2(b) and 5.3(b). This recirculation zone is similar to the isolated breakdown case found in swirling annular jets (Douglas et al., 2022), where the central jet would be replaced by a bluff-body. As S increases further to 2.1, the initial expansion of the air-jet leads to a recirculation zone in the fuel/air-jet mixing layer, and the elevated swirl downstream elongates the primary recirculation zone, moving the central-jet axis stagnation point upstream (Figures 5.1(d) and 5.2(d)). Note that the transition to breakdown and flow reversal is gradual in this case because of the low Reynolds number. By way of contrast, more complicated transition patterns, including conical breakdown, have been observed in previous experimental investigations of turbulent concentric jets (Santhosh et al., 2014; Rajamanickam and Basu, 2018).

Typically, single swirling jets exhibit strong hysteresis, often including a bi-stability of the pre-breakdown and bubble breakdown states (Douglas et al., 2021), which are the only modes identified in this work because of the low Reynolds numbers, lack of confinement, and inclusion of the upstream flow. To check for hysteresis, the solution for $S = 2.2 > S_B^*$ was used as an initial condition in a decreasing ramp and dwell simulation with the same ramp rates and convergence criteria. All solutions were found to be identical, confirming

that no hysteresis was present through the transition. The hysteresis previously identified in the same concentric jet configuration (Rajamanickam and Basu, 2018) involves turbulent flow, and is beyond the scope of this work.

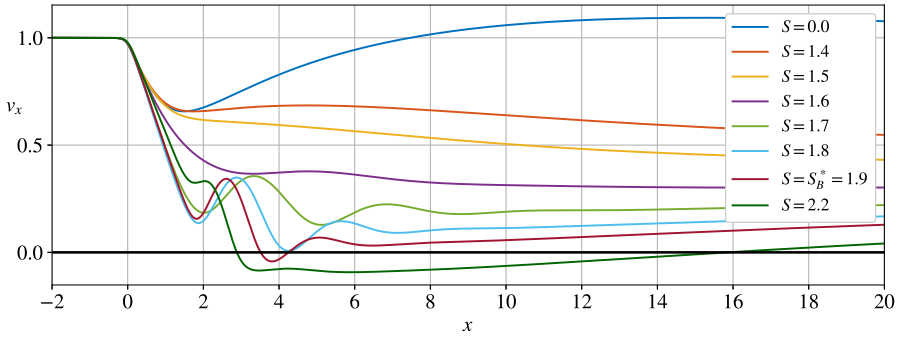

Figure 5.1. Centerline axial velocity for isothermal flow at $Re = 200$ and different values of S.

5.2.2 Burke-Schumann flame: increasing S

Before analyzing order-unity values of D_N for which flames lift off the injector rim, we can consider the Burke-Schumann limit of infinitely fast reaction rate ($D_N \to \infty$), for which the flame remains attached to the injector walls. The inverse filter width (2.19) was set to $\xi = 500$, which was permissible because of the low Reynolds numbers and increase in viscosity with temperature. Beginning with the cold flow solution for $S = 0$, the temperature is assigned a value consistent with the Burke-Schumann solution (2.21), and an increasing S ramp-and-dwell simulation is initiated. The computational grid consists of $(n_x, n_r) = (122, 26)$ spectral elements with $(x_{\max}, r_{\max}) = (100, 50)$, and a fixed time step $\Delta t = 10^{-3}$ was used.

Unlike the isothermal flow, for which the centerline axial velocity just outside of the injector ($x > 0$) decreases (Figure 5.1), the centerline axial velocity associated with the Burke-Schumann flame (Figure 5.4(a)) increases because of the thermal expansion at the base of the flame. The swirl required to produce an axial stagnation point, $S = S_B^* = 4.1$, is thus considerably larger in the case of the burner-attached flame. Also contributing

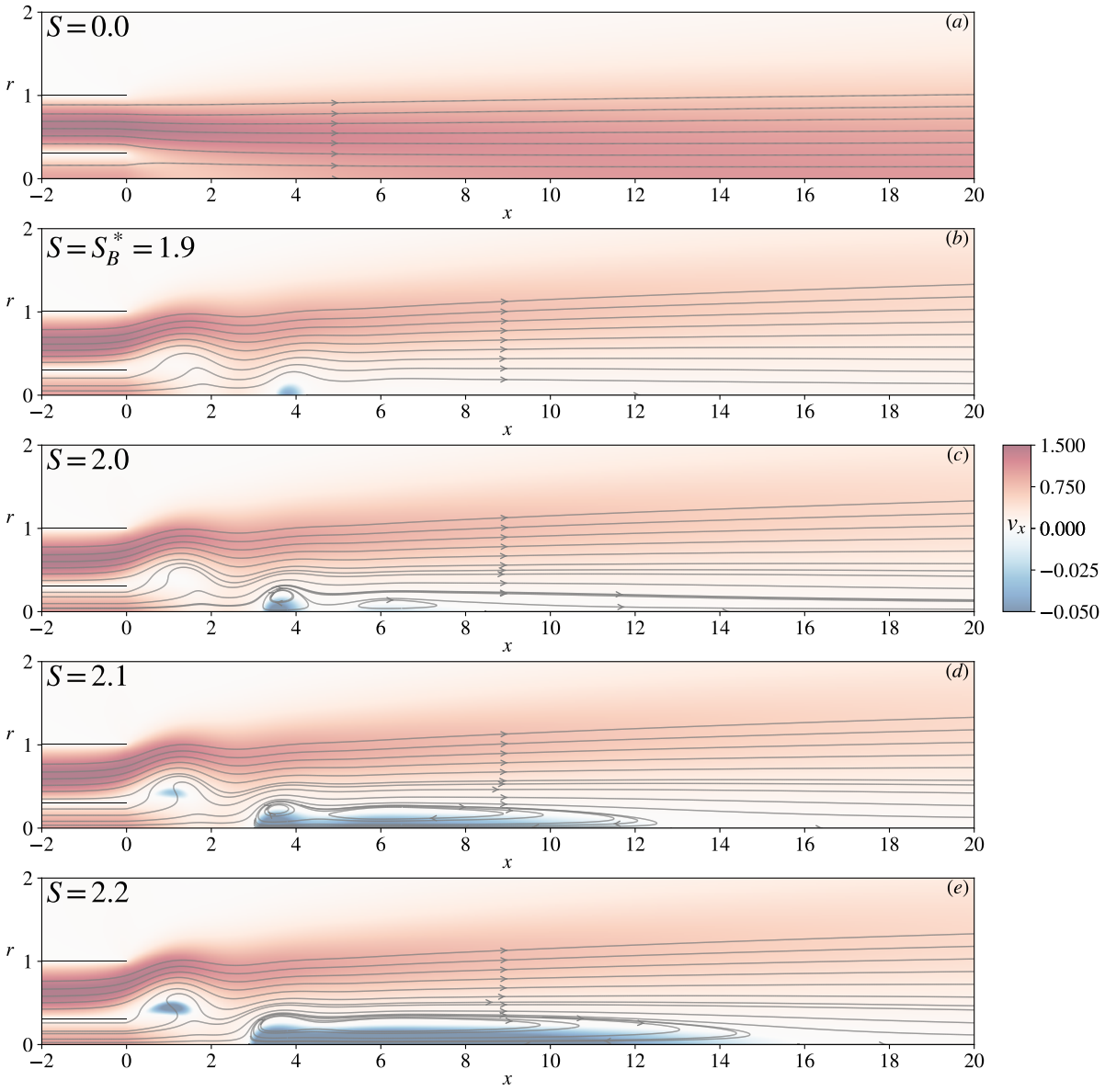

Figure 5.2. Streamlines projected onto the meridional plane colored by axial velocity contours for different values of S.

to this increase is the increase in viscosity that occurs with the high flame temperature ($\nu = T^{1+\sigma}$), which has previously been shown to delay breakdown (Keeton et al., 2022, 2023). The transition to breakdown is again gradual, because of the previously mentioned viscous effects. The recirculation zone, shown for $S = S_B^* = 4.1$ in Figure 5.4(b), is located within the region of fuel and products, and does not considerably affect the flame height or shape compared to those of subcritical solutions $S < S_B^*$.

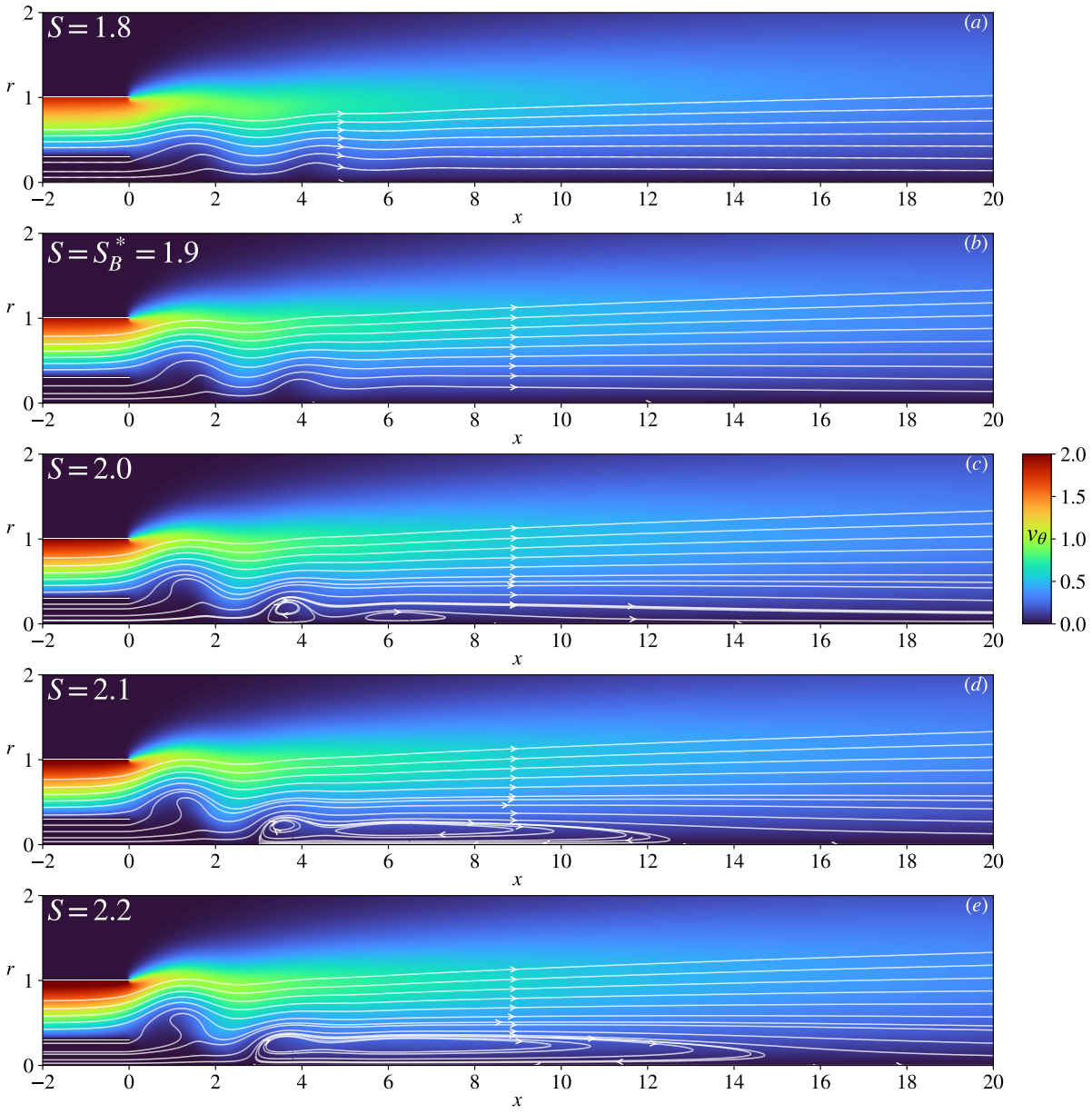

Figure 5.3. Streamlines projected onto the meridional plane colored by azimuthal velocity contours for different values of S.

5.2.3 Zero-swirl flame: decreasing D_N

Beginning with the $S = 0$ Burke-Schumann results from the previous section (§ 5.2.2), a transient simulation for decreasing D_N was conducted with fixed $S = 0$. The computations were initialized at $D_N = 0.95$, a value sufficiently large for the flame to remain attached to the injector. Since the high gradients of velocity, temperature and mixture fraction occur

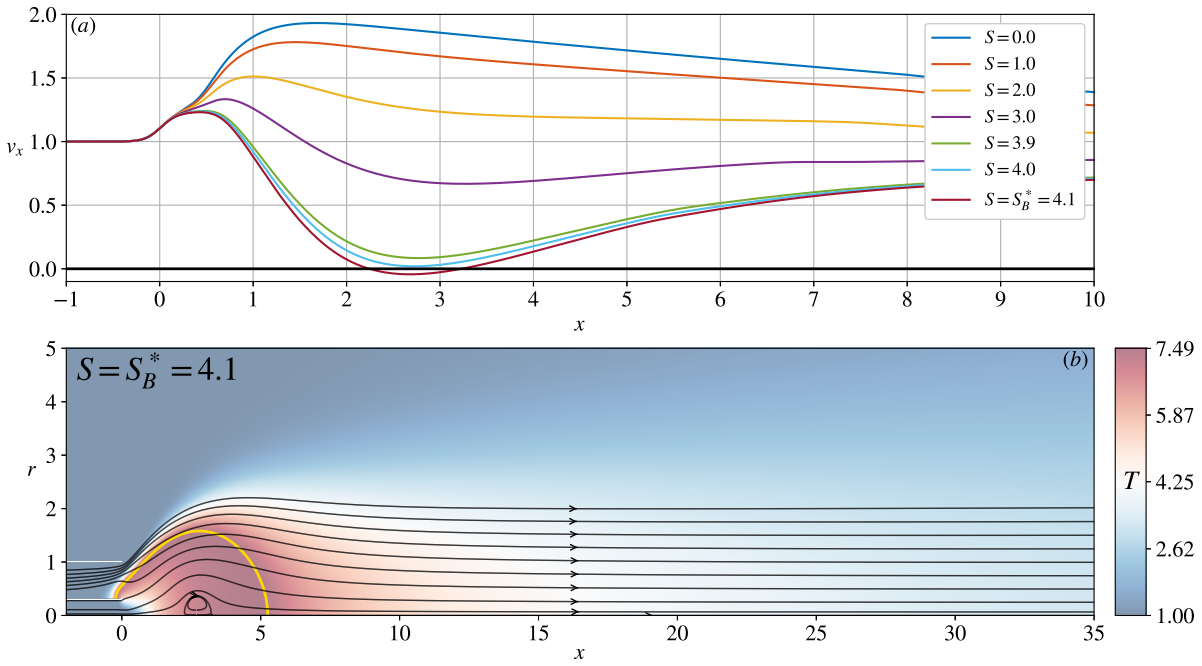

Figure 5.4. Centerline axial velocity for Burke-Schumann flame for different S values (a) and projected streamlines colored by a temperature contour for $S = S_B^* = 4.1$ (b). The gold line represents the stoichiometric surface located at $Z = Z_s$.

near the flame, a series of computational grids were employed that used a uniform spectral element skeleton of $\mathrm{d}x = \mathrm{d}r = 0.05$ to capture the flame as it traveled downstream. The remaining spectral elements were stretched, increasing in size at larger distances from the flame. For $D_N = 0.25$ (fifth row of Figure 5.6), to be discussed later, the refined-grid flame region was located in the coordinate range $24 \leq x \leq 34$ and $0 \leq r \leq 2.5$, so that the total number of axial and radial elements were $(n_x, n_r) = (280, 56)$. The radial and axial outflow boundaries were placed at $r_{\max} = 40$ and $x_{\max} = 80$, respectively, and the time step was fixed to $\Delta t = 6 \times 10^{-4}$. A grid convergence and initial condition test was conducted and will be presented in § 5.2.4 for a case involving vortex breakdown, validating the numerical approach. The same moving-grid procedure, time step, and boundary locations were used for all of the remaining simulations, unless otherwise noted.

For decreasing values of the Damköhler number D_N, the flame moves downstream to regions of lower axial velocity. The axial (x_f) and radial (r_f) flame positions, defined by

the values (x, r) at maximum heat release, are plotted for the zero-swirl flame in Figure 5.5, which also shows the flame height (h_f), determined by the location along the fuel-jet axis where $Z = Z_s$. The results for $S = 1$ will be discussed in the following section.

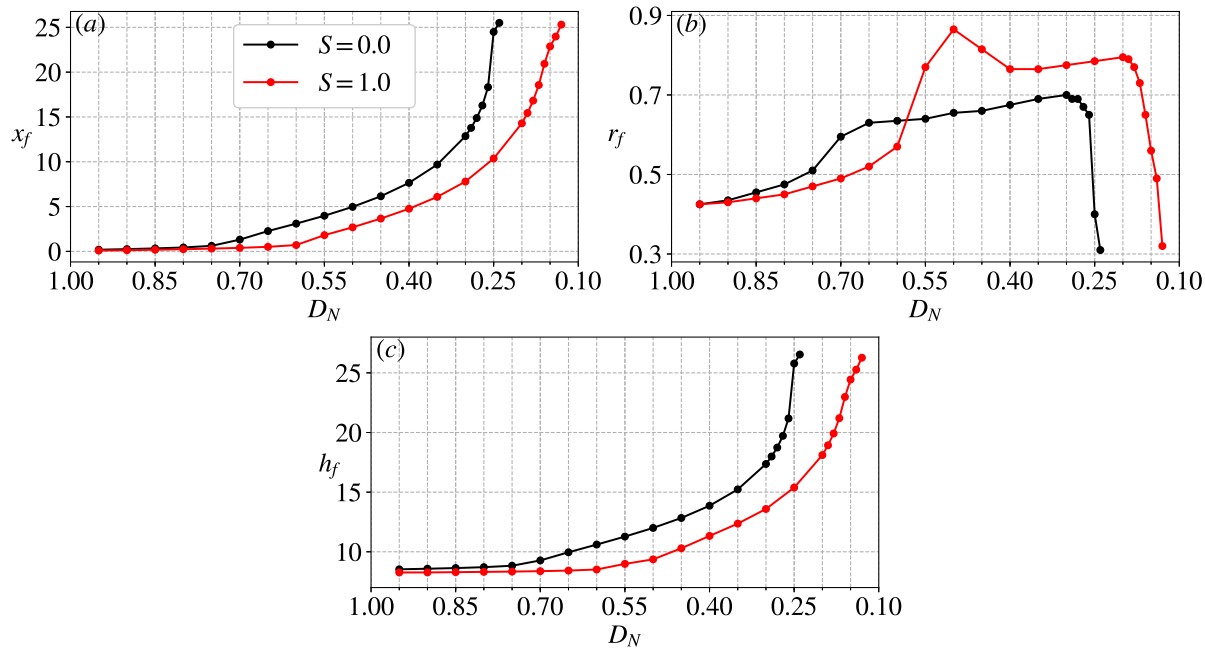

Figure 5.5. Axial flame position (a), radial flame position (b) and flame height (c) for $S = 0$ and $S = 1$ and different values of the Damköhler number D_N.

A more detailed view of the flame structure for $S = 0$ is given in Figure 5.6. For $D_N = 0.95$, the resulting edge flame (first row of Figure 5.6) has a radius of curvature comparable to the flame thickness, and sits just off the jet exit plane ($x_f = 0.19$), on the air side of the mixing layer ($r_f = 0.43$), as needed to achieve stoichiometric conditions when $Z_s \ll 1$. For decreasing values of D_N in the range $0.95 \geq D_N > 0.7$, the flame gradually moves downstream (increasing values x_f) and radially outward (increasing values r_f), but remains close to the injector. These flames are considered attached. For $D_N = 0.7$ (second row of Figure 5.6), a triple flame forms, and the flame begins to move off the injector to usher in a lifted-flame regime. Because the flame sits relatively close to the injectors, there is little decay in the axial velocity of the fuel jet, and the rich branch of the flame is guided toward the air stream. Thermal expansion at the base of the flame leads to a deflection of

the streamlines in the radial direction so that the triple flame moves relative to the incoming cold flow with a velocity that exceeds the propagation velocity of the stoichiometric planar flame, a known result in partially-premixed lifted flames in mixing layers (Ruetsch et al., 1995).

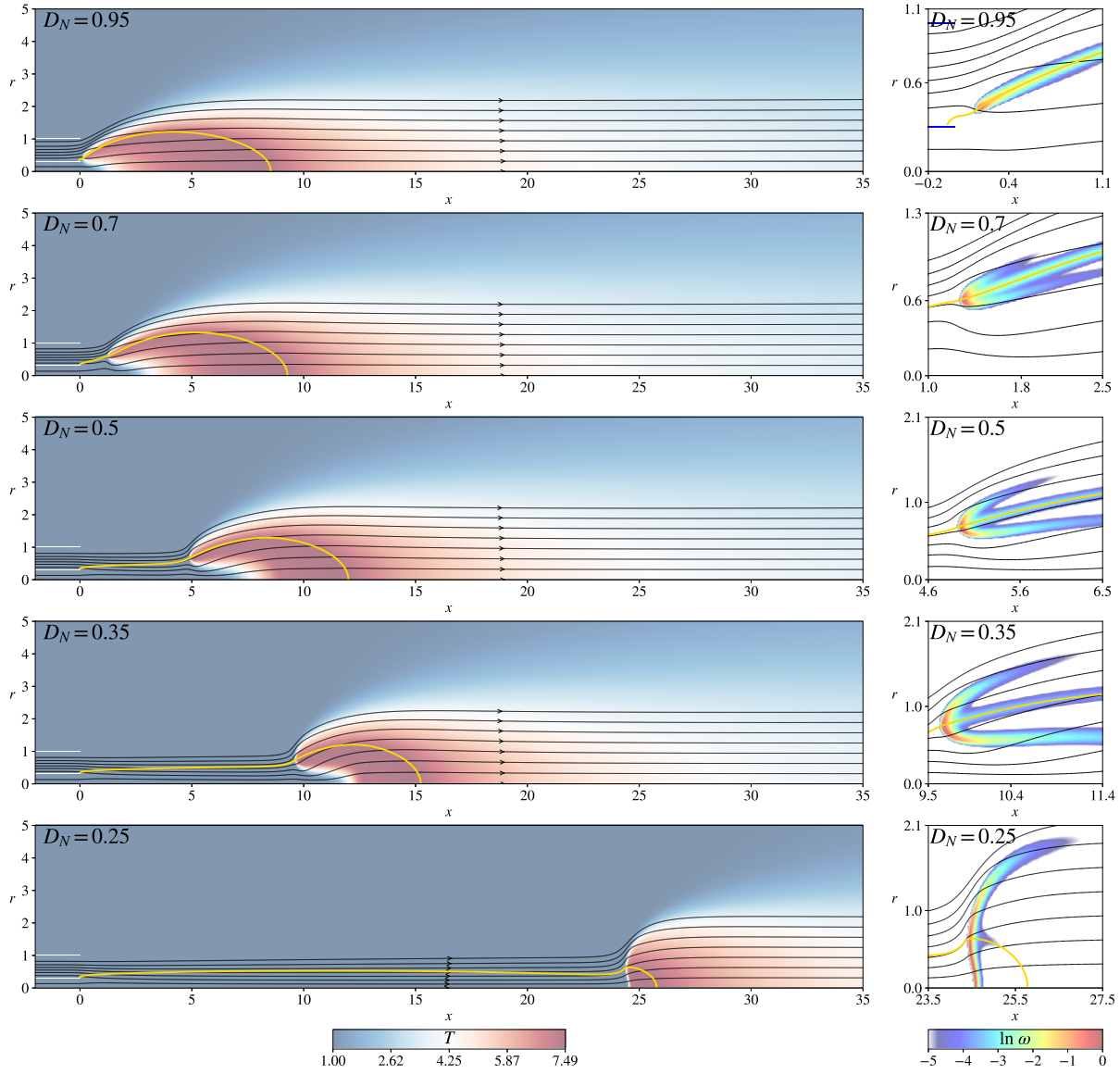

Figure 5.6. Color contours of temperature (left) and reaction rate (right) for $S = 0$ and different values of the Damköhler number D_N. Projected streamlines are shown by black lines and the gold line represents the stoichiometric surface located at $Z = Z_s$.

As D_N decreases further in the lifted-flame regime ($D_N \leq 0.7$), the radius of curvature of the triple flame and associated thermal expansion increase as the flame moves farther

downstream to regions of lower axial velocity, and the rich branch of the flame begins to bend toward the jet axis, as is shown by the color contours of the reaction rate in the fourth row of Figure 5.6. For the computations with $D_N < 0.30$, ΔD_N was reduced from 0.05 to 0.01 (see Figure 5.5) while maintaining the same ramp rate and convergence criteria, so that a more precise blowoff value could be obtained. Further decrease in D_N from 0.26 to 0.25 (fifth row of Figure 5.6) results in an abrupt increase in the flame axial position to a downstream location $x_f = 24.49$ (also Figure 5.5(a)). Since the flame has no effect on the upstream flow, the solution to the cold flow can be used to predict the upstream mixing of fuel and air. For the zero-swirl chemically frozen flow (§ 5.2.1), the concentric jet merging is complete at $x = 17$, a distance far upstream of the flame location $x_f = 24.49$, and the enhanced fuel/air mixing leads to a nearly planar flame, with a weak trailing diffusion flame. The thermal expansion at the base of the flame deflects the flow radially away from the axis, and the lean branch bends downstream. This flattened lean premixed flame has also been identified in experiments of laminar propane jet flames with (Won et al., 2000) and without (Savas and Gollahalli, 1986; Chung and Lee, 1991) coflow, where it served as a precursor for blowoff. When the planar flame forms at $D_N = 0.25$, the existing non-linear liftoff behavior that is found for decreasing D_N exhibits a minor change in curvature, a trend also identified in experiments of coflowing propane jet flames (Lee and Chung, 1997). At the blowoff value $D_{N,b} = 0.23$, the radial position of the flame r_f converges rapidly toward the axis (Figure 5.5(b)), a known mechanism for blowoff in non-premixed jet flames (Chen and Bilger, 2000).

5.2.4 Swirling jet flame at $S = 1$: decreasing D_N

Starting with the Burke-Schumann results with $S = 1$ (§ 5.2.2) as an initial condition, a decreasing D_N simulation was conducted for fixed $S = 1$. At the initialization Damköhler number $D_N = 0.95$ (first row of Figure 5.7), the flame is nearly identical to the non-swirling flame at the same value D_N (first row of Figure 5.6). In this attached regime, effects of swirl

are limited because of the thermal expansion at the base of the flame, a result consistent with previously discussed cases for $D_N \to \infty$. For decreasing D_N, the flame transitions from the attached to the lifted regime at $D_N = 0.55$, a value smaller than the non-swirling case because of the reduced axial velocities associated with the increase in swirl. During this transition, the flame moves off the injector and abruptly outward to $r_f = 0.77$, as is shown in Figure 5.5(b). As D_N is further decreased to 0.5 (third row of Figure 5.7), the radially inward deflection of the flow at the base of the flame redistributes the swirl towards the fuel-jet axis, and a vortex breakdown recirculation region forms, which in turn pushes the flame to larger radial distances. This recirculation zone is absent in the non-swirling case, but does little to alter the existing nonlinear liftoff (x_f) behavior. By $D_N = 0.4$, the flame has moved further downstream, decreasing the strength of the swirl in the vicinity of the flame and destroying the small recirculation zone. Similar to the procedure adopted in the previous section, the calculations for $D_N < 0.2$ used $\Delta D_N = 0.01$ instead of 0.05. As D_N is decreased from 0.16 to 0.15, a planar stoichiometric flame formed far downstream, but its appearance was more gradual than the non-swirling case. As before, the change to the planar flame introduces a small change in the curvature of the liftoff height x_f (Figure 5.5(a)), and occurs just before blowoff at $D_{N,b} = 0.12$, a value that is considerably lower than that of the corresponding non-swirling flame.

To confirm solutions were independent of both grid spacing and the ramp-and-dwell procedure, a numerical simulation was conducted for $D_N = 0.5$ on a refined grid using the Burke-Schumann solution as an initial condition. The refined region used spacing $\mathrm{d}x = \mathrm{d}r = 0.025$ in the coordinate range $-0.5 \leq x \leq 5.5$ and $0 \leq r \leq 2.5$, and the time-step was reduced to $\Delta t = 3 \times 10^{-4}$. Once the flame stabilized downstream, given by the same criteria previously presented in § 5.1, the result was compared to the one given in the third row of Figure 5.7. The two vortex breakdown flames were found to be identical, validating the numerical approach.

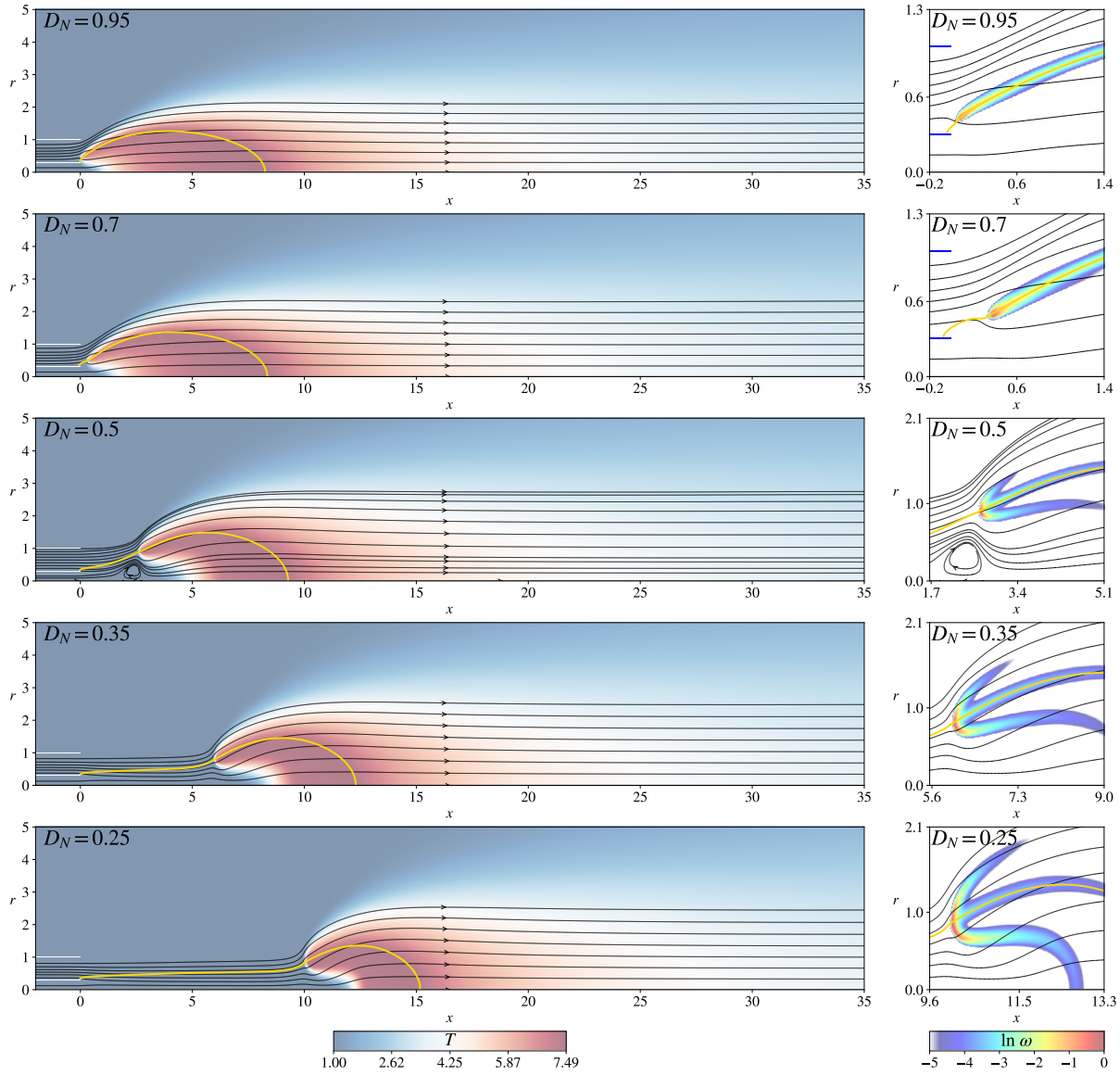

Figure 5.7. Color contours of temperature (left) and reaction rate (right) for $S = 1$ and different values of the Damköhler number D_N. Projected streamlines are shown by black lines and the gold line represents the stoichiometric surface located at $Z = Z_s$.

5.2.5 Swirling jet flame at $D_N = 0.35$: increasing S

Beginning with the zero-swirl steady-state solution for $D_N = 0.35$ (fourth row of Figure 5.6) as an initial condition, a transient simulation for increasing values of S was conducted for fixed $D_N = 0.35$. Steady-state flame positions and heights are plotted in Figure 5.8.

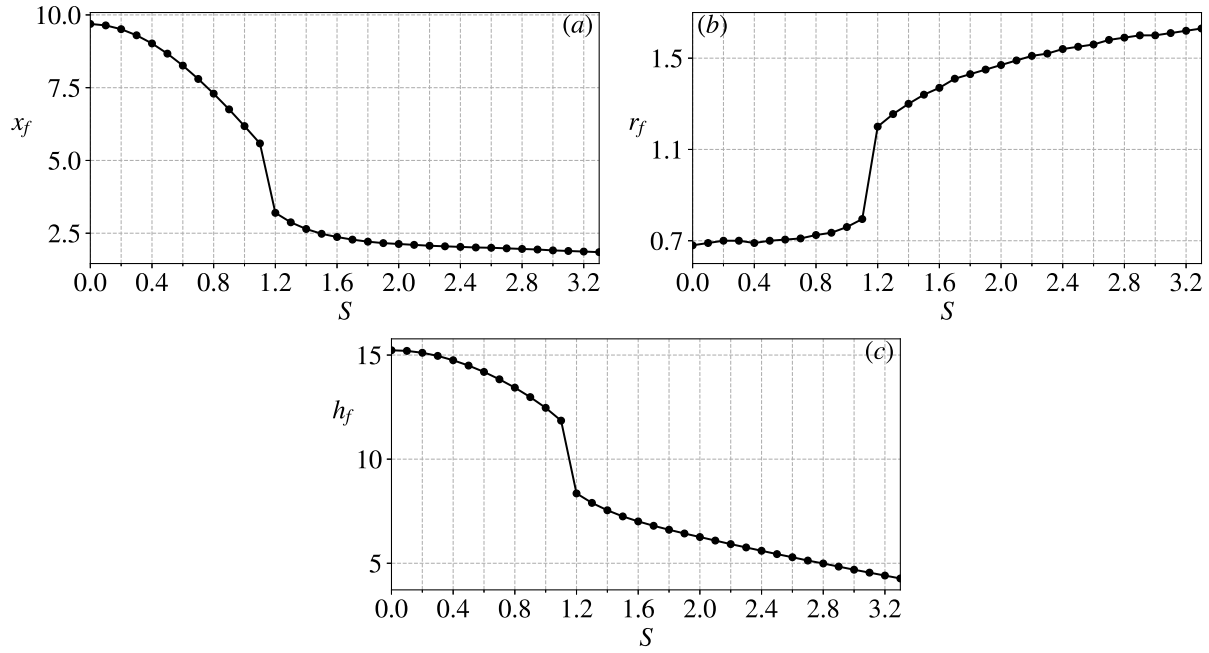

Figure 5.8. Axial flame position (a), radial flame position (b), and flame height (c) for $D_N = 0.35$ and different values of inflow swirl S.

As S increases from $S = 0$, the adverse axial pressure gradient increases, and the axial velocity decreases. Since $D_N = 0.35$ is fixed, the flame moves upstream to match the changes in velocity, as is indicated by the smaller values of x_f in Figure 5.8(a). A radially outward shift of the flame (increasing values of r_f) moves the triple flame toward the inner radius of the air injector at $r = 1$. For $S = 1$, the flame shown in the first row of Figure 5.9 is identical to the one obtained by decreasing D_N (fourth row of Figure 5.7), reconfirming that the solutions are independent of the initial condition, as was discussed in § 5.2.4. As S increases from $S = 1.1$ to $S = S_B^* = 1.2$ (second and third rows of Figure 5.9), the abrupt formation of a recirculation zone occurs because of the thermal expansion at the base of the flame, and the flame position rapidly moves upstream to $x_f = 3.1$. For $S \geq 1.8$, the flame is attached, and while the axial position x_f remains relatively constant, the decreased flow velocity along the central axis shortens the flame (h_f) at a nearly linear rate, as shown in Figure 5.8(c). A simulation for decreasing values of S from 1.7 to 1.1 revealed identical flame positions to the simulation for increasing values of S, so that it can

be concluded that no hysteresis is present during the transition to breakdown for the lifted laminar flames considered here. Hysteresis associated with the transition from an attached to lifted flame, on the other hand, may depend strongly on heat transfer to injectors and the thermal boundary condition there. This aspect of the problem has not been explored further since the focus of this work is on vortex breakdown, which occurs when the flame is lifted off the injector.

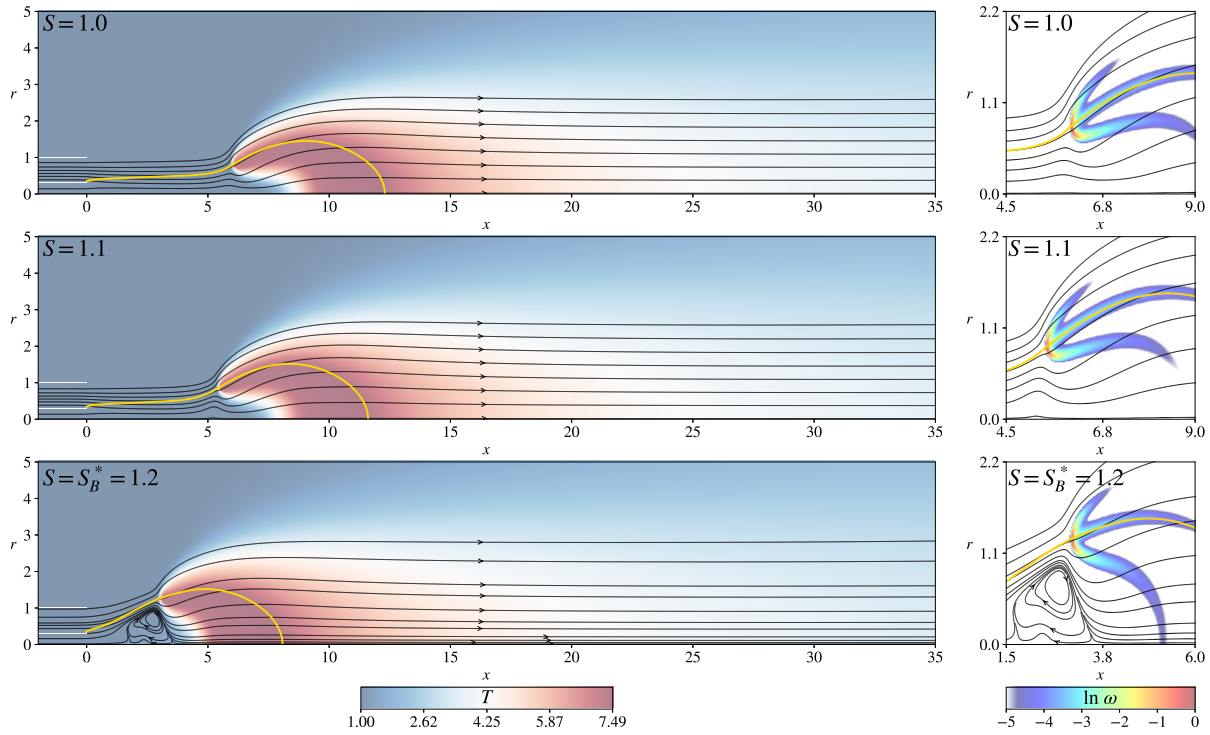

Figure 5.9. Color contours of temperature (left) and reaction rate (right) for $D_N = 0.35$ and different values of the swirl number S. Projected streamlines are shown by black lines and the gold line represents the stoichiometric surface located at $Z = Z_s$.

5.3 Three-dimensional simulations

Previous analyses have shown the applicability of using axisymmetric simulations to study bubble vortex breakdown (chapter 3) for single jets with a fixed-inflow plane. In the concentric jet configuration, a number of distinctions arise such as the inclusion of the upstream flow, the high swirl gradient at the injector exit and the physics of the multi-jet

flow. Thus, further analysis is needed to determine the extent to which vortex breakdown is axisymmetric in this configuration. To check the validity of the axisymmetric assumption on the low-Re flows considered above, identical simulations for the isothermal flow are performed with the fully three-dimensional configuration. The isothermal simulations will also be extended to a larger Reynolds number.

5.3.1 Computational grid

The computational domain is a revolved version of the axisymmetric schematic in Figure 2.2. A region spanning the coordinate range $-1 \leq x \leq 11$ and $0 \leq r \leq 4$ is resolved with a nearly uniform spectral element skeleton with spacing $\mathrm{d}x = \mathrm{d}r = 0.2$, with elements stretched in the far field. The grid is extended to $x_{\max} = 100$ and $r_{\max} = 50$ with the same upstream boundary location $x_{\min} = -10$, yielding a total of $E = 111\,156$ spectral elements. The spectral element skeleton is shown in Figure 5.10.

When the same boundary conditions of § 2.3.3 were applied to the three-dimensional simulations, a stationary counter-winding $|m| = 3$ mode was first observed for all all values of S at $Re = 200$. While steady-state asymmetric flows have been identified in non-swirling annular jets, (Del Taglia et al., 2004, 2009; Douglas et al., 2022), these structures typically rotate around the central axis for any finite amounts of swirl (Douglas et al., 2022). Tests revealed that the instability was spurious, and the result of the sharp boundary conditions on v_θ that exist at the intersection of the rotating pipe wall and the unconfined atmosphere, located at $(x, r) = (0, 1)$. To resolve this numerical issue, the azimuthal velocity along the rotating pipe wall was gradually smoothed to zero at $x = 0$ via a hyperbolic tangent profile, so that $v_\theta = S\tanh(x/0.1)$. The thickness of the smoothing was chosen to be small, and comparisons to the axisymmetric results were agreeable, as will be discussed below.

5.3.2 Isothermal flow: comparison to axisymmetric results

The instantaneous centerline axial velocity is plotted in Figure 5.11 for $S = 1$ and $S = 2$ at $Re = 200$. This figure also includes the corresponding curves for the axisymmet-

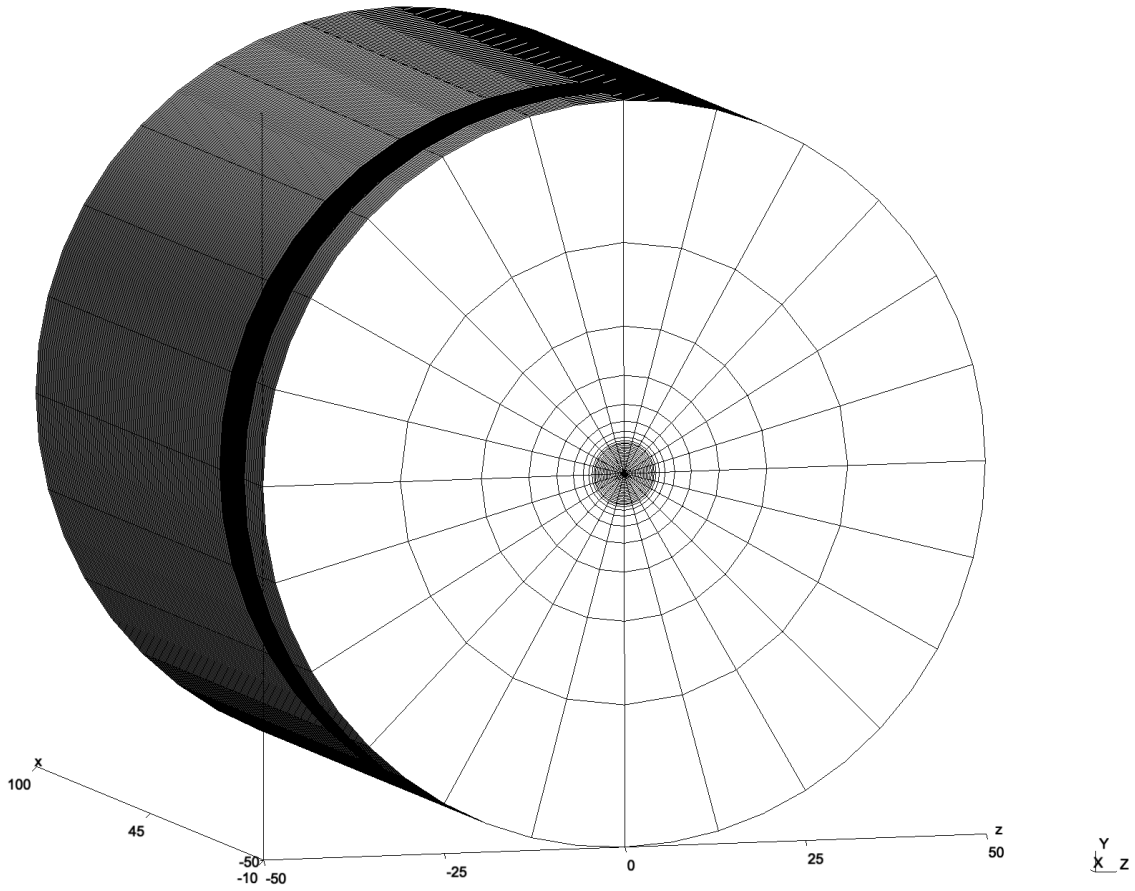

Figure 5.10. Spectral element skeleton for concentric jet three-dimensional computational domain.

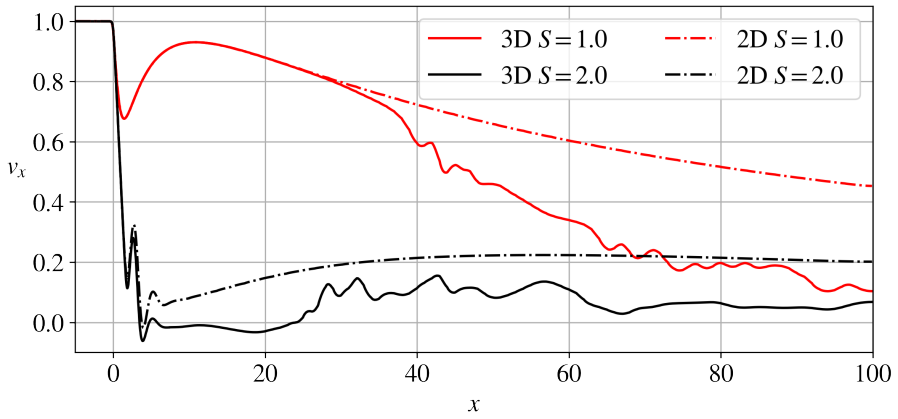

Figure 5.11. Instantaneous centerline axial velocity for axisymmetric (2D) and three-dimensional solutions for isothermal jets at $Re = 200$.

ric solutions, which both achieved a steady-state. The agreement for the pre-breakdown value $S = 1$ is excellent in the region $x \leq 25$, where the flow remains steady and nearly axisymmetric. In the previous analysis (§ 5.2.3 and § 5.2.4), the maximum flame position at blowoff for $S = 1$ was $x_f = 25.3$, and since the upstream flow is unaffected by the flame, this result validates the use of axisymmetric solutions. By $x = 28$, a steady counter-winding $|m| = 4$ mode emerges, as indicated by the axial velocity contour in Figure 5.12(b). Further downstream, the $|m| = 2$ mode becomes dominant and a trident structure appears (Figures 5.12(a, c)), which has previously been observed in both experimental (Billant et al., 1998) and numerical (Moise and Mathew, 2019) studies of single swirling jets.

As the swirl is increased to $S = 2$, vortex breakdown occurs, as shown by the time-averaged streamlines in Figure 5.13, which have also been averaged in the azimuthal direction to improve statistical convergence. For small distances off the injectors ($x < 2$), the flow remains roughly axisymmetric and steady, and agrees well with the 2D computation (Figure 5.11). The process for the formation of the first stagnation point is nearly identical to that described for the axisymmetric solution $S = 2$ in Figures 5.2(c) and 5.3(c), and is summarized as follows. The swirl-induced initial expansion ($x = 0$) of the annular jet (Figure 5.13(b)) leads to a radial expansion of the central jet, which in turn produces a decay of the centerline axial velocity (Figure 5.11). Because of the strong central jet momentum, this

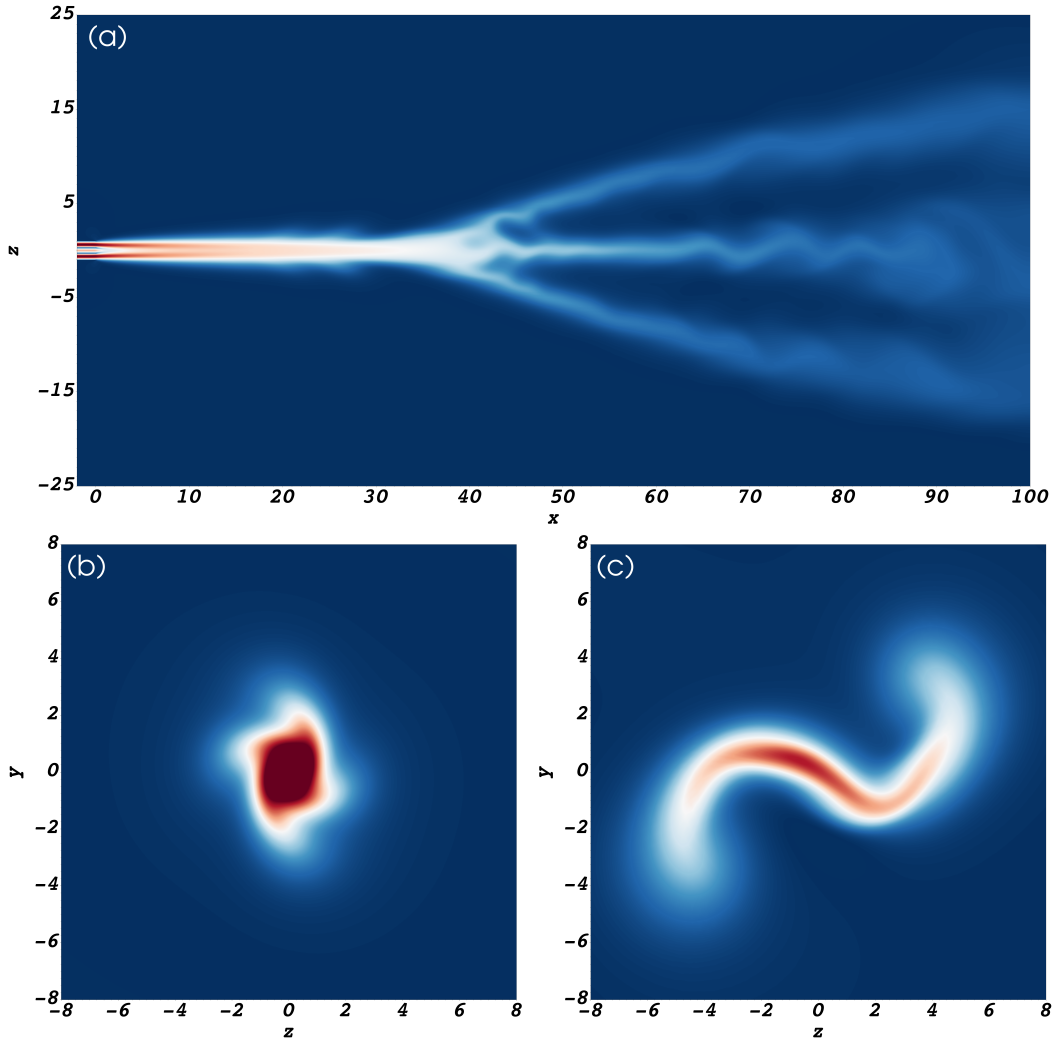

Figure 5.12. Instantaneous results for $S = 1$ and $Re = 200$: (a) color contour of $v_x \in [0, 1.5]$ at $y = 0$, (b) color contour of $v_x \in [0, 0.6]$ at $x = 28$ and (c) color contour of $v_x \in [0, 0.6]$ at $x = 45$. Note that the swirl is clockwise.

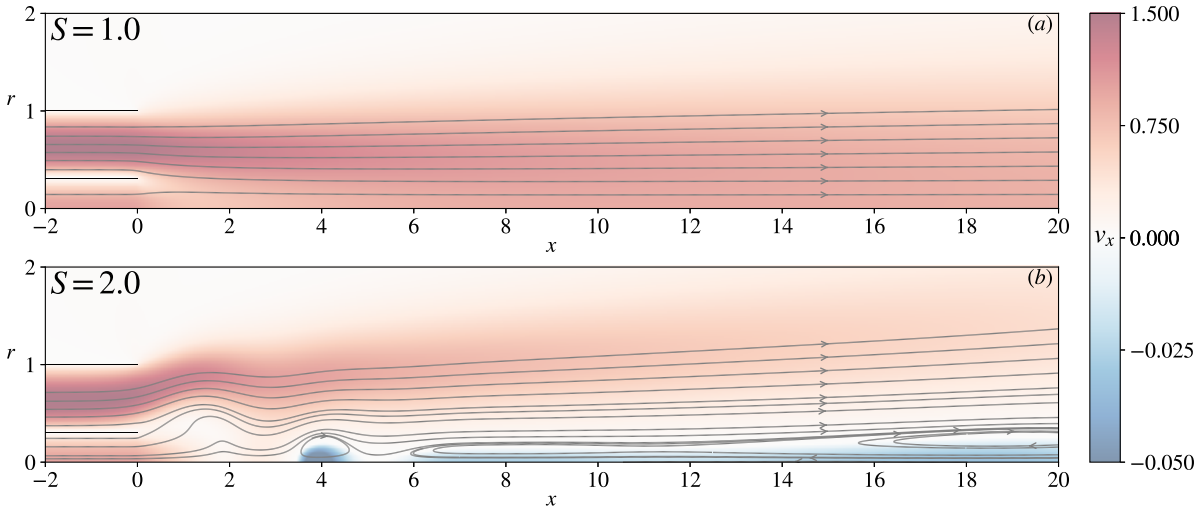

Figure 5.13. Temporal and azimuthally averaged projected streamlines colored by axial velocity for $Re = 200$ and different values of S.

initial expansion is insufficient to produce a stagnation point. The annular jet is deflected back toward the axis at $x = 2$, increasing the centerline velocity and redirecting the swirl towards the axis, so that an axial stagnation point forms at $x = 3.5$, which exhibits a very slight precession around the jet axis. After a slight recovery of the centerline axial velocity ($v_x > 0$), a secondary elongated breakdown occurs as the annular jet spirals around the central axis. This process is depicted in Figure 5.14, where an iso-surface of Q delineates the regions of strong vorticity, and the three-dimensional velocity field is shown by the instantaneous streamlines, which are colored by azimuthal vorticity. This figure clearly indicates the region ($2 \leq x \leq 3.5$) where the central jet acquires the negative azimuthal vorticity required to produce the first breakdown, which also corresponds to the central migration of the annular jet (Figure 5.13). After the first breakdown, the annular jet spirals around the central axis, producing the same effect on the elongated secondary recirculation zone, indicated by the inner Q surface at $x > 6$ in Figure 5.14. Downstream, a counter-rotating co-winding $|m| = 5$ mode occurs in the coordinate range $13 \leq x \leq 23$ (Figures 5.15 and 5.16), beyond which various modes interact to form more complex vortex structures.

Even for these moderate values $S = 2$ and $Re = 200$, small but non-negligible radial

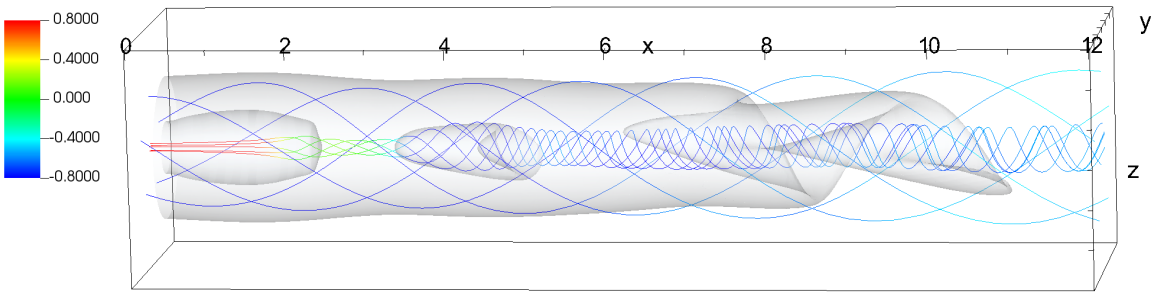

Figure 5.14. Iso-surface of $Q = 0.4$ with instantaneous streamlines colored by azimuthal vorticity for $S = 2$ and $Re = 200$. Streamlines originate in both the central jet at $(x, r) = (0, 0.05)$ and the annular jet at $(x, r) = (0, 0.65)$ with 5 points in the azimuthal direction.

velocities near $x = 0$ (Figure 5.13(b)) highlight the significance of modeling the upstream flow. For an increase to $S = 2.5$, the recirculation zone traveled toward the jet exit plane, deflecting the annular jet within the pipe. Non-zero radial velocities traveled all the way upstream to the Dirichlet inlet ($\partial\Omega_j$) at $x_{\min} = -10$, so that the flow was no longer parallel. Previous computations of swirling jets with pipes extending upstream have replaced (2.30) and (2.33) with Neumann conditions ($\partial v_r/\partial x = 0$), which might be more applicable in these cases.

Although this configuration is limited to moderate values of Re and S so that the upstream flow ($x \ll 0$) remains parallel, allowing for the development of radial velocities near the injector exit plane $x = 0$ is essential for accurately describing vortex breakdown. These effects are neglected in the single jet configuration (Figure 2.1), where a fixed inflow plane at $x = 0$ sets $v_r = 0$, restricting the flow when the stagnation point moves near the inlet plane. Through continuity, this restriction increases the radial expansion of the flow just off the inlet, which may trigger conical breakdown. Details on swirling inflow conditions for turbulent flow, which is beyond the scope of this work, may be found in studies by Pierce and Moin (1998) and Sloan et al. (1986)

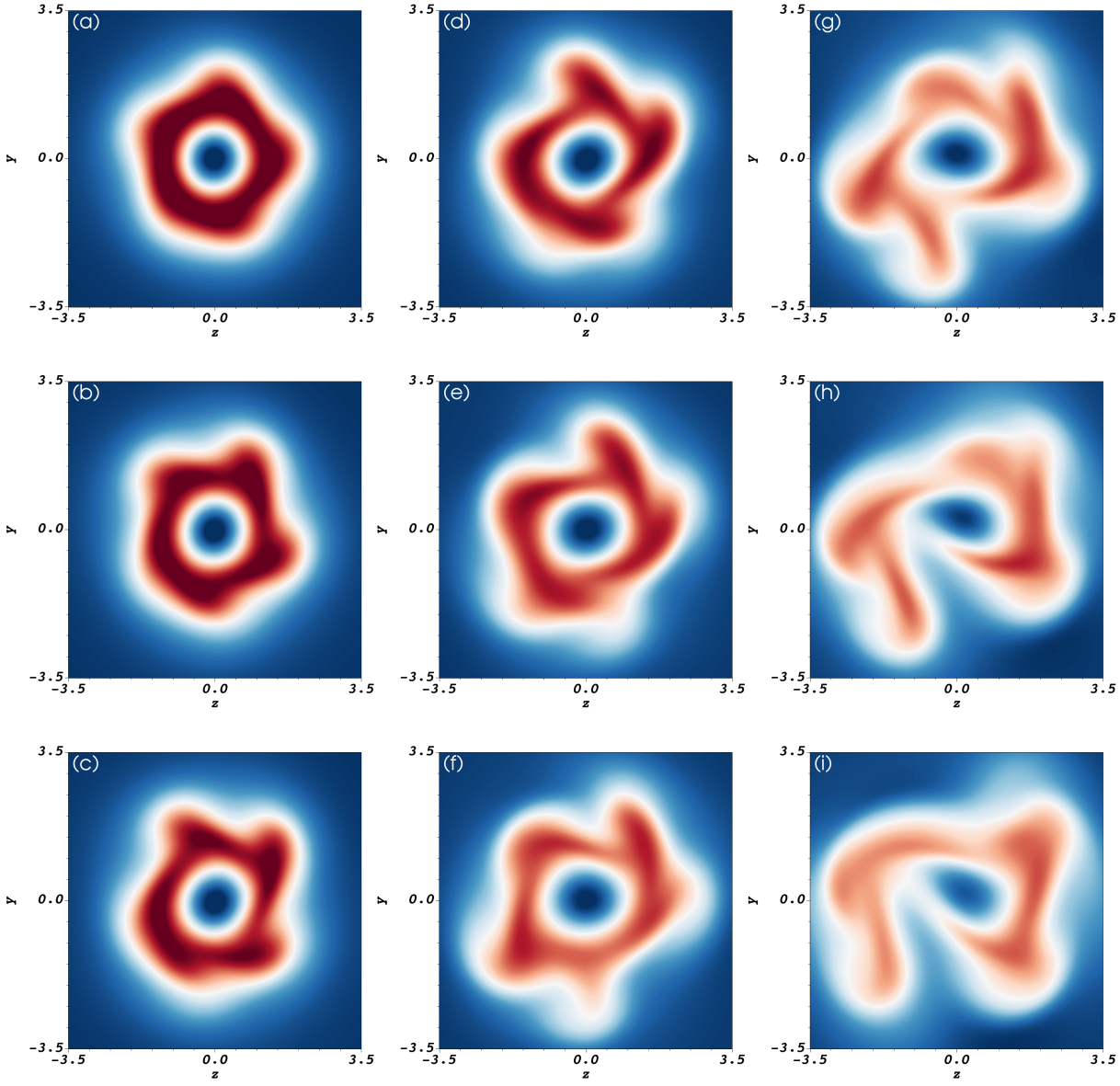

Figure 5.15. Instantaneous color contour of $v_x \in [0, 0.5]$ for $Re = 200$ and $S = 2$ at (a) $x = 17$, (b) $x = 18$, (c) $x = 19$, (d) $x = 20$, (e) $x = 21$, (f) $x = 22$, (g) $x = 23$, (h) $x = 24$ and (i) $x = 25$. Note that the swirl is clockwise.

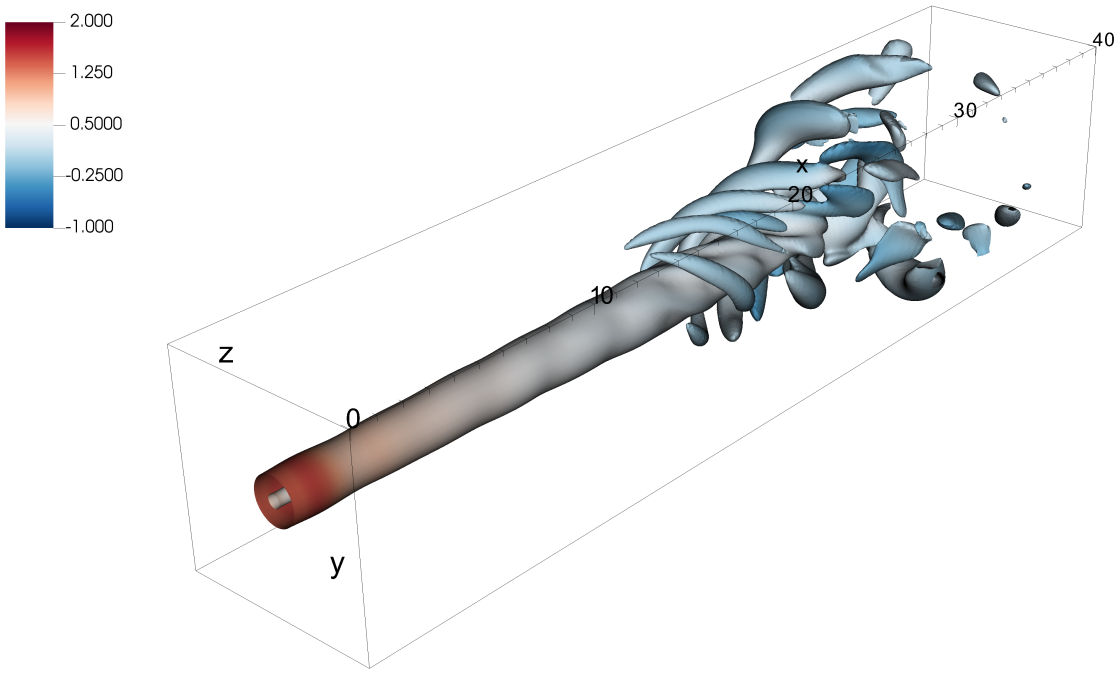

Figure 5.16. Instantaneous iso-surface of $Q = 0.01$ colored by axial vorticity for $Re = 200$ and $S = 2$. The jet is swirled clockwise.

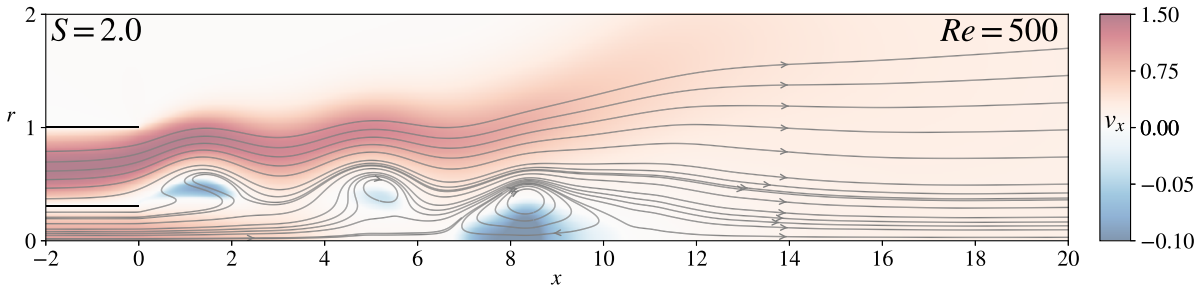

Figure 5.17. Temporal and azimuthally averaged projected streamlines colored by axial velocity for $S = 2$ and $Re = 500$.

5.3.3 Isothermal flow: effects of Re

In the single jet configuration (chapters 3 and 4), an increase in Re increased the radial divergence of the jet, moving the stagnation point upstream, and increasing the size of the bubble. In the concentric jet configuration, with swirl only located in the outer stream, radial expansion of the flow primarily occurs in the annular jet, and the centerline axial velocity initially increases for increasing Re because of reduced diffusion. Thus, for $S = 2$, the time-averaged $Re = 500$ solution, shown in Figure 5.17, shows a recirculation zone that forms between the streams just off the injectors. This figure also clearly highlights the stronger penetration of the central jet as compared to the $Re = 200$ solution in Figure 5.13(b). After the flow recovers, a secondary breakdown occurs between the two streams at $x = 4.5$, leading to a further decay of the central jet, and the formation of a stagnation point on the central-jet axis at $x = 7$. In the bubble's wake, which begins at roughly $x = 10$, more complex vortex structures are observed, as indicated by the iso-surface of Q in Figure 5.18.

5.4 Conclusions

Effects of swirl and mixture reactivity on the structure of laminar concentric axisymmetric swirling jet flames have been explored through numerical simulations for varying values of the swirl number S and the Damköhler number D_N. For zero swirl, decreasing

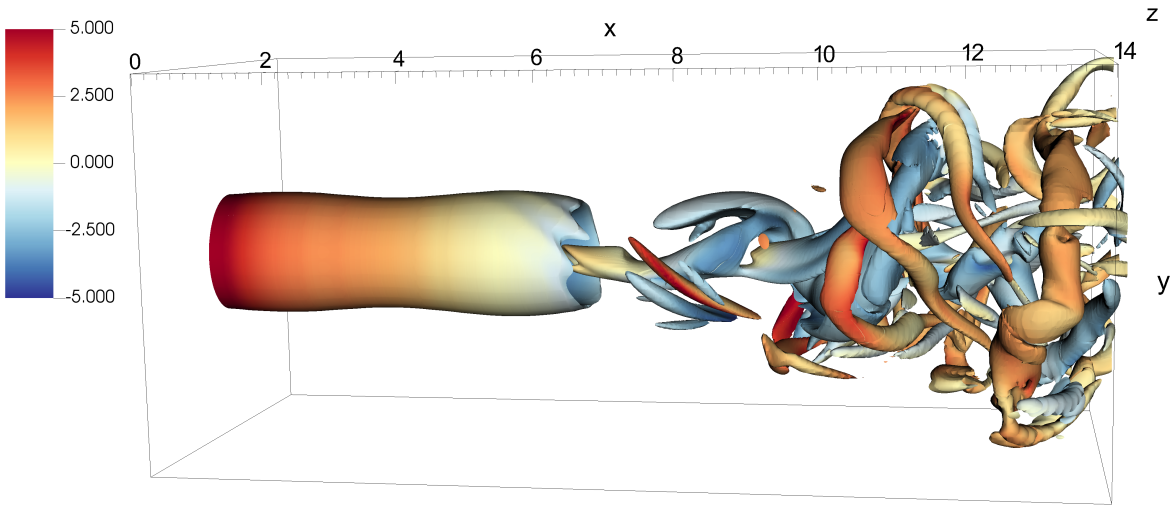

Figure 5.18. Instantaneous results for $S = 2$ and $Re = 500$: iso-surface of $Q = 1$ colored by azimuthal vorticity.

values of D_N revealed gradual transitions from an attached flame to blowoff. The same flame transitions were found for a fixed-swirl decreasing D_N simulation, although they were delayed because of the reduced axial velocities associated with the swirl. A small recirculation zone formed when the flame moved to a sufficiently large radial distance, but the overall axial liftoff characteristics were unaffected. Increasing values of S for fixed D_N were found to decrease the axial velocity in the vicinity of the flame, leading to flame displacement towards the injector and radially outward. At the critical swirl number S_B^*, a recirculation zone forms behind the flame, enhancing mixing and rapidly shifting the flame to a position close to the injectors.

Three-dimensional simulations of isothermal flow validated the use of the axisymmetric equations for the bubble breakdown flames. As the swirl and Reynolds number were increased, more complex instabilities formed downstream, which necessitate the three-dimensional framework.

The axisymmetric results in this chapter have been submitted to Combustion & Flame 2023. Keeton, Benjamin W.; Nomura, Keiko K.; Sánchez, Antonio L.; Williams,

Forman A. The dissertation author was the primary investigator in this project.

Chapter 6

Summary and future work

The objective of this work was to investigate the effects of swirl and vortex breakdown on flame transitions in laminar non-premixed swirling jet flames. The work was carried out by performing numerical simulations with increasing levels of physical and computational complexity, which formed three basic studies.

The effects of non-uniform temperature on vortex breakdown transitions were first studied for heated/cooled non-reacting swirling jets in the single jet configuration. Cold jets exhibited a greater swirl-induced adverse axial pressure gradient, and thus reduced critical swirl numbers for the first transition to bubble breakdown. The specific extent to which this decrease occurred was found to depend upon the jet Reynolds number. Steady axisymmetric forms of the conservation equations were found to be effective in describing the transition to bubble breakdown since for the moderate Reynolds numbers considered, the upstream flow remains stable and axisymmetric. For the isothermal flow, both axisymmetric and three-dimensional simulations predicted the same transitions to conical breakdown, although the three-dimensional flow exhibited a more open reciruclation zone. For non-isothermal cases, three-dimensional simulations were needed to determine critical swirl numbers for the transition to the cone, which remained relatively constant across the entire range of jet-to-ambient density ratios.

Using the same single-jet configuration, critical swirl numbers in Burke-Schumann (infinite reaction rate) swirling flames were evaluated as a function of the relevant thermo-

chemical parameters. For the methane-air flames considered, dilution played a negligible role in the first transition to bubble breakdown, since counteracting effects of the exothermicity and the stoichoimetric value of the mixture fraction left the jet core unaffected by the flame, which was positioned in the surrounding shear layer. The reaction sheets passed around the recirculating fuel and products, producing jet-like flames. The transition to the cone for moderate values of dilution produced a single-celled conical breakdown flame, that retained a jet-like structure, while for extreme values of dilution, the flame sheet stabilized near the jet inlet. Unlike the comparable axisymmetric cold jets discussed earlier, the moderate-dilution cones that emerged at the transition reached a steady state with a more open recirculation zone, which may be influenced by the increased radial velocities associated with thermal expansion. Although individual contributions of both the exothermicity and the stoichiometric value of the mixture fraction played a larger role in both transitions, the critical swirl numbers still remained relatively constant across the range of parameters encountered in these flames.

The third study investigated vortex breakdown in the more practical concentric jet configuration, which is used for non-premixed flame stabilization. For the axisymmetric isothermal flow, the relatively large central jet momentum considered prevents the formation of breakdown just off the injector exit plane where the swirl-induced radial expansion of the annular jet occurs. Once the central jet decays downstream, and the swirl in the annular jet was redirected towards the central axis, a small recirculation zone formed. For the Burke-Schumann flame, similar to the single-jet analysis, the viscosity increase associated with the reaction considerably delayed breakdown. For the finite-rate reaction flame, decreasing values of the Damköhler number resulted in the formation of triple flames which promoted the transition to bubble breakdown by redirecting the flow radially inward at a position just upstream of the flame base. The addition of swirl induced an adverse axial pressure gradient that reduced the axial velocity at the base of the flame, lowering the critical value of Damköhler number needed for blow-off. Three-dimensional simulations of the isothermal

flow confirmed that for moderate values of swirl, the axisymmetric assumption was sufficient to capture the physics upstream of the flames considered. For post-breakdown levels of swirl, the recirculation zone and wake were unstable, and three-dimensional simulations were required to accurately study the precessing stagnation point.

The work presented provides important insight into the effects of temperature variation on laminar vortex breakdown in two fundamental non-premixed flame configurations. While practical combustion chambers typically operate at higher Reynolds numbers, the instantaneous stabilization mechanism for turbulent flames is closely linked with that in the laminar regime. The first critical swirl number studied in this work provides a more detailed understanding of the appearance (and disappearance) of breakdown, which may contribute to intermittent recirculation regions that trigger blow-off or thermoacoustic instabilities. On the other hand, increasing values of swirl may lead to significant changes in the mean flame shape, or excessive heating of combustion hardware. Practical combustion chambers typically require a narrow range of swirl for proper operation, and the fundamental analysis presented here may be used to improve our understanding of these more complex flows.

This work suggests further development for numerical simulations of vortex breakdown. One aspect of the problem that requires more attention is the effects of the upstream boundaries on conical breakdown. In the single-jet configuration, the effects of the fixed inflow plane appear to be relevant for the range of swirl numbers and Reynolds numbers considered. As the stagnation point approaches the inlet plane, radial velocities increase, which may contribute to the formation of the cone. The present work also suggests further studies to expand our knowledge of swirl-induced flame stabilization. In the concentric jet configuration, the analysis may be continued by incorporating additional complexity like turbulence, detailed chemistry and liquid fuels.

Appendix

Steady-state code

The spatial discretization is based on the finite-element method, which, similar to the spectral element method, considers the variational form of the equations given by (2.38)-(2.41) with $\partial/\partial t = 0$. A simplification is introduced to the momentum equation (2.39) by redefining the pressure to include the isotropic component of the viscous stress tensor, reducing the number of terms in a redefined stress tensor $\tau = \mu[\boldsymbol{\nabla v} + \boldsymbol{\nabla v}^T]$. This approach was avoided in the unsteady simulations since the velocity divergence was used to couple the thermal and momentum equations during the time-advancement (see § 2.5). The inlet and lateral boundary conditions are unchanged from the unsteady simulations, and at the outflow boundary $\partial\Omega_o$, the convective condition is replaced by stress-free adiabatic conditions. The weak form of the equations are multiplied by r to remove the singularity at the axis, and then cast onto the basis of $\mathbb{P}_2, \mathbb{P}_1, \mathbb{P}_2$ and $\mathbb{P}_2$ finite elements for the velocity, pressure, temperature and mixture fraction, respectively, using FreeFEM (Hecht, 2012).

The solutions to the steady equations are obtained using a root-finding scheme involving a Newton-Raphson algorithm, similar to previous computations of steady vortex breakdown (Meliga and Gallaire, 2011; Douglas et al., 2021). To simplify the notation, the strong conservation equations (2.8)-(2.11) are written in the simplified form

$$\mathcal{M}\frac{\partial \boldsymbol{q}}{\partial t} + \mathcal{R}(\boldsymbol{q}, Re, S, \Lambda, \gamma, Z_s) = 0, \tag{6.1}$$

where $\boldsymbol{q} = [\boldsymbol{v}, p, T, Z]^{\mathrm{T}}$ is the solution vector, and $\mathcal{M}$ and $\mathcal{R}$ are the mass and axisymmetric

steady system operators, respectively. One approach to obtain the steady-state solutions involves fixing all parameters and branching along one free parameter, either Re, S, Λ, γ or Z_s, so that the steady solutions satisfy $\mathcal{R}(\boldsymbol{q}, Re, S, \Lambda, \gamma, Z_s) = 0$. These solutions may be obtained through the classical Newton method that updates an initial guess $\boldsymbol{q}_0$ by solving the linear system

$$\mathcal{J}(\boldsymbol{q}_0)\delta\boldsymbol{q}_0 = \mathcal{R}(\boldsymbol{q}_0), \tag{6.2}$$

where $\mathcal{J} = \partial\mathcal{R}/\partial\boldsymbol{q}$ is the Jacobian operator. The linear system is solved in parallel with PETSc (Balay et al., 2023) based on a factorization via MUMPS (Amestoy et al., 2001). Each successive iteration uses the updated solution $\boldsymbol{q}_0 \leftarrow \boldsymbol{q}_0 - \delta\boldsymbol{q}_0$, and the procedure is repeated until the $\mathcal{L}^2$ -norm of the residual is smaller than 10^{-8}. This method is known to fail near a turning point where several branches exist. Previous studies (Meliga and Gallaire, 2011; Douglas et al., 2021) have used predictor-corrector algorithms for branching, but since the focus of this analysis is on pre-breakdown solutions ahead of turning points, a simple finite-difference scheme was used to generate initial guesses at the next increment of the free parameter.

To initialize a branch, the columnar initial condition (see § 2.4) used in the unsteady calculations was set as the initial guess for $\boldsymbol{q}_0$, and the Reynolds number was increased from Stokes flow up to the fixed value of interest. This solution was then used to begin the branching method along the free parameter.

References

Adzlan, A. and Gotoda, H. Experimental investigation of vortex breakdown in a coaxial swirling jet with a density difference. *Chem. Eng. Sci.*, 80:174–181, 2012.

Althaus, W., Brücker, C., and Weimer, M. Breakdown of slender vortices. In Green, S. I., editor, *Fluid Vortices*, pages 373–426. Springer Netherlands, 1995.

Amestoy, P.R., Duff, I.S., L'Excellent, J.-Y., and Koster, J. A fully asynchronous multifrontal solver using distributed dynamic scheduling. *SIAM J. Matrix Anal. A.*, 23(1): 15–41, 2001.

Balarac, Guillaume and Metais, Olivier. The near field of coaxial jets: A numerical study. *Phys. Fluids*, 17(6):065102, 2005.

Balay, S., Abhyankar, S., Adams, M.F., Benson, S., Brown, J., Brune, P., Buschelman, K., Constantinescu, E.M., Dalcin, L., Dener, Alp, Eijkhout, V., Faibussowitsch, J., Gropp, W.D., Hapla, V., Isaac, T., Jolivet, P., Karpeev, D., Kaushik, D., Knepley, M.G., Kong, F., Kruger, S., May, D.A., McInnes, L.C., Mills, R.T., Mitchell, L., Munson, T., Roman, J.E., Rupp, K., Sanan, P., Sarich, J., Smith, B.F., Zampini, S., Zhang, H., and Zhang, J. PETSc Web page, 2023. https://petsc.org.

Benjamin, T.B. Theory of the vortex breakdown phenomenon. *J. Fluid Mech.*, 14(4): 593–629, 1962.

Billant, P. and Gallaire, F. A unified criterion for the centrifugal instabilities of vortices and swirling jets. *J. Fluid Mech.*, 734:5–35, 2013.

Billant, P., Chomaz, J.M., and Huerre, P. Experimental study of vortex breakdown in swirling jets. *J. Fluid Mech.*, 376:183–219, 1998.

Boström, E. Investigation of outflow boundary conditions for convection-dominated incompressible fluid flows in a spectral element framework. Master's thesis, KTH Royal Institute of Technology, 2015.

Brown, G.L. and Lopez, J. M. Axisymmetric vortex breakdown Part 2. physical mechanisms. *J. Fluid Mech.*, 221:553–576, 1990.

Buckmaster, J. Edge-flames. *Prog. Energ. Combust.*, 28(5):435–475, 2002.

Burke, S. and Schumann, T. Diffusion flames. *Ind. Eng. Chem.*, 20(10):998–1004, 1928.

Cha, M., Lee, D.S., and Chung, S. Effect of swirl on lifted flame characteristics in nonpremixed jets. *Combust. Flame*, 117(3):636–645, 1999.

Champagne, F.H. and Kromat, S. Experiments on the formation of a recirculation zone in swirling coaxial jets. *Exp. Fluids*, 29(5):494–504, 2000.

Chen, R.H. and Driscoll, J. The role of the recirculation vortex in improving fuel-air mixing within swirling flames. *Symp. (Int.) Combust.*, 22:531–540, 1989.

Chen, Y.C. and Bilger, R.W. Stabilization mechanisms of lifted laminar flames in axisymmetric jet flows. *Combust. Flame*, 122:377–399, 2000.

Chigier, N.A. and Beér, J.M. The flow region near the nozzle in double concentric jets. *J. Basic Eng.*, 86:797–804, 12 1964.

Chung, S.H. and Lee, B.J. On the characteristics of laminar lifted flames in a nonpremixed jet. *Combust. Flame*, 86:62–72, 1991.

Claypole, T.C. and Syred, N. Effect of swirl burner aerodynamics on NO_x formation. *Symp. (Int.) Combust.*, 18:81–89, 1981.

Dagan, Y., Arad, E., and Tambour, Y. The evolution of local instability regions in turbulent non-premixed flames. *J. Fluid. Mech.*, 803:18–50, 2016.

Darmofal, D. The role of vorticity dynamics in vortex breakdown. *AIAA J.*, 93:3036, 1993.

Degenève, A., Mirat, C., Caudal, J., Vicquelin, R., and Schuller, T. Effects of swirl on the stabilization of non-premixed oxygen-enriched flames above coaxial injectors. *J. Eng. Gas Turb. Power*, 141(12):121018, 2019a.

Degenève, A., Vicquelin, R., Mirat, C., Labegorre, B., Jourdaine, P., Caudal, J., and Schuller, T. Scaling relations for the length of coaxial oxy-flames with and without swirl. *Proc. Combust. Inst.*, 37:4563–4570, 2019b.

Degenève, A., Vicquelin, R., Mirat, C., Caudal, J., and Schuller, T. Impact of co-and counter-swirl on flow recirculation and liftoff of non-premixed oxy-flames above coaxial injectors. *Proc. Combust. Inst.*, 38(4):5501–5508, 2021.

Del Taglia, C., Blum, L., Gass, J., Ventikos, Y., and Poulikakos, D. Numerical and experimental investigation of an annular jet flow with large blockage. *J. Fluids Eng.*, 126(3): 375–384, 2004.

Del Taglia, C., Moser, A., and Blum, L. Spontaneous break of symmetry in unconfined laminar annular jets. *J. Fluid. Eng.*, 131(8), 2009.

Deville, M.O., Fischer, P.F., and Mund, E.H. *High-order methods for incompressible fluid flow*, volume 9. Cambridge university press, 2002.

Dong, S., Karniadakis, G.E., and Chryssostomidis, C. A robust and accurate outflow boundary condition for incompressible flow simulations on severely-truncated unbounded domains. *J. Comput. Phys.*, 261:83–105, 2014.

Douglas, C.M. and Lesshafft, L. Confinement effects in laminar swirling jets. *J. Fluid. Mech.*, 945:A27, 2022.

Douglas, C.M., Emerson, B.L., and Lieuwen, T.C. Nonlinear dynamics of fully developed swirling jets. *J. Fluid Mech.*, 924:A14, 2021.

Douglas, C.M., Emerson, B.L., and Lieuwen, T.C. Dynamics and bifurcations of laminar annular swirling and non-swirling jets. *J. Fluid Mech.*, 943:A35, 2022.

Escudier, M. Vortex breakdown: Observations and explanations. *Prog. Aerosp. Sci.*, 25(2): 189–229, 1988.

Farokhi, S., Taghavi, R., and Rice, E.J. Effect of initial swirl distribution on the evolution of a turbulent jet. *AIAA J.*, 27(6):700–706, 1989.

Feikema, D., Chen, R.H., and Driscoll, J. Enhancement of flame blowout limits by the use of swirl. *Combust. Flame*, 80(2):183–195, 1990.

Feikema, D., Chen, R.H., and Driscoll, J. Blowout of nonpremixed flames: maximum coaxial air velocities achievable, with and without swirl. *Combust. Flame*, 86(4):347–358, 1991.

Fernández-Tarrazo, E., Sánchez, A.L., Liñán, A., and Williams, F.A. A simple one-step chemistry model for partially premixed hydrocarbon combustion. *Combust. Flame*, 147 (1-2):32–38, 2006a.

Fernández-Tarrazo, E., Vera, M., and Liñán, A. Liftoff and blowoff of a diffusion flame between parallel streams of fuel and air. *Combust. Flame*, 144(1-2):261–276, 2006b.

Fischer, P.F., Lottes, J.W., and Kerkemeier, S.G. nek5000 web page, 2008. http://nek5000.mcs.anl.gov.

Fischer, P.F., Schmitt, M., and Tomboulides, A.G. Recent developments in spectral element simulations of moving-domain problems. *Recent progress and modern challenges in applied mathematics, modeling and computational science*, pages 213–244, 2017.

Fitzgerald, A.J., Hourigan, K., and Thompson, M.C. Towards a universal criterion for predicting vortex breakdown in swirling jets. In Behnia, M., Lin, W., and McBain, G. D., editors, *Proceeding of the Fifteenth Australasian Fluid Mechanics Conference*. The University of Sydney, 2004.

Gallaire, F. and Chomaz, J.M. Instability mechanisms in swirling flows. *Phy. Fluids*, 15(9): 2622–2639, 2003.

Gallaire, F., Rott, S., and Chomaz, J.M. Experimental study of a free and forced swirling jet. *Phys. Fluids*, 16(8):2907–2917, 2004.

Gallardo-Ruiz, J.M., del Pino, C., and Fernandez-Feria, R. Quasicylindrical description of a swirling light gas jet discharging into a heavier ambient gas. *Phys. Fluids*, 22(11):113601, 2010.

Geuzaine, C. and Remacle, J.F. Gmsh: A 3-d finite element mesh generator with built-in pre-and post-processing facilities. *Int. J. Numer. Meth. Eng.*, 79(11):1309–1331, 2009.

Giannadakis, A, Perrakis, K, and Panidis, T. A swirling jet under the influence of a coaxial flow. *Exp. Therm. Fluid. Sci.*, 32(8):1548–1563, 2008.

Görtler, H. Decay of swirl in an axially symmetrical jet, far from the orifice. *Rev. Mat. Hisp. Am.*, 14(4):143–178, 1954.

Hall, M. G. A new approach to vortex breakdown. In *Proceedings of Heat Transfer and Fluid Mechanics Institute*, pages 319–340. Stanford University Press, 1967.

Hall, M. G. Vortex breakdown. *Annu. Rev. Fluid Mech.*, 4(1):195–218, 1972.

Harvey, J.K. Some observations of the vortex breakdown phenomenon. *J. Fluid Mech.*, 14 (4):585–592, 1962.

Hecht, F. New development in freefem++. *J. Numer. Math.*, 20(3-4):251–265, 2012.

Higuera, F.J and Moser, R. Effect of chemical heat release in a temporally evolving mixing layer. *CTR Report*, pages 19–40, 1994.

Kadu, P.A., Sakai, Y., Ito, Y., Iwano, K., Sugino, M., Katagiri, T., and Nagata, K. Numerical investigation of passive scalar transport and mixing in a turbulent unconfined coaxial swirling jet. *Int. J. Heat. Mass Tran.*, 142:118461, 2019.

Kadu, P.A., Sakai, Y., Ito, Y., Iwano, K., Sugino, M., Katagiri, T., Hayase, T., and Nagata, K. Application of spectral proper orthogonal decomposition to velocity and passive scalar fields in a swirling coaxial jet. *Phys. Fluids*, 32(1):015106, 2020.

Keeton, B.W., Carpio, J., Nomura, K.K., Sánchez, A.L., and Williams, F.A. Vortex breakdown in variable-density gaseous swirling jets. *J. Fluid Mech.*, 936, 2022.

Keeton, B.W., Nomura, K.K., Sánchez, A.L., and Williams, F.A. Vortex breakdown in

swirling Burke–Schumann flames. *Proc. Combust. Inst.*, 39(2):1635–1645, 2023.

Lee, B.J. and Chung, S.H. Stabilization of lifted tribrachial flames in a laminar nonpremixed jet. *Combust. Flame*, 109:163–172, 1997.

Leibovich, S. The structure of vortex breakdown. *Annu. Rev. Fluid Mech.*, 10(1):221–246, 1978.

Leibovich, S. Vortex stability and breakdown-survey and extension. *AIAA J.*, 22(9):1192–1206, 1984.

Leibovich, S. and Stewartson, K. A sufficient condition for the instability of columnar vortices. *J. Fluid Mech.*, 126:335–356, 1983.

Liang, H. and Maxworthy, T. An experimental investigation of swirling jets. *J. Fluid Mech.*, 525:115, 2005.

Liñán, A., Fernandez-Tarrazo, E., Vera, M., and Sánchez, A.L. Lifted laminar jet diffusion flames. *Combust. Sci. Technol.*, 177(5-6):933–953, 2005.

Liñán, A., Vera, M., and Sánchez, A.L. Ignition, liftoff, and extinction of gaseous diffusion flames. *Annu. Rev. Fluid Mech.*, 47:293–314, 2015.

Loiseleux, T., Chomaz, J.M., and Huerre, P. The effect of swirl on jets and wakes: Linear instability of the rankine vortex with axial flow. *Phys. Fluids*, 10(5):1120–1134, 1998.

Loitsianskii, L. G. Propagation of a whirling jet in an infinite space filled with the same fluid. *Prikl. Mat. Mekh*, 17(3):7, 1953.

Lucca-Negro, O. and O'Doherty, T. Vortex breakdown: a review. *Prog. Energy Combust. Sci.*, 27(4):431–481, 2001.

Maday, Y., Patera, A.T., and Rønquist, E.M. An operator-integration-factor splitting method for time-dependent problems: application to incompressible fluid flow. *J. Sci. Comput.*, 5:263–292, 1990.

Majda, A. and Sethian, J. The derivation and numerical solution of the equations for zero mach number combustion. *Combust. Sci. Technol.*, 42(3-4):185–205, 1985.

Manoharan, K., Hansford, S., O'Connor, J., and Hemchandra, S. Instability mechanism in a swirl flow combustor: precession of vortex core and influence of density gradient. In *ASME Turbo Expo 2015: Turbine Technical Conference and Exposition*. American Society of Mechanical Engineers, 2015.

Manoharan, K., Frederick, M., Clees, S., O'Connor, J., and Hemchandra, S. A weakly nonlinear analysis of the precessing vortex core oscillation in a variable swirl turbulent round jet. *J. Fluid Mech.*, 884:A29, 2020.

Meliga, P. and Gallaire, F. Control of axisymmetric vortex breakdown in a constricted pipe: nonlinear steady states and weakly nonlinear asymptotic expansions. *Phys. Fluids*, 23(8): 084102, 2011.

Moise, P. Bistability of bubble and conical forms of vortex breakdown in laminar swirling jets. *J. Fluid Mech.*, 889:A31, 2020.

Moise, P. and Mathew, J. Bubble and conical forms of vortex breakdown in swirling jets. *J. Fluid Mech.*, 873:322–357, 2019.

Moise, P. and Mathew, J. Hysteresis and turbulent vortex breakdown in transitional swirling jets. *J. Fluid Mech.*, 915, 2021.

Montagnani, D. and Auteri, F. Non-modal analysis of coaxial jets. *J. Fluid Mech.*, 872: 665–696, 2019.

Moreno-Boza, D., Coenen, W., Sevilla, A., Carpio, J., Sánchez, A.L., and Liñán, A. Diffusion-flame flickering as a hydrodynamic global mode. *J. Fluid Mech.*, 798:997–1014, 2016.

Moreno-Boza, D., Coenen, W., Carpio, J., Sánchez, A.L., and Williams, F.A. On the critical conditions for pool-fire puffing. *Combust. Flame*, 192:426–438, 2018.

Oberleithner, K., Sieber, M., Nayeri, C., Paschereit, C.O., Petz, C., Hege, H., Noack, B.R., and Wygnanski, I. Three-dimensional coherent structures in a swirling jet undergoing vortex breakdown: stability analysis and empirical mode construction. *J. Fluid Mech.*, 679:383 – 414, 2011.

Oberleithner, K., Paschereit, C., Seele, R., and Wygnanski, I. Formation of turbulent vortex breakdown: intermittency, criticality, and global instability. *AIAA J.*, 50(7):1437–1452, 2012.

Offermans, N., Marin, O., Schanen, M., Gong, J., Fischer, P.F., Schlatter, P., Obabko, A., Peplinski, A., Hutchinson, M., and Merzari, E. On the strong scaling of the spectral element solver nek5000 on petascale systems. In *Proceedings of the Exascale Applications and Software Conference 2016*, pages 1–10, 2016.

Orszag, S.A., Israeli, M., and Deville, M.O. Boundary conditions for incompressible flows. *J. Sci. Comput.*, 1:75–111, 1986.

Panda, J. and McLaughlin, D.K. Experiments on the instabilities of a swirling jet. *Phys. Fluids*, 6(1):263–276, 1994.

Patel, S., Fischer, P.F., Min, M., and Tomboulides, A.G. A characteristic-based spectral element method for moving-domain problems. *J. Sci. Comput.*, 79:564–592, 2019.

Patera, A.T. A spectral element method for fluid dynamics: laminar flow in a channel expansion. *J. Comput. Phys.*, 54(3):468–488, 1984.

Pattanshetti, A., Santhosh, R., and Attar, N. Experimental and numerical investigation of recirculation structures in isothermal swirling coaxial jet. *J. Fluid. Eng.*, 144(10):101204, 2022.

Pierce, C.D. and Moin, P. Method for generating equilibrium swirling inflow conditions. *AIAA J.*, 36(7):1325–1327, 1998.

Qadri, U. *Global stability and control of swirling jets and flames*. PhD thesis, University of Cambridge, 2014.

Rajamanickam, K. and Basu, S. Insights into the dynamics of conical breakdown modes in coaxial swirling flow field. *J. Fluid Mech.*, 853:72–110, 2018.

Revuelta, A., Sánchez, A.L., and Liñán, A. The quasi-cylindrical description of submerged laminar swirling jets. *Phys. Fluids*, 16(3):848–851, 2004.

Ruetsch, G.R., Vervisch, L., and Liñán, A. Effects of heat release on triple flames. *Phys. Fluids*, 7(6):1447–1454, 1995.

Ruith, M.R., Chen, P., and Meiburg, E. Development of boundary conditions for direct numerical simulations of three-dimensional vortex breakdown phenomena in semi-infinite domains. *Comput. Fluids*, 33(9):1225–1250, 2004.

Saediamiri, M., Birouk, M., and Kozinski, J. On the stability of a turbulent non-premixed biogas flame: Effect of low swirl strength. *Combust. Flame*, 161(5):1326–1336, 2014.

Salvetti, M.V., Orlandi, P., and Verzicco, R. Numerical simulations of transitional axisymmetric coaxial jets. *AIAA J.*, 34(4):736–743, 1996.

Santhosh, R. and Basu, S. Transitions and blowoff of unconfined non-premixed swirling flame. *Combust. Flame*, 164:35–52, 2016.

Santhosh, R., Miglani, A., and Basu, S. Transition in vortex breakdown modes in a coaxial isothermal unconfined swirling jet. *Phys. Fluids*, 26(4), 2014.

Savas, Ö. and Gollahalli, S.R. Stability of lifted laminar round gas-jet flame. *J. Fluid Mech.*, 165:297–318, 1986.

Sloan, D.G., Smith, P.J., and Smoot, L.D. Modeling of swirl in turbulent flow systems. *Prog. Energ. Combust.*, 12(3):163–250, 1986.

Smooke, M.D. *Reduced kinetic mechanisms and asymptotic approximations for methane-air flames: a topical volume*. Springer, Heidelberg, Germany, 1991.

Spall, R., Gatski, T., and Grosch, C. A criterion for vortex breakdown. *Phys. Fluids*, 30 (11):3434–3440, 1987.

Squire, H.B. Analysis of the vortex breakdown phenomenon: part I. Report 102, Aeronautical Dept., Imperial College, 1960.

Syred, N. and Beer, J. Combustion in swirling flows: a review. *Combust. Flame*, 23(2): 143–201, 1974.

Tangirala, V. and Driscoll, J. Temperatures within non-premixed flames: effects of rapid mixing due to swirl. *Combust. Sci. Technol.*, 60(1-3):143–162, 1988.

Tangirala, V., Chen, R.H., and Driscoll, J. Effect of heat release and swirl on the recirculation within swirl-stabilized flames. *Combust. Sci. Technol.*, 51(1-3):75–95, 1987.

Tomboulides, A.G., Lee, J., and Orszag, S.A. Numerical simulation of low mach number reactive flows. *J. Sci. Comput.*, 12(2):139–167, 1997.

Tummers, M.J., Hübner, A.W., Van Veen, E.H., Hanjalić, K., and Van der Meer, T.H. Hysteresis and transition in swirling nonpremixed flames. *Combust. Flame*, 156(2):447–459, 2009.

Vignat, G., Durox, D., and Candel, S. The suitability of different swirl number definitions for describing swirl flows: Accurate, common and (over-) simplified formulations. *Prog. Energ. Combust.*, 89:100969, 2022.

Von Schlichting, H. Laminare strahlausbreitung. *Z. Angew. Math. Mech.*, 13(4):260–263, 1933.

Werner, J., Frieler, C.E., and Tryggvason, G. Vortex structure and dynamics in the near field of a coaxial jet. *J. Fluid Mech.*, 241:371402, 1992.

Williams, F.A. *Combustion theory*. Addison-Wesley Pub., 1985.

Won, S.H., Chung, S.H., Cha, M.S., and Lee, B.J. Lifted flame stabilization in developing

and developed regions of coflow jets for highly diluted propane. *Proc. Combust. Inst.*, 28: 2093–2099, 2000.

Xiao, H., Luo, K., Jin, T., Wang, H., Xing, J., and Fan, J. Direct numerical simulations of turbulent non-premixed flames: Assessment of turbulence within swirling flows. *Phys. Fluids*, 33(1):015112, 2021.

Yuasa, S. Effects of swirl on the stability of jet diffusion flames. *Combust. Flame*, 66(2): 181–192, 1986.